NUMERICAL SOLUTION OF 3D HIGHLY NONLINEAR WATER ENTRY PROBLEMS

QINGYONG YANG

NUMERICAL SOLUTION OF 3D HIGHLY NONLINEAR WATER ENTRY PROBLEMS

by

©Qingyong Yang, B.Eng., M.Eng.

A thesis submitted to the
School of Graduate Studies
in partial fulfillment of the
requirements for the degree of
Doctor of Philosophy

Faculty of Engineering and Applied Science
Memorial University

October 2011
St. John's, Newfoundland, Canada

Abstract

Ships or offshore structures may experience severe water impact problems in the harsh environments, such as cargo sloshing, slamming and green water on deck. These impact loads can cause serious structural damage and are of considerable concern to the stability and survivability of ships or offshore structures. All of these forces are associated with highly nonlinear free surface flows.

The thesis presents the numerical solution of slamming problems for 3D bodies entering calm water symmetrically and asymmetrically, with prescribed entry velocities and free-fall motions. The highly nonlinear slamming problems are governed by the Navier-Stokes equations and are solved by a Constrained Interpolation Profile (CIP)-based finite difference method on a fixed Cartesian grid. The CIP method is employed for the advection calculations and a pressure-based algorithm is applied for the non-advection calculations. For the pressure computation, a Poisson-type equation is solved at each time step by the Conjugate Gradient iterative method. The solid body and free surface interfaces are captured by density functions. A panel-based method is developed to capture the interfaces of 3D bodies. The motion of a body is described in terms of six degrees of freedom.

Validation studies of the present method were carried out for several 3D bodies entering calm water symmetrically and asymmetrically with prescribed velocities and free-fall motions. Water entries of 3D bodies with prescribed velocities were first studied. For the water entry of a 3D wedge, 3D flow effects were investigated. 3D flow effects tend to cause a reduction in slamming force. The computed slamming forces are in good agreement with experimental results. For the sphere entering calm water obliquely, the computed vertical and horizontal slamming forces in general agree

well with experimental results. The simulations were further carried out for a couple of bodies with complex geometry. For the water entry of a 3D ship section, pressures near the knuckles were under-predicted by the numerical method. The slamming force on a 3D flared body was also computed by the present numerical method, and the predicted slamming forces are in good agreement with the experimental results. The maximum slamming force coefficients of a planing hull with different pitch and roll angles were computed by the present numerical method and compared with these by the 2D strip theory. The 2D results are slightly greater than the 3D solutions.

The studies were then extended to 3D bodies entering calm water with free-fall motions. The predicted motion of the half-buoyant cylinder with free-fall motion agrees well with the experimental data. For the neutrally buoyant cylinder, reasonable agreement is obtained, except at one experimental value which obviously deviates from the other data. The complicated free surface elevations during water entry of cylinder were simulated by the present numerical method. They are visually in good agreement with the photographs taken from the experiments. The present numerical method over-predicts the velocity ratios for water entry of a catamaran, especially for large drop heights. Velocity, acceleration, as well as vertical and horizontal hydrodynamic forces as a function of time were predicted by the present numerical method for the asymmetric water entry of a ship section. A satisfactory agreement with experimental drop test results is demonstrated.

Acknowledgements

I would like to give my foremost appreciation and thanks to my supervisor, Dr. Wei Qiu, who greatly enhanced my interest in Marine Hydrodynamics, for his continuous patience, kindness, encouragement, and support throughout my work on this thesis. His advice and academic guidance have been invaluable to the development of this work.

I would like to show my gratitude to Dr. David Molyneux and Dr. Heather Peng, whose guidance and supports enabled me to develop an understanding of the subject. I would also like to acknowledge advice and comments from Dr. Mahmoud R. Haddara and Dr. Serpil Kocabiyik. Many thanks are extended to my colleagues and friends at Memorial University for the useful discussions and suggestions throughout various stages of my research.

I wish to express my deep appreciation to the Canadian Foundation for Innovation and the Natural Sciences and Engineering Research Council of Canada. I would also like to express my special thanks to Defence Research and Development Canada Atlantic and Oceanic Consulting Corporation for their support through a partnership program. This work would not have been completed without their financial support.

I owe my deepest gratitude to my family. As for my wife Lei Liu, her love, patience, and encouragement have upheld me all the time. For my parents, X.L. Wang and E.Z. Yang, I am profoundly grateful for their loves and support. I would also like to give my special thanks to my grandparents, whose kindness and understanding have been the most important treasure in my life.

Contents

List of Figures

List of Tables

Nomenclatures

$\mathbf{A}$	matrix
A	area
A_p	projected area
a, b, c, d	coefficients in interpolation function
B	breadth of wedge
$B(t)$	instantaneous submerged depth
$\mathbf{b}$	column vector
C_p	slamming pressure coefficient
C_s	slamming force coefficient
C_v	velocity ratio
c_{mn}	coefficient in interpolation function
c_s	sound speed
$\mathbf{D}$	diagonal vector of panel
E	comparison error
F_i	hydrodynamic force
F_n	Froude number

F_r	resistance
F_s	safety factor
f	objective value in interpolation function
f_i^b	body force due to gravity
f_x, f_y, f_z	derivatives of objective value
g	gravity acceleration
H	drop height
L	length of hull
$\mathbf{M}$	diagonal matrix
$\mathbf{M}_B$	body mass
m	meter
m_a	added mass
m^*	mass coefficient
N_j	total number of panels
N_k	total number of nodes
$\mathbf{n}$	normal vector
p	pressure
p^n	pressure in time step n

p^{n+1}	pressure in time step $n+1$
p^*	pressure in advection phase
R	radius of a sphere
R_c	coordinates of central point of a panel
R_i	coordinates of corner points of a panel
r_i	distance vector
s	second
t	time
u_b	body velocity
$\mathbf{u}_c$	translation velocity of mass center
u_i	velocity components
u_i^b	body velocity components
u_i^n	velocity components in time step n
u_i^{n+1}	velocity components in time step $n+1$
u_i^*	velocity components in advection phase
u_i^{**}	velocity components in non-advection phase I
V	vertical velocity
$\mathbf{x}$	unknown column vector

x_c, y_c, z_c	coordinates of mass center
$x_{c_j}, y_{c_j}, z_{c_j}$	coordinates of centroid of panels
x_i	coordinates in Cartesian coordinates system
x_p	particle position of upwind departure point
$x_{R_k}, y_{R_k}, z_{R_k}$	coordinates of nodes of panels
α	grid distribution factor
β	grid stretching factor
Γ	net moment
Δm	mass of a computational cell
Δt	time step
ΔV	volume of a computational cell
$\Delta x, \Delta y, \Delta z$	grid spacings
δ	Relative error
δ_{ij}	Kronecker's delta function
ε	panel contribution factor
ϵ	small positive constant number
Φ	velocity potential
ϕ_m	density function

μ	dynamic viscosity coefficient
μ_{air}	dynamic viscosity coefficient for air
μ_{ghost}	dynamic viscosity coefficient for ghost points inside the body
μ_{water}	dynamic viscosity coefficient for water
Π	tensor of inertia moment
π	circumference ratio
ρ	mass density
ρ_{air}	mass density for air
ρ_{ghost}	mass density for ghost points inside the body
ρ_{solid}	mass density for solid body
ρ_{water}	mass density for water
ρ^n	mass density in time step n
ρ^{n+1}	mass density in time step $n+1$
ρ^*	mass density after advection phase
σ_{ij}	total stress
φ	controlling function for panel concentration
ω	angular velocity

Ω	computational domain
F	cubic polynomial interpolation function
F_x, F_y, F_z	derivatives of cubic polynomial interpolation function
$\emptyset$	tangent function
$\pm\infty$	positive, negative infinity

Abbreviations

BEM	boundary element method
BFC	boundary-fitted coordinate
CFD	computational fluid dynamics
CFL	Courant Friedrich Lewy
CG	conjugate gradient
CIP	constrained interpolation profile
EOS	equation of state
FDM	finite difference method
FPSO	floating production storage and offloading
LNG	liquefied natural gas
LS	level set
RE	Richardson extrapolation
RMSE	root-mean-square errors
SPD	symmetric positive definite
SPH	smoothed particle hydrodynamics
VOF	volume of fluid
1D	one-dimensional
2D	two-dimensional
3D	three-dimensional

Chapter 1

Introduction

1.1 Background

Ships or offshore structures may experience severe water impact problems in the harsh environment, such as slamming, green water on deck and sloshing in tank etc (See Fig. 1-1). These impact loads are associated with highly nonlinear free surface flows. They can cause serious structural damages, and are of considerable concern to the stability and survivability of ships or offshore structures.

Slamming is a highly nonlinear free surface flow phenomenon caused by motions of a floating structure in a rough sea. When the hull emerges from the water due to its motion and re-enters the water, the combination of ship motion and free surface motion can result in large dynamic impact loads, and subsequent damage to the hull. Slamming load is one of typical issues in the dynamic load analysis. For large ships, slamming force analysis is of great concern in structural design. For high speed marine crafts, slamming impact is a primary factor in motion prediction. In addition, many offshore marine operations involve the lowering of objects through the free surface. Slamming force can impact on the operations and cause local damage of the objects.

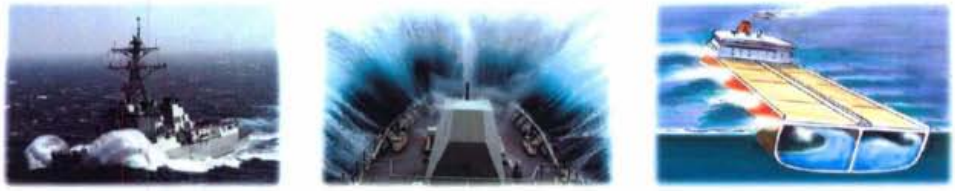

(a) Slamming (b) Green water on deck (c) Sloshing

Figure 1-1: Violent fluid motion

To improve the safe and effective operation of surface ships and offshore structures in heavy seas, it is necessary to increase the knowledge of flow behavior and wave induced motion of ships during water impacts. The forces and pressure that are exerted by the fluid impact on the structures are especially important.

Many experimental studies have been carried out on water impact. Greenhow and Lin (1983) conducted some 2D slamming tests, during which the surface of the water was displaced a great deal from its undistributed position. Particular attention was paid to the point of intersection of the free surface and a moving body. Zhao et al. (1996) carried out drop tests for a 2D wedge and a real ship section. Hydrodynamic forces and pressure distributions were obtained. 3D flow effects were discussed in their work. Troesch and Kang (1986) conducted a model test of a sphere entering calm water with both vertical and horizontal velocities. Experiments have been the primary source of practical information, but they are expensive to conduct.

Numerical simulations have also been used to study the water impact. The main difficulty in the numerical method arises from the treatment of complicated hydrodynamic phenomena such as high speed impacts on structures, breaking waves, jets, and air bubble entrainment. A review of earlier research on water entry problems was given by Korobkin and Pukhnachov (1988). Zhao and Faltinsen (1993) studied the water entry of a symmetrical wedge using the boundary element method with constant elements. Yang and Qiu (2007) solved the 2D water entry problem

of symmetric and asymmetric wedges with various deadrise angles using the CIP method. A summary of the numerical methods on slamming is given in the next section.

1.2 Literature Review

Water entry is a complex hydrodynamic problem. Many different methods have been proposed. Before the development of computer, these were predominantly analytical methods based on different assumptions intended to make the problem mathematically manageable. The theoretical analysis of the impact problem was first conducted by von Karman (1929) and modified by Wagner (1932) to include the local uprise of the water. Armand and Cointe (1986), Cointe (1991) and Howison et al. (1991) extended Wagner's theory to analyze the wedge entry problem using matched asymptotic expansions for wedges with small deadrise angles. Furthermore, Dobrovol'skaya (1969) developed an analytical solution in terms of a nonlinear singular integral equation for the problem of symmetrical entry of a wedge into calm water. Shiffman and Spencer (1951) developed general expressions for the pressure distribution and slamming force on a cone. Miloh (1981) derived the added mass coefficients for a double spherical bowl with an analytical solution. For wedge-type bodies, these approximate solutions can be easily used to calculate the slamming forces. However, there are limitations when they are applied to more complex geometries.

With the general availability of computers, the emphasis in the treatment of free surface problems is shifting towards numerical methods. Many numerical methods have been developed to solve the water entry problem on the basis of potential flow theory. Based on the work of Vinje and Brevig (1981), Greenhow (1987) used Cauchy's formula to solve the wedge entry problem. In his work, both gravity and

nonlinear free surface conditions were taken into account. Zhao and Faltinsen (1993) studied the water entry of a symmetrical wedge using the boundary element method with constant elements. The jet tip at the intersection point of the body surface and the free surface was cut and two small constant elements were distributed. The gravity was neglected. Zhao et al. (1996) extended this method to general asymmetric bodies with flow separation. When separation occurs from a continuously curved surface, the separation points are determined empirically. There are numerical difficulties to trace the water particles at the intersection point. Lin et al. (1984) presented an approach to treat the difficulties. In their work, the boundary integral equation derived from Cauchy's formula was discretized using linear elements so that the intersection points can be used as the collocation points. Chuang et al. (2006) developed a boundary element method based on a desingularized Cauchy's formula. A numerical approach was also developed to remove the corner singularity at the intersection point of the body surface and the free surface.

Although great progress has been made in solving the highly nonlinear free surface problem with methods based on the potential flow assumption, there are difficulties for these methods to treat highly distorted or breaking free surfaces. These difficulties can be overcome by a computational fluid dynamics (CFD) method based on solving the Navier-Stokes equations. Free surface modeling methods are essential in applying CFD methods to solve the water entry problems. It is necessary to resort to numerical solutions to find the interface between air and water. Calculating the advection of free surface is a tough task since the free surface may undergo large deformation and even topological changes. For modeling the free surfaces, several technologies exist, and they can generally be classified into Lagrangian and Eulerian methods.

The Lagrangian method, also called the moving grid method, is used to construct a computational grid that is fitted and moves with the fluid by means of a boundary conforming curvilinear grid, a block-structured domain decomposition, or overset

meshes (Fekken, 2004). It is a relatively simple method of defining and tracking a free surface. Because the grid and fluid move together, the grid automatically tracks free surfaces without smearing the information at the interface. Hirt et al. (1970) used the Lagrangian method to simulate a transient flow of viscous incompressible fluids with free surfaces. In their work, the Lagrangian method gave accurate treatment of free surfaces. The principal limitation of Lagrangian methods is that they cannot track breaking free surfaces.

A special case of the Lagrangian method is the Smoothed Particle Hydrodynamics (SPH) method, originally developed by Gingold and Monaghan (1977). It has become increasingly popular, since it can treat large deforming interfaces and topological changes. SPH is a meshless technique. It divides the fluid domain into a finite number of mass carrying particles. The movement of the particles and pressure distribution in the fluid are obtained through solving the momentum equations and continuity equation within the Lagrangian description of the motion (Zheng, 2007). The method was used by Monaghan (1994) to simulate the broken dam problem. Kim et al. (2007) used the SPH method to simulate the water entry of 2D asymmetric bodies. A drawback of SPH is its inherent difficulty when modeling boundaries (Rogers et al., 2003). Another drawback is that predicted pressure may not be very accurate due to the use of an artificial pressure density relationship.

In the Eulerian method, also called fixed grid method, the computational mesh is treated as a fixed reference frame through which the fluid moves. The interface is not explicitly tracked but is reconstructed from the field variables of the fixed grid. The interface is of a finite thickness but can be sharpened by various strategies. The Eulerian method is suitable for modeling large deformation of free surfaces. However, the Eulerian method has some shortcomings associated with the determination of the free surface location. It is difficult to apply the boundary conditions at the exact location of the boundary. Another drawback is that some interface accuracy

may be lost when details of the interface can not be covered by the grid. The free surface modeling method discussed below uses a fixed Eulerian grid as the basis for computation.

The Volume of Fluid (VOF) method, developed by Nichols et al (1980) and Hirt and Nichols (1981), is a free surface capturing method. In the VOF method, a volume fraction function is introduced with values between zero and one, representing the fractional volume of a cell that is occupied by a certain fluid. The time evolution of the volume fraction function is obtained by solving an advection equation, and the volume fraction function is reconstructed in every cell. The most commonly used reconstruction methods are piecewise constant reconstruction (Hirt and Nichols, 1981) and piecewise linear reconstruction (Youngs, 1982, 1987). In the piecewise constant reconstruction, the interface is parallel to one of the coordinate axes, while the piecewise linear reconstruction uses a linear approximation with the orientation of the interface within each cell. The linear approximation is more accurate, but a significant increase in the algorithmic complexity is unavoidable. Based on the reconstructed interface, the velocity fluxes are computed at cell faces and the fluid is moved in the fixed grid. The VOF method has been made to work well by many successful applications. Hirt and Nichols (1981) applied the VOF method to simulate several complicated free surface flow problems, i.e., broken dam, undular bore and breaking bore. Kleefsman et al. (2005) solved the 2D slamming problems of symmetric bodies by the VOF method, and a finite volume discretization with a cut-cell method was applied on a fixed Cartesian grid. The VOF methods using piecewise linear approximation were highly accurate and had no mass conservation errors; however, its implementation in 3D was difficult (Yokoi, 2007).

The Level Set (LS) method, originally devised by Osher and Sethian (1988), has been proven to be successful as a free surface capturing method. In the LS method, the deformation and movement of the free surface can be captured by a continuous smooth

level set function, which has the features of a signed distance function. At one phase of flow the level set function has positive distance from the free surface, negative distance at another phase, and zero level corresponds to the free surface. The LS method can treat highly distorted interfaces. Also, the topology changes are incorporated automatically (Fekken, 2004). Sussman et al. (1994) solved incompressible two phase fluid problems based on the LS approach. Walhorn et al. (2005) simulated the 2D fluid-structure interaction problems using the LS method. However, mass conservation errors occurred in the numerical presentation of the advection equation for the determination of the level set function (Sussman and Fatemi, 1999).

The Constrained Interpolation Profile (CIP) method, developed by Yabe et al. (2001) based on the work of Takewaki et al. (1985), Yabe et al. (1991) and Yabe (1991), is a high order upwind scheme for capturing free surfaces. The CIP method uses a fixed, Eulerian grid as the basis for computations. It also employs a Lagrangian solution to determine the function value at the upstream departure point at the new time step, depending on an interpolation function of the initial profile. The CIP method uses both the advection function and its spatial derivatives to construct the high order interpolation function within one grid cell so that the interface profile inside the grid is retrieved. The CIP method, as an interface capturing method, does not need an adaptive grid system and therefore removes the problems of grid distortion caused by interface breakup and topology change. Furthermore, the scheme can treat multi-phase problems and it can handle large discontinuities or large gradients at the interface of different phases because of its compact scheme characteristics (Yabe et al., 2001). A pressure-based algorithm coupled with CIP has been proven to be stable and robust in solving the 2D slamming problem (Hu and Kashiwagi, 2004). The validation and verification of 2D CIP method were presented by Vestbøstad et al. (2007), and the numerical result showed that the CIP method was both robust and accurate for capturing violent free surface flows. Zhu et al. (2005) studied the water entry and the exit of a horizontal circular cylinder with the CIP algorithm

in the 2D computational domain. Yang and Qiu (2007) solved the 2D water entry problems of symmetric and asymmetric wedges with various deadrise angles using the CIP method. The effect of compressible air for 2D wedges with small deadrise angles were studied (Yang and Qiu, 2008).

From the literature review, it can be seen that many experimental, analytical, and numerical studies of slamming have been carried out. The vast majority of the work is, however, restricted to two-dimensional bodies and simple axisymmetric bodies. Relatively few attempts have been made to rigorously solve impact problems of 3D bodies. Some researches on 3D impact problems were conducted by Troesch and Kang (1986). They numerically studied impact loads on three-dimensional bodies using the boundary element method. In the three-dimensional computations, normal dipole distributions and an equi-potential free surface were used, and the results were compared with experimental results. Faltinsen and Chezhian (2005) presented a numerical method for three-dimensional slamming problems based on the generalized Wagner method. Thoroddsen et al. (2004) studied the initial stage of the impact of a solid sphere into a water surface using a novel ultra-high-speed video camera. There is a need to further develop three-dimensional methods to solve the slamming problems since most of water entry phenomena are three-dimensional.

1.3 Present Work

Present research work focuses on the development of a numerical simulation tool for highly nonlinear water impact problems. In particular, the phenomenon of slamming on 3D ship hulls, which has caught the interests of many marine engineers and naval architects for a long time, is an important motivation. More precisely, the main objective of this thesis is to develop a method to solve 3D slamming problems by addressing the following aspects:

Three-dimensional flow effects. The physics of slamming problems is extremely complex since it involves breaking waves and jets, etc. Due to the challenges of the realistic physical problem and the numerical technology, the vast majority of this work has been restricted to 2D or simple wedge-type bodies. Relatively few attempts have been made to rigorously solve impact problems of 3D bodies. This work aims at developing a numerical technique to investigate 3D nonlinear free surface flow effects in the slamming problem. In the research, the 2D Constrained Interpolation Profile (CIP) method (Yang, 2007) is further developed to simulate the 3D nonlinear free surface problems.

Coupled motion simulation. In order to simulate the slamming problem more realistically, the coupled motion of a 3D body and fluid has to be solved as well. Therefore, a method has to be developed that is capable of handling freely moving bodies. The coupling motion simulation poses more challenging work. The body velocity is unknown before the solution for the fluid is found. The accuracy of the pressure will be fed back through the fluid flow via the calculation of the body motion. Inaccurate pressure can cause false body response. One of the aims of this work is to overcome these difficulties and accurately predict the body motion and the violent flow phenomena during water entry. In this research, slamming forces and moments are obtained from the Navier-Stokes equations which are solved by a CIP-based finite difference method. The motion of a solid body is predicted by numerical integration of differential equations of motions considering the computed slamming forces as external forces. The fluid velocities due to the body motion are calculated, and they are then used for the free surface simulation using the CIP method. By solving the body and fluid motions simultaneously, the coupled motions are computed in the time domain.

Three-dimensional moving body interface treatment. To distinguish the flow and solid geometry on a fixed Cartesian grid, the volume fraction of solid body in

each Cartesian grid cell must be calculated accurately, which is important for the computation of fluid-structure interaction problems using the Eulerian grid method. However, allowing arbitrary 3D geometry (i.e., a realistic ship), the computation of volume fraction can become very complex. Especially, considering not only translating, but also rotating bodies, the situation becomes somewhat more complicated. Therefore, it will be important to develop a geometry reconstruction method that will compute the volume fraction accurately. In this research, a panel-based numerical method is developed to capture the arbitrary solid geometries. The body surface is represented by a set of panels. Since the body is assumed to be rigid, the panels can be used to update the body position with a Lagrangian method in each time step. The contribution of each panel is estimated by the contribution factor in each computational grid cell. Then the density function for a solid body is obtained, and the solid phase is modeled in a fixed computational grid.

1.4 Outline of the Thesis

The thesis presents the numerical solution of slamming for 3D bodies entering calm water. The highly nonlinear water entry problems are governed by the Navier-Stokes equations and are solved by a Constrained Interpolation Profile (CIP)-based finite difference method on a fixed Cartesian grid. The CIP method is employed for the advection calculations and a pressure-based algorithm is applied for the non-advection calculations. The solid body and free surface interfaces are captured by density functions. The motion of a body is described in terms of six degrees of freedom. For the pressure computation, a Poisson-type equation is solved at each time step by the Conjugate Gradient iterative method.

Chapter 2 introduces the computational method. The Navier Stokes equations are described as the governing equations. The fractional step method is introduced,

and the governing equations are split into three-different phases. The CIP method is discussed in details and the upwind cubic interpolation functions are given. A Poisson equation of pressure is derived based on a pressure-based method, and a Conjugate Gradient iterative method and Jacobi preconditioning are introduced. Free surface and moving body interface modeling methods are explained. The numerical method for coupled motion of a solid body and fluid is described. The computational methods for hydrodynamic forces and moments are provided.

In Chapter 3, a verification of the numerical method is presented. The added mass of a sphere was computed and compared with the analytical solution based on potential flow theory. Convergence studies of grid spacing and time step were conducted. Validation studies are described for several 3D solid bodies entering calm water with prescribed drop velocities. The computations were carried out for a 3D wedge entering calm water with a vertical velocity. The slamming force was calculated and compared with experimental results. Three-dimensional flow effects were discussed. The present method was also applied to a 3D ship section entering calm water vertically. The predicted slamming loads were compared with experimental results. The oblique water entry of a sphere was studied. The vertical and horizontal slamming forces were calculated for different drop velocities and were compared with experimental results and other numerical solutions. Studies were also extended to the water entry of a 3D planing hull at various pitch and roll angles. The 3D results were compared with the solutions based on the strip theory and 2D CIP method.

Three-dimensional bodies entering calm water with free-fall motions are studied in Chapter 4. The water entry of a 3D half-buoyant cylinder and a 3D neutrally buoyant cylinder were carried out. The predicted motions of the cylinders were compared with experimental data. The water entry of a 3D catamaran model with free-fall motion was also simulated. The variations of the ratio of hull velocities were computed and compared with experimental results. The asymmetric water entry of a 3D ship

section was simulated, and the computed accelerations and velocities were compared with experimental results.

In Chapter 5, this thesis ends with a summary and conclusions. Some future perspectives are also given.

Chapter 2

Mathematical Formulation

2.1 Governing Equations

An Earth-fixed Cartesian coordinate system is applied, z-axis pointing upward, see Fig. 2-1. The differential equations governing the unsteady motion of a viscous fluid are given as follows:

$$\frac{\partial \rho}{\partial t} + u_i \frac{\partial \rho}{\partial x_i} = -\rho \frac{\partial u_i}{\partial x_i} \tag{2.1}$$

$$\frac{\partial u_i}{\partial t} + u_j \frac{\partial u_i}{\partial x_j} = -\frac{1}{\rho} \frac{\partial \sigma_{ij}}{\partial x_j} + f_i^b \tag{2.2}$$

where t is the time; x_i $(i = 1, 2, 3)$ are the coordinates in a Cartesian coordinate system; ρ is the mass density; u_i are the velocity components; f_i^b is the gravity force.

For a Newtonian fluid, the total stress can be written as

$$\sigma_{ij} = -p\delta_{ij} + 2\mu S_{ij} - 2\mu\delta_{ij}S_{kk}/3$$

$$S_{ij} = \frac{1}{2}(\frac{\partial u_i}{\partial x_j} + \frac{\partial u_j}{\partial x_i})$$

where μ is the dynamic viscosity coefficient and δ_{ij} is Kronecker delta function.

The equation of state (EOS) is written as $p = f(\rho)$. Applying the EOS to Eq. (2.1), the pressure equation can be obtained as

$$\frac{\partial p}{\partial t} + u_i\frac{\partial p}{\partial x_i} = -\rho c_s^2\frac{\partial u_i}{\partial x_i} \tag{2.3}$$

where, $c_s = \sqrt{\partial p/\partial\rho}$ is the sound speed, and p is the pressure.

If turbulent flows are considered, the equations can be averaged over the time scale of turbulence and additional equations describing the Reynolds stresses need to be introduced. Since slamming is a transient problem, the significant turbulent effects do not have time to develop during the rapid impacts (Faltinsen et al., 2004). The laminar flow is assumed in the studies for the slamming problem based on the work of Zhu et al. (2005).

A fixed rectangular computational domain is used in the present computation, see Fig. 2-1. An exterior fictitious one cell layer to each side of the physical domain is added to allow imposition of discrete boundary conditions. The pressure along the top of the computational domain is set to zero. No-slip wall boundary conditions are applied to the domain sides. For a water entry problem, if the domain boundaries are far enough from the body, the existence of the boundary will not give significant influence during the rapid water entry process. Computational domain including the geometry of a moving body, air and water, is divided into regular cubic grids. The solid body boundary is immersed in the fixed Cartesian grid with a fractional volume or area representation technique (See Section 2.5). The solid body is set up

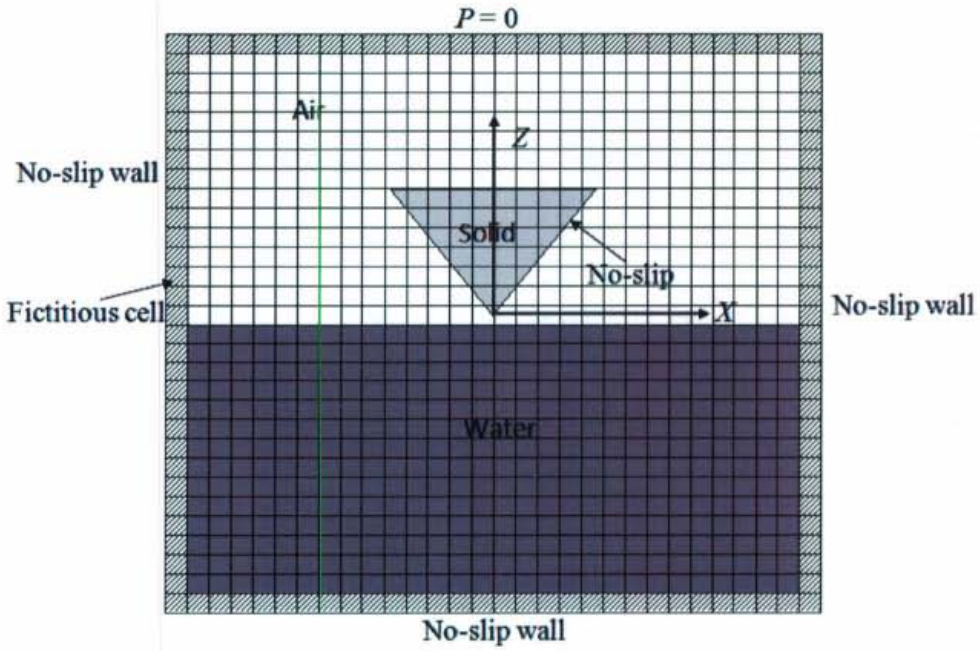

Figure 2-1: A fixed Cartesian grid for a multiple phase domain

as a moving object with a drop velocity and its contour is defined as a no-slip wall condition (See Eq. 2.100). This approach allows for a complex geometry without a time consuming grid generation as for a boundary-fitted coordinate (BFC) method. It is well known that BFC grids can be difficult to construct and it takes a significant amount of time to establish a workable and well-behaved grid even with good grid generators. The present numerical method is described in details in the following Sections.

2.2 Discretization Method

Applying the fractional step approach to Eqs. 2.1 to 2.3 leads to the numerical solutions of governing equations in three steps as follows (Hu and Kashiwagi, 2004).

1. Advection phase

$$\frac{\rho^* - \rho^n}{\Delta t} + u_i^n \frac{\partial \rho^n}{\partial x_i} = 0 \tag{2.4}$$

$$\frac{u_i^* - u_i^n}{\Delta t} + u_j^n \frac{\partial u_i^n}{\partial x_j} = 0 \tag{2.5}$$

$$\frac{p^* - p^n}{\Delta t} + u_i^n \frac{\partial p^n}{\partial x_i} = 0 \tag{2.6}$$

2. Non-advection phase I

$$\frac{u_i^{**} - u_i^*}{\Delta t} = \frac{2\mu}{\rho^*} \frac{\partial}{\partial x_j} (S_{ij}^* - \frac{1}{3}\delta_{ij} S_{kk}^*) + f_i^b \tag{2.7}$$

3. Non-advection phase II

$$\frac{\rho^{n+1} - \rho^*}{\Delta t} = -\rho^* \frac{\partial u_i^{n+1}}{\partial x_i} \tag{2.8}$$

$$\frac{u_i^{n+1} - u_i^{**}}{\Delta t} = -\frac{1}{\rho^*} \frac{\partial p^{n+1}}{\partial x_i} \tag{2.9}$$

$$\frac{p^{n+1} - p^*}{\Delta t} = -\rho^* c_s^2 \frac{\partial u_i^{n+1}}{\partial x_i} \tag{2.10}$$

where the superscripts $*$ and $**$ indicate the intermediate values after the calculations of advection phase and non-advection I phase. The superscript $n+1$ indicates the final values at the new time step. The fractional steps in the present numerical method are arranged in the order of advection phase, non-advection phase I, and non-advection

phase II.

The equations in the advection phase are computed by the CIP method which will be introduced in Section 2.4.

For an incompressible fluid, the non-advection phase I, Eq. 2.7, can be expanded as follows:

$$\frac{u^{**} - u^{*}}{\Delta t} = \frac{\mu}{\rho}\left(\frac{\partial^2 u^{*}}{\partial x^2} + \frac{\partial^2 u^{*}}{\partial y^2} + \frac{\partial^2 u^{*}}{\partial z^2}\right) \tag{2.11}$$

$$\frac{v^{**} - v^{*}}{\Delta t} = \frac{\mu}{\rho}\left(\frac{\partial^2 v^{*}}{\partial y^2} + \frac{\partial^2 v^{*}}{\partial x^2} + \frac{\partial^2 v^{*}}{\partial z^2}\right) \tag{2.12}$$

$$\frac{w^{**} - w^{*}}{\Delta t} = \frac{\mu}{\rho}\left(\frac{\partial^2 w^{*}}{\partial z^2} + \frac{\partial^2 w^{*}}{\partial x^2} + \frac{\partial^2 w^{*}}{\partial y^2}\right) - g \tag{2.13}$$

where g is the gravity acceleration.

An Euler explicit scheme is used for the time integration for the left-hand-side terms of Eqs. 2.11 to 2.13 and a central finite difference scheme is used to discretize the terms on the right-hand-side of these equations. The velocities in non-advection I can be obtained as follows:

$$u^{**} = u^{*} + \frac{\mu \Delta t}{\rho}\left(\frac{\partial^2 u^{*}}{\partial x^2} + \frac{\partial^2 u^{*}}{\partial y^2} + \frac{\partial^2 u^{*}}{\partial z^2}\right) \tag{2.14}$$

$$v^{**} = v^{*} + \frac{\mu \Delta t}{\rho}\left(\frac{\partial^2 v^{*}}{\partial y^2} + \frac{\partial^2 v^{*}}{\partial x^2} + \frac{\partial^2 v^{*}}{\partial z^2}\right) \tag{2.15}$$

$$w^{**} = w^{*} + \frac{\mu \Delta t}{\rho}\left(\frac{\partial^2 w^{*}}{\partial z^2} + \frac{\partial^2 w^{*}}{\partial x^2} + \frac{\partial^2 w^{*}}{\partial y^2}\right) - g\Delta t \tag{2.16}$$

These second-order derivatives in Eqs. 2.14 to 2.16 can be approximated by:

$$\frac{\partial^2 u^*}{\partial x^2} = \frac{(u^*_{i+1,j,k} - u^*_{i,j,k})/\Delta x - (u^*_{i,j,k} - u^*_{i-1,j,k})/\Delta x}{\Delta x}$$

$$\frac{\partial^2 u^*}{\partial y^2} = \frac{(u^*_{i,j+1,k} - u^*_{i,j,k})/\Delta y - (u^*_{i,j,k} - u^*_{i,j-1,k})/\Delta y}{\Delta y}$$

$$\frac{\partial^2 u^*}{\partial z^2} = \frac{(u^*_{i,j,k+1} - u^*_{i,j,k})/\Delta z - (u^*_{i,j,k} - u^*_{i,j,k-1})/\Delta z}{\Delta z}$$

$$\frac{\partial^2 v^*}{\partial x^2} = \frac{(v^*_{i+1,j,k} - v^*_{i,j,k})/\Delta x - (v^*_{i,j,k} - v^*_{i-1,j,k})/\Delta x}{\Delta x}$$

$$\frac{\partial^2 v^*}{\partial y^2} = \frac{(v^*_{i,j+1,k} - v^*_{i,j,k})/\Delta y - (v^*_{i,j,k} - v^*_{i,j-1,k})/\Delta y}{\Delta y}$$

$$\frac{\partial^2 v^*}{\partial z^2} = \frac{(v^*_{i,j,k+1} - v^*_{i,j,k})/\Delta z - (v^*_{i,j,k} - v^*_{i,j,k-1})/\Delta z}{\Delta z}$$

$$\frac{\partial^2 w^*}{\partial x^2} = \frac{(w^*_{i+1,j,k} - w^*_{i,j,k})/\Delta x - (w^*_{i,j,k} - w^*_{i-1,j,k})/\Delta x}{\Delta x}$$

$$\frac{\partial^2 w^*}{\partial y^2} = \frac{(w^*_{i,j+1,k} - w^*_{i,j,k})/\Delta y - (w^*_{i,j,k} - w^*_{i,j-1,k})/\Delta y}{\Delta y}$$

$$\frac{\partial^2 w^*}{\partial z^2} = \frac{(w^*_{i,j,k+1} - w^*_{i,j,k})/\Delta z - (w^*_{i,j,k} - w^*_{i,j,k-1})/\Delta z}{\Delta z}$$

For the non-advection phase II, in a general way, the density ρ is solved first, and then the pressure can be calculated based on the density. Since the speed of sound, $c_s = \sqrt{\partial p/\partial \rho}$, is very large for solid or liquid phases, a small density error can lead to a large pressure pulse, and it tends to cause a dispersion error in numerical simulation. A pressure-based algorithm (Yabe, 1991) is employed to overcome this problem. In the pressure-based method, a Poisson-type pressure equation can be obtained by taking the divergence of Eq. 2.9 and substituting $\partial u_i/\partial x_i$ into Eq. 2.10,

$$\frac{\partial}{\partial x_i}\left(\frac{1}{\rho^*}\frac{\partial p^{n+1}}{\partial x_i}\right) = \frac{p^{n+1} - p^*}{\rho^* c_s^2 \Delta t^2} + \frac{1}{\Delta t}\frac{\partial u_i^{**}}{\partial x_i} \tag{2.17}$$

Eq. 2.17 shows that $\nabla p/\rho$ is continuous at sharp discontinuities. In this case, if the density changes by several orders of magnitude at the boundary, for example, between liquid and gas, the pressure gradient can be calculated accurately enough to ensure the continuous change. The equation is very robust even with a density ratio larger than 1000 and the multi-phase computations can be carried out.

For a perfect incompressible fluid, we can assume $c_s = \infty$, a simpler Poisson equation can be obtained as below:

$$\frac{\partial}{\partial x_i}\left(\frac{1}{\rho^*}\frac{\partial p^{n+1}}{\partial x_i}\right) = \frac{1}{\Delta t}\frac{\partial u_i^{**}}{\partial x_i} \tag{2.18}$$

In the computation, the velocity inside the body is forced to be equal to the rigid body velocity before solving Eq. 2.18. The solution of Eq. 2.18 provides the pressure distribution in the whole computational domain. Note that the pressure distribution obtained inside the solid body is a fictitious one, which satisfies the divergence free condition of the velocity field (Hu and Kashiwagi, 2007), and is consistent with the pressure on the body surface. These points inside the body are denoted as ghost points. The reason for doing this is from a practical computational point of view. With this treatment, the boundary condition for pressure at the interface between

different phases is not required.

The central finite difference method is used for the velocity derivatives on the right-hand-side of Eq. 2.18.

$$\frac{\partial u_i^{**}}{\partial x_i} = \frac{\partial u^{**}}{\partial x} + \frac{\partial v^{**}}{\partial y} + \frac{\partial w^{**}}{\partial z} = \frac{u_{i+1,j,k}^{**} - u_{i-1,j,k}^{**}}{2\Delta x} + \frac{v_{i,j+1,k}^{**} - v_{i,j-1,k}^{**}}{2\Delta y} + \frac{w_{i,j,k+1}^{**} - w_{i,j,k-1}^{**}}{2\Delta z} \tag{2.19}$$

The pressure terms on the left-hand-side can be re-written as:

$$\frac{\partial}{\partial x_i}(\frac{1}{\rho^*}\frac{\partial p^{n+1}}{\partial x_i}) = \frac{\partial}{\partial x}(\frac{1}{\rho^*}\frac{\partial p^{n+1}}{\partial x}) + \frac{\partial}{\partial y}(\frac{1}{\rho^*}\frac{\partial p^{n+1}}{\partial y}) + \frac{\partial}{\partial z}(\frac{1}{\rho^*}\frac{\partial p^{n+1}}{\partial z}) \tag{2.20}$$

We start to apply the central finite difference method to the first term on the right-hand-side of Eq. 2.20. This can be done by first approximating $\frac{1}{\rho^*}\frac{\partial p^{n+1}}{\partial x}$ at points halfway between the grid points, using a centered approximation,

$$\frac{1}{\rho^*}\frac{\partial p^{n+1}}{\partial x} = \frac{1}{\rho^*_{i+1/2,j,k}}\frac{p_{i+1,j,k}^{n+1} - p_{i,j,k}^{n+1}}{\Delta x} \tag{2.21}$$

and then applying another central finite difference method to approximate the derivatives of this quantity,

$$\begin{aligned}\frac{\partial}{\partial x}(\frac{1}{\rho^*}\frac{\partial p^{n+1}}{\partial x}) &= \frac{1}{\Delta x}(\frac{1}{\rho^*_{i+1/2,j,k}}\frac{p_{i+1,j,k}^{n+1} - p_{i,j,k}^{n+1}}{\Delta x} - \frac{1}{\rho^*_{i-1/2,j,k}}\frac{p_{i,j,k}^{n+1} - p_{i-1,j,k}^{n+1}}{\Delta x}) \\ &= \frac{1}{\Delta^2 x}[\frac{1}{\rho^*_{i+1/2,j,k}}p_{i+1,j,k}^{n+1} - (\frac{1}{\rho^*_{i+1/2,j,k}} + \frac{1}{\rho^*_{i-1/2,j,k}})p_{i,j,k}^{n+1} + \frac{1}{\rho^*_{i-1/2,j,k}}p_{i-1,j,k}^{n+1}]\end{aligned} \tag{2.22}$$

Applying the same method to the second and third terms on the right-hand-side of

Eq. 2.20 leads to the following equations.

$$\frac{\partial}{\partial y}(\frac{1}{\rho^*}\frac{\partial p^{n+1}}{\partial y}) = \frac{1}{\Delta y}(\frac{1}{\rho^*_{i,j+1/2,k}}\frac{p^{n+1}_{i,j+1,k}-p^{n+1}_{i,j,k}}{\Delta y} - \frac{1}{\rho^*_{i,j-1/2,k}}\frac{p^{n+1}_{i,j,k}-p^{n+1}_{i,j-1,k}}{\Delta y})$$
$$= \frac{1}{\Delta^2 y}[\frac{1}{\rho^*_{i,j+1/2,k}}p^{n+1}_{i,j+1,k} - (\frac{1}{\rho^*_{i,j+1/2,k}} + \frac{1}{\rho^*_{i,j-1/2,k}})p^{n+1}_{i,j,k} + \frac{1}{\rho^*_{i,j-1/2,k}}p^{n+1}_{i,j-1,k}] \quad (2.23)$$

and

$$\frac{\partial}{\partial z}(\frac{1}{\rho^*}\frac{\partial p^{n+1}}{\partial z}) = \frac{1}{\Delta z}(\frac{1}{\rho^*_{i,j,k+1/2}}\frac{p^{n+1}_{i,j,k+1}-p^{n+1}_{i,j,k}}{\Delta z} - \frac{1}{\rho^*_{i,j,k-1/2}}\frac{p^{n+1}_{i,j,k}-p^{n+1}_{i,j,k-1}}{\Delta z})$$
$$= \frac{1}{\Delta^2 z}[\frac{1}{\rho^*_{i,j,k+1/2}}p^{n+1}_{i,j,k+1} - (\frac{1}{\rho^*_{i,j,k+1/2}} + \frac{1}{\rho^*_{i,j,k-1/2}})p^{n+1}_{i,j,k} + \frac{1}{\rho^*_{i,j,k-1/2}}p^{n+1}_{i,j,k-1}] \quad (2.24)$$

Substituting Eqs. 2.22 to 2.24 into Eq. 2.18, yields,

$$\frac{\partial}{\partial x_i}(\frac{1}{\rho^*}\frac{\partial p^{n+1}}{\partial x_i}) = \frac{1}{\Delta^2 x}[\frac{1}{\rho^*_{i+1/2,j,k}}p^{n+1}_{i+1,j,k} - (\frac{1}{\rho^*_{i+1/2,j,k}} + \frac{1}{\rho^*_{i-1/2,j,k}})p^{n+1}_{i,j,k} + \frac{1}{\rho^*_{i-1/2,j,k}}p^{n+1}_{i-1,j,k}]$$
$$+ \frac{1}{\Delta^2 y}[\frac{1}{\rho^*_{i,j+1/2,k}}p^{n+1}_{i,j+1,k} - (\frac{1}{\rho^*_{i,j+1/2,k}} + \frac{1}{\rho^*_{i,j-1/2,k}})p^{n+1}_{i,j,k} + \frac{1}{\rho^*_{i,j-1/2,k}}p^{n+1}_{i,j-1,k}]$$
$$+ \frac{1}{\Delta^2 z}[\frac{1}{\rho^*_{i,j,k+1/2}}p^{n+1}_{i,j,k+1} - (\frac{1}{\rho^*_{i,j,k+1/2}} + \frac{1}{\rho^*_{i,j,k-1/2}})p^{n+1}_{i,j,k} + \frac{1}{\rho^*_{i,j,k-1/2}}p^{n+1}_{i,j,k-1}] \quad (2.25)$$

By rearranging Eq. 2.25, the final differential equation for pressure equation can be obtained as follows:

$$\frac{\partial}{\partial x_i}(\frac{1}{\rho^*}\frac{\partial p^{n+1}}{\partial x_i}) =$$
$$-p^{n+1}_{i,j,k}[\frac{1}{\Delta^2 x}(\frac{1}{\rho^*_{i+1/2,j,k}}+\frac{1}{\rho^*_{i-1/2,j,k}})+\frac{1}{\Delta^2 y}(\frac{1}{\rho^*_{i,j+1/2,k}}+\frac{1}{\rho^*_{i,j-1/2,k}})+\frac{1}{\Delta^2 z}(\frac{1}{\rho^*_{i,j,k+1/2}}+\frac{1}{\rho^*_{i,j,k-1/2}})]$$
$$+p^{n+1}_{i+1,j,k}(\frac{1}{\Delta^2 x}\frac{1}{\rho^*_{i+1/2,j,k}})+p^{n+1}_{i-1,j,k}(\frac{1}{\Delta^2 x}\frac{1}{\rho^*_{i-1/2,j,k}})+p^{n+1}_{i,j+1,k}(\frac{1}{\Delta^2 y}\frac{1}{\rho^*_{i,j+1/2,k}})$$
$$+p^{n+1}_{i,j-1,k}(\frac{1}{\Delta^2 y}\frac{1}{\rho^*_{i,j-1/2,k}})+p^{n+1}_{i,j,k+1}(\frac{1}{\Delta^2 z}\frac{1}{\rho^*_{i,j,k+1/2}})+p^{n+1}_{i,j,k-1}(\frac{1}{\Delta^2 z}\frac{1}{\rho^*_{i,j,k-1/2}}) \quad (2.26)$$

where $\rho^*_{i+1/2,j,k}=\frac{1}{2}(\rho^*_{i,j,k}+\rho^*_{i+1,j,k})$, $\rho^*_{i-1/2,j,k}=\frac{1}{2}(\rho^*_{i,j,k}+\rho^*_{i-1,j,k})$, $\rho^*_{i,j+1/2,k}=\frac{1}{2}(\rho^*_{i,j,k}+\rho^*_{i,j+1,k})$, $\rho^*_{i,j-1/2,k}=\frac{1}{2}(\rho^*_{i,j,k}+\rho^*_{i,j-1,k})$, $\rho^*_{i,j,k+1/2}=\frac{1}{2}(\rho^*_{i,j,k}+\rho^*_{i,j,k+1})$, and $\rho^*_{i,j,k-1/2}=\frac{1}{2}(\rho^*_{i,j,k}+\rho^*_{i,j,k-1})$.

A linear system of equations, $\mathbf{Ax}=\mathbf{b}$, can be obtained from Eq. 2.26 and Eq. 2.18, in which $\mathbf{x}$ is an unknown column vector of pressure, $\mathbf{b}$ is a known vector of velocity gradient components, and $\mathbf{A}$ is a known, square, symmetric, positive-definite matrix. A Conjugate Gradient (CG) iterative method is employed to solve the linear equations, and a Jacobi preconditioner is applied to improve the computation efficiency. A brief discussion on the CG algorithm and preconditioning is given in Appendix A.

After the pressure field is obtained by solving Eq. 2.18, the velocities in the new time step can be calculated by solving Eq. 2.9 in the whole computational domain.

$$\frac{u^{n+1}-u^{**}}{\Delta t}=-\frac{1}{\rho^*}\frac{p^{n+1}_{i+1,j,k}-p^{n+1}_{i-1,j,k}}{2\Delta x} \quad (2.27)$$

$$\frac{v^{n+1}-v^{**}}{\Delta t}=-\frac{1}{\rho^*}\frac{p^{n+1}_{i,j+1,k}-p^{n+1}_{i,j-1,k}}{2\Delta y} \quad (2.28)$$

$$\frac{w^{n+1} - w^{**}}{\Delta t} = -\frac{1}{\rho^*} \frac{p^{n+1}_{i,j,k+1} - p^{n+1}_{i,j,k-1}}{2\Delta z} \tag{2.29}$$

The velocities in new time step can be obtained, as follows, based on an Euler explicit scheme.

$$u^{n+1} = u^{**} - \frac{\Delta t}{\rho^*} \frac{p^{n+1}_{i+1,j,k} - p^{n+1}_{i-1,j,k}}{2\Delta x} \tag{2.30}$$

$$v^{n+1} = v^{**} - \frac{\Delta t}{\rho^*} \frac{p^{n+1}_{i,j+1,k} - p^{n+1}_{i,j-1,k}}{2\Delta y} \tag{2.31}$$

$$w^{n+1} = w^{**} - \frac{\Delta t}{\rho^*} \frac{p^{n+1}_{i,j,k+1} - p^{n+1}_{i,j,k-1}}{2\Delta z} \tag{2.32}$$

Note that under the incompressible fluid assumption, the density can be determined by density functions instead of solving Eq. 2.1, which will be introduced in next Section.

In the whole solution procedure for the governing equations, the computation of advection phase with the CIP method has no restriction on the CFL (Courant-Friedrich-Lewy) (See Section 2.4.1). The application of the explicit time integration scheme, i.e. Euler scheme, results in a CFL restriction for the time step size, $u\Delta t/\Delta x \leq 1$. The Euler explicit integration yields first-order accuracy in time integration of the governing equations. Central finite difference gives second-order accuracy in space integration. However, the fractional step method can cause splitting error, therefore the resulting method will be of first-order accuracy (Leveque, 2007).

2.3 Free Surface Modeling Method

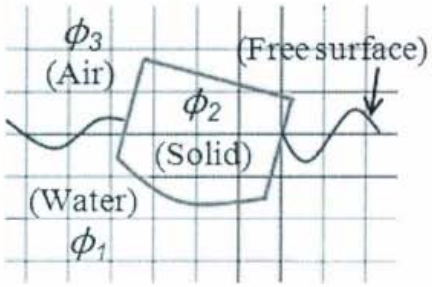

Figure 2-2: Multi-phase computational domain

In a multi-phase computation, in order to identify which part is occupied by water, solid body or air in the computational domain, a density function ϕ_m is introduced, which satisfies

$$0 \leq \phi_m(x, y, z, t) \leq 1 \quad \text{(x,y,z)} \in \Omega_m$$

where Ω_m, $m = 1$, 2, and 3, denotes the domain occupied by liquid, solid and air, respectively. The density functions have the value range of $\phi_m = [0.0, 1.0]$. If $\phi_1 = 1.0$, the cell is completely submerged in water; if $\phi_1 = 0$, no water is in the cell; if $0 < \phi_1 < 1$, the cell is partially submerged in water. For each cell, the density functions must fulfill the following requirement:

$$\sum_{m=1}^{3} \phi_m = 1.0 \tag{2.33}$$

There are two types of interfaces that need to be modeled in the computation, see Fig. 2-2. One is interface between air and water (the free surface), and the other is

the interface between solid body and water (or air). The behaviors of these two types of interface are different, and different numerical methods are used for each of them. The density function for water is advected with flow and the CIP method is thus used to propagate ϕ_1 with time (See Section 2.4). The body density function ϕ_2 is updated with a direct method under the assumption of a rigid body (See Section 2.5). The density function for air can thus be found by utilizing Eq. 2.33. Because the air and the water phases are modeled as a single fluid with varying properties (i.e. density, viscosity, etc.), there is no need to specify dynamic conditions in terms of stresses at the interface between air and water. The dynamic conditions are automatically satisfied.

After the density function for each phase is determined, the physical properties, such as viscosity and density, can be calculated as follows for each computational cell based on the incompressible flow assumption.

$$\rho = \phi_1 \rho_{water} + \phi_2 \rho_{ghost} + \phi_3 \rho_{air} \tag{2.34}$$

$$\mu = \phi_1 \mu_{water} + \phi_2 \mu_{ghost} + \phi_3 \mu_{air} \tag{2.35}$$

where ρ_{water} and ρ_{air} are the densities of water and air; μ_{water} and μ_{air} are the dynamic viscosities of water and air; and ρ_{ghost} and μ_{ghost} are the artificial density and viscosity for these ghost points inside the solid body. In the computation, $\rho_{ghost} = \rho_{water}$ and $\mu_{ghost} = \mu_{water}$.

The motion of free surface can be described by the following advection equation,

$$\frac{\partial \phi_1}{\partial t} + u_i \frac{\partial \phi_1}{\partial x_i} = 0 \tag{2.36}$$

The left-hand-side of Eq. 2.36 is the material derivative. Eq. 2.36 indicates that if we

follow a fluid particle, the property of the fluid particle does not change with time.

The finite difference schemes based on the Eulerian representation tend to produce numerical diffusion, which will smear the initial sharpness of the interface. In this work, a tangent function (Xiao, 1999) is used to transform the density function into a new function,

$$\emptyset(\phi_1) = \tan[(1-\epsilon)\pi(\phi_1 - 1/2)] \tag{2.37}$$

where ϵ is a small positive constant. The factor, 1-ϵ, enables us to get around $-\infty$ for $\phi_1 = 0$ and ∞ for $\phi_1 = 1$, and to tune for desired steepness of the transition layer. The parameter ϵ needs to be chosen artificially before calculation. In the present computation, $\epsilon = 0.02$. According to the tangent function, a smaller ϵ results in a numerically sharper slope across the transition layer.

The new function $\emptyset(\phi_1)$ is also governed by the advection equation

$$\frac{\partial \emptyset(\phi_1)}{\partial t} + u_i \frac{\partial \emptyset(\phi_1)}{\partial x_i} = 0 \tag{2.38}$$

Eq. 2.38 can be solved by the CIP method. The present work focuses on 3D bodies entering calm water. Therefore, the water is at rest initially before the body interacts with the water. Since the compact scheme of CIP method and its subcell resolution feature, the initial sharpness of the interface can be maintained very well in the whole computation process.

$$\phi_1 = \tan^{-1} \emptyset(\phi_1)/[(1-\epsilon)\pi] + 1/2 \tag{2.39}$$

The density function of water then can be obtained by Eq. 2.39. The value of ϕ_1 changes continuously between the values of air and water at the free surface during

the simulation.

2.4 CIP Method

2.4.1 Principle of the CIP Method

Using an upwind difference technique for the advection term of the Navier-Stokes equations can lead to a stable computation in CFD methods. However, the use of upwind schemes will introduce excessive numerical diffusion and associated inaccuracies. In the present computation, the advection equations of Eqs. 2.5 and 2.6 for velocities and pressure, and the advection equation of Eq. 2.38 for free surface, are solved by the CIP method to reduce the numerical diffusion and improve the accuracy of solution.

The Constrained Interpolation Profile (CIP) method developed by Yabe et al. (2001) based on the work of Takewaki et al. (1985), Yabe et al. (1991) and Yabe (1991), is a high order upwind scheme for solving the advection equation.

The CIP method can also be treated as a kind of semi-Lagrangian method. It traces back along the characteristics in a fixed Cartesian grid, and an interpolation of the profile is required to determine the value at the upstream departure point. The key aspect in the CIP method is that the interpolation function is constructed by both the function itself and its spatial derivatives. The strategy of the CIP method can be explained by using a 1D advection equation as follows:

$$\frac{\partial f}{\partial t} + u\frac{\partial f}{\partial x} = 0 \tag{2.40}$$

When the velocity is constant, the solution of the equation gives a simple translation

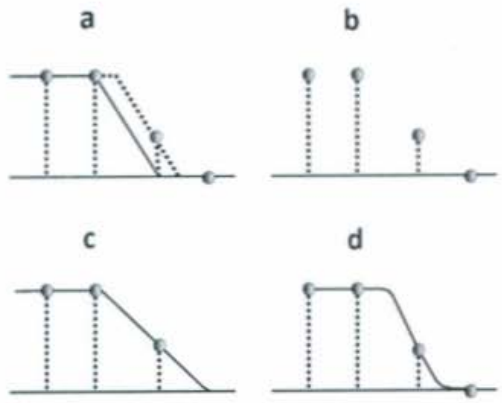

Figure 2-3: Principle of the CIP method (Yabe et al., 2001)

motion of profiles with a velocity u. As shown in Fig. 2-3, the initial profile moves like a dashed line in a continuous representation, and the solution at grid points denoted by the filled circles is the same as the exact solution. However, if the dashed line is eliminated as shown in Fig. 2-3 (b), the information of the profile inside the grid cell is lost. When the profile is constructed by a linear interpolation, it is natural to get a profile like that shown by the solid line in Fig. 2-3 (c), and numerical diffusion arises. The reason why this solution becomes worse is that the behavior of the solution inside grid cell is neglected. If the profile is approximated with a new numerical scheme to make the lost information inside a grid cell retrieved, the numerical solution will become better.

Differentiating Eq. 2.40 with respect to the spatial variable x, we can obtain,

$$\frac{\partial f_x}{\partial t} + u\frac{\partial f_x}{\partial x} = -\frac{\partial u}{\partial x} f_x \tag{2.41}$$

where, $f_x = \partial f/\partial x$ stands for the spatial derivative of f. For simplicity, a constant advection velocity u is assumed. Eq. 2.41 represents the propagation of spatial

derivative with a constant velocity u. Using Eqs. 2.40 and 2.41, the time evolution of f and f_x can be traced. Since the spatial derivative is used to approximate the propagation, the profile after one step is limited to a specific profile, even inside the grid cell. The solution becomes much closer to the real solution, as shown in Fig. 2-3 d.

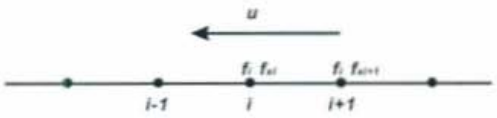

Figure 2-4: One dimensional grid

A high-order interpolation function can be constructed in an upwind grid using the values of f and f_x, see Fig. 2-4.

$$F(x) = a_i x^3 + b_i x^2 + c_i x + d_i$$

$$a_i = \frac{f^n_{x,i} + f^n_{x,i+1}}{\Delta x^2} + \frac{2(f^n_i - f^n_{i+1})}{\Delta x^3}$$

$$b_i = \frac{3(f^n_{i+1} - f^n_i)}{\Delta x^2} - \frac{2f^n_{x,i} + f^n_{x,i+1}}{\Delta x}$$

$$c_i = g^n_i$$

$$d_i = f^n_i$$

For $u > 0$, the subscript $i+1$ needs to be changed into $i-1$, and $\Delta x = -\Delta x$.

The profile at the $n+1$ step can then be obtained by shifting the profile by a distance of $u\Delta t$.

$$f^{n+1} = F(x - u\Delta t)$$

$$f_x^{n+1} = dF(x - u\Delta t)/dx$$

or,

$$f_i^{n+1} = a_i\xi_i^3 + b_i\xi_i^2 + g_i^n\xi_i + f_i^n \tag{2.42}$$

$$f_{x,i}^{n+1} = 3a_i\xi_i^2 + 2b_i\xi_i + g_i^n \tag{2.43}$$

where $\xi_i = -u\Delta t$, and Δt is the time step. Note that the right-hand-side of Eq. 2.41 must be calculated for a variable velocity, which will be discussed in Section 2.4.3.

The CIP method has been proved to have third-order accuracy in time and space by Taylor expansion (Utsumi et al., 1996). The construction of Eqs. 2.42 and 2.43 over a neighboring cell of the interested grid i implies CFL ≤ 1. In order to allow the use of a larger time step like other semi-Lagrangian methods, Eqs. 2.42 and 2.43 are modified by applying these to the far upwind grid cell (See the cell m in Fig. 2-5) from which the Lagrangian particle starts to the present position of concern (Yabe, 2000).

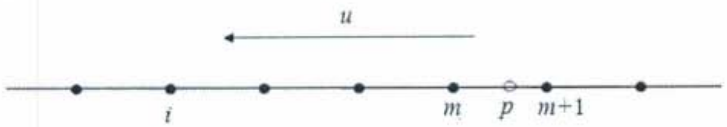

Figure 2-5: A far upwind cell in one dimensional grid

Eqs. 2.42 and 2.43 are modified to be

$$f_i^{n+1} = a_m \xi^3 + b_m \xi^2 + g_m^n \xi + f_m^n \tag{2.44}$$

$$f_{x,i}^{n+1} = 3a_m \xi^2 + 2b_m \xi + g_m^n \tag{2.45}$$

where m is the grid point determined by $x_m < x_p < x_{m+1}$ for $u \leq 0$ and $x_{m-1} < x_p < x_m$ for $u > 0$, and x_p is the particle position of upwind departure point which is calculated by

$$x_p = x_i + \int_{t+\Delta t}^{t} u dt$$

where ξ is the distance between these two points:

$$\xi = x_p - x_m$$

a_m and b_m are:

$$a_m = \frac{f_{x,m}^n + f_{x,m+1}^n}{\Delta x^2} + \frac{2(f_m^n - f_{m+1}^n)}{\Delta x^3}$$
$$b_m = \frac{3(f_{m+1}^n - f_m^n)}{\Delta x^2} - \frac{2f_{x,m}^n + f_{x,m+1}^n}{\Delta x}$$

We then get a semi-Lagrangian scheme that permits a large time step free from the restriction CFL ≤ 1.

With the special treatment of the spatial derivative, only two points are needed for constructing the high-order interpolation approximation in one grid cell. The CIP method achieves a compact form and provides subcell resolution. The key points of

the CIP method can be summarized as follows:

1. It is a compact upwind scheme with subcell resolution for advection calculations;
2. A cubic interpolation function is constructed, and a high-order scheme is achieved;
3. Since no re-meshing calculation is required, the computational time can usually be shortened for time dependent problems;
4. The CIP method does not involve any interface construction procedure and is quite economical in computational complexity, especially for 3D applications.

2.4.2 CIP Formulation in Multiple Dimensional Cases

A. 2D CIP Method

The governing equations for first-order spatial derivatives of the interpolation function in multi-dimensions are derived by differentiating the advection equation with respect to the spatial coordinates. The general forms of 2D advection equations can be written as follows:

$$\frac{\partial f}{\partial t} + u\frac{\partial f}{\partial x} + v\frac{\partial f}{\partial y} = 0 \tag{2.46}$$

$$\frac{\partial f_x}{\partial t} + u\frac{\partial f_x}{\partial x} + v\frac{\partial f_x}{\partial y} = 0 \tag{2.47}$$

$$\frac{\partial f_y}{\partial t} + u\frac{\partial f_y}{\partial x} + v\frac{\partial f_y}{\partial y} = 0 \tag{2.48}$$

The terms on the right-hand-sides of Eqs. 2.47 and 2.48 are included in the non-advection phase calculation of a fractional step approach as shown in Section 2.4.3.

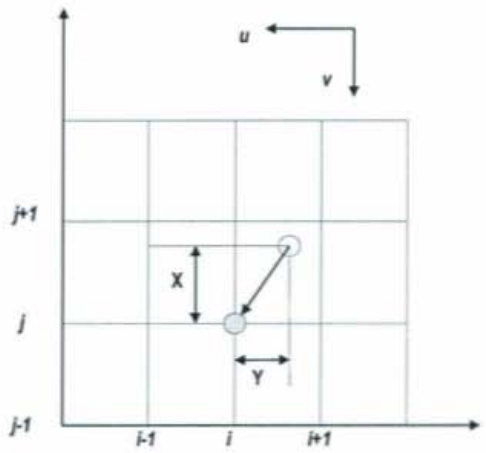

Figure 2-6: Two dimensional grid

Several forms of 2D cubic polynomial have been proposed. The simplest one proposed by Yabe et al. (2001) is given as follows, see Fig. 2-6. In this upwind cell, we assume $u < 0$, $v < 0$.

$$F(X,Y) = c_{30}X^3 + c_{21}X^2Y + c_{12}XY^2 + c_{03}Y^3 + c_{20}X^2 + c_{11}XY + c_{02}Y^2 + c_{10}X + c_{01}Y + c_{00} \tag{2.49}$$

$$F_x = 3c_{30}X^2 + 2c_{21}XY + c_{12}Y^2 + 2c_{20}X + c_{11}Y + c_{10} \tag{2.50}$$

$$F_y = c_{21}X^2 + 2c_{12}XY + 3c_{03}Y^2 + c_{11}X + 2c_{02}Y + c_{01} \tag{2.51}$$

where $X = -u\Delta t$, $Y = -v\Delta t$. There are ten unknown coefficients, C_{mn}, which will be determined as follows by the values of f, f_x, and f_y at grid points (i, j), $(i+1, j)$, $(i, j+1)$, and the value of f at the grid point $(i+1, j+1)$. These coefficients are given as follows:

$$c_{00} = f(i,j)$$

$$c_{01} = f_y(i,j)$$

$$c_{10} = f_x(i,j)$$

$$c_{30} = [\Delta x(f_x(i+1,j) + f_x(i,j)) - 2(f(i+1,j) - f(i,j))]/\Delta x^3$$

$$c_{20} = [-\Delta x(f_x(i+1,j) + 2f_x(i,j)) + 3(f(i+1,j) - f(i,j))]/\Delta x^2$$

$$c_{03} = [\Delta y(f_y(i,j+1) + f_y(i,j)) - 2(f(i,j+1) - f(i,j))]/\Delta y^3$$

$$c_{02} = [-\Delta y(f_y(i,j+1) + 2f_y(i,j)) + 3(f(i,j+1) - f(i,j))]/\Delta y^2$$

$$c_{21} = [f_x(i+1,j+1) - f_x(i+1,j) - f_x(i,j+1) + f_x(i,j)]/(2\Delta x\Delta y)$$

$$c_{12} = [f_y(i+1,j+1) - f_y(i+1,j) - f_y(i,j+1) + f_y(i,j)]/(2\Delta x\Delta y)$$

$$c_{11} = [f(i+1,j+1) - f(i+1,j) - f(i,j+1) + f(i,j)]/(\Delta x\Delta y) - c_{21}\Delta x - c_{12}\Delta y$$

The following changes are needed for $u \geq 0$ and $v \geq 0$: $i+1 \Rightarrow i-1$ and $\Delta x \Rightarrow -\Delta x$, $j+1 \Rightarrow j-1$ and $\Delta y \Rightarrow -\Delta y$.

B. 3D CIP Method

The general form of three-dimensional advection equations can be written as follows:

$$\frac{\partial f}{\partial t} + u\frac{\partial f}{\partial x} + v\frac{\partial f}{\partial y} + w\frac{\partial f}{\partial z} = 0 \tag{2.52}$$

$$\frac{\partial f_x}{\partial t} + u\frac{\partial f_x}{\partial x} + v\frac{\partial f_x}{\partial y} + w\frac{\partial f_x}{\partial z} = 0 \tag{2.53}$$

$$\frac{\partial f_y}{\partial t} + u\frac{\partial f_y}{\partial x} + v\frac{\partial f_y}{\partial y} + w\frac{\partial f_z}{\partial z} = 0 \tag{2.54}$$

$$\frac{\partial f_z}{\partial t} + u\frac{\partial f_z}{\partial x} + v\frac{\partial f_z}{\partial y} + w\frac{\partial f_z}{\partial z} = 0 \tag{2.55}$$

The terms on the right-hand-sides of Eqs. 2.52 to 2.54 are included in the non-advection phase calculation of a fractional step approach as shown in the next Section.

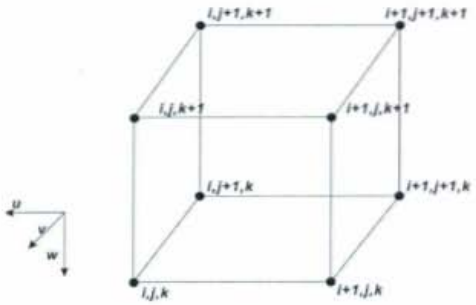

Figure 2-7: Upwind cubic grid cell

A cubic polynomial interpolation function is constructed in an upwind cell (Fig. 2-7) based on the work of Yabe (1991). In this upwind cell, it is assumed that $u < 0$,

$v < 0$ and $w < 0$.

$$\begin{aligned} F(x,y,z) = &[(c_1X + c_2Y + c_3Z + c_4)X + c_5Y + f_x(i,j,k)]X \\ &+ [(c_6Y + c_7Z + c_8X + c_9)Y + c_{10}Z + f_y(i,j,k)]Y \\ &+ [(c_{11}Z + c_{12}X + c_{13}Y + c_{14})Z + c_{15}X + f_z(i,j,k)]Z \\ &+ c_{16}XYZ + f_{i,j,k} \end{aligned} \tag{2.56}$$

where $X = -u\Delta t$, $Y = -v\Delta t$ and $Z = -w\Delta t$.

The 16 unknown coefficients are determined from the values of f, f_x, f_y and f_z at grid points $(i+1,j,k)$, $(i,j+1,k)$ and $(i,j,k+1)$ and that of f at points $(i+1,j+1,k)$, $(i,j+1,k+1)$, $(i+1,j,k+1)$ and $(i+1,j+1,k+1)$. These coefficients are given as follows:

$$c_1 = [-2D_i + \partial_x(f_{i+1,j,k} + f_{i,j,k})\Delta x]/\Delta x^3$$

$$c_2 = -[c_\alpha + \partial_x D_j \Delta x]/(\Delta x^2 \Delta y)$$

$$c_3 = -[c_\beta + \partial_x D_k \Delta x]/(\Delta x^2 \Delta z)$$

$$c_4 = [-3D_i - \partial_x(f_{i+1,j,k} + 2f_{i,j,k})\Delta x]/\Delta x^2$$

$$c_5 = -[c_\alpha + \partial_x D_j \Delta x + \partial_y D_i \Delta y]/(\Delta x \Delta y)$$

$$c_6 = [-2D_i - \partial_y(f_{i,j+1,k} + f_{i,j,k})\Delta y]/\Delta y^3$$

$$c_7 = -[c_\gamma + \partial_y D_k \Delta y]/(\Delta y^2 \Delta z)$$

$$c_8 = -[c_\alpha + \partial_y D_i \Delta y]/(\Delta x \Delta y^2)$$

$$c_9 = [3D_i - \partial_y(f_{i,j+1,k} + 2f_{i,j,k})\Delta y]/\Delta y^2$$

$$c_{10} = [c_\gamma + \partial_y D_k \Delta y + \partial_z D_j \Delta z](\Delta y \Delta z)$$

$$c_{11} = [-2D_k + \partial_z (f_{i,j,k+1} + f_{i,j,k})\Delta z]/\Delta z^2$$

$$c_{12} = -[c_\beta + \partial_z D_i \Delta z]/(\Delta x \Delta z^2)$$

$$c_{13} = -[c_\gamma + \partial_z D_j \Delta z]/(\Delta y \Delta z^2)$$

$$c_{14} = [3D_k - \partial_z (f_{i,j,k+1} + 2f_{i,j,k})\Delta z]/\Delta z^2$$

$$c_{15} = [c_\beta + \partial_z D_i \Delta z + \partial_x D_k \Delta x]/(\Delta x \Delta z)$$

$$c_{16} = [c_\alpha + f_{i,j,k+1} - (f_{i,j+1,k+1} + f_{i+1,j,k+1}) + f_{i+1,j+1,k+1}]/(\Delta x \Delta y \Delta z)$$

where $D_i = f_{i+1,j,k} - f_{i,j,k}$, $D_j = f_{i,j+1,k} - f_{i,j,k}$, $D_i = f_{i,j,k+1} - f_{i,j,k}$, $c_\alpha = -f_{i,j,k} + f_{i+1,j,k} + f_{i,j+1,k} - f_{i+1,j+1,k}$, $c_\beta = -f_{i,j,k} + f_{i+1,j,k} + f_{i,j,k+1} - f_{i+1,j,k+1}$, $c_\gamma = -f_{i,j,k} + f_{i,j+1,k} + f_{i,j,k+1} - f_{i,j+1,k+1}$.

Depending on the signs of u, v and w, the following changed can be made: $i+1 \Rightarrow i-1$ and $\Delta x \Rightarrow -\Delta x$ for $u \geq 0$, $j+1 \Rightarrow j-1$ and $\Delta y \Rightarrow -\Delta y$ for $v \geq 0$ and $j+1 \Rightarrow j-1$ and $\Delta z \Rightarrow -\Delta z$ for $w \geq 0$.

The interpolation functions for these spatial derivatives are then obtained.

$$\begin{aligned} F_x = {} & [3c_1 X + 2(c_2 Y + c_3 Z + c_4)]X \\ & + (c_7 Y + c_{16} Z + c_5)Y \\ & + (c_{12} Z + c_{15})Z \\ & + f_x \end{aligned} \tag{2.57}$$

$$
\begin{aligned}
F_y = & [3c_6Y + 2(c_7X + c_8Z + c_9)]Y \\
& + (c_{13}Z + c_{16}X + c_{10})Z \\
& + (c_2X + c_5)X \\
& + f_y
\end{aligned} \tag{2.58}
$$

$$
\begin{aligned}
F_z = & [3c_{11}Z + 2(c_{12}X + c_{13}Y + c_{14})]Z \\
& + (c_3X + c_{16}Y + c_{15})X \\
& + (c_8Y + c_{10})Y \\
& + f_z
\end{aligned} \tag{2.59}
$$

2.4.3 Calculation of Spatial Derivatives

In the CIP method, not only the function of f, but also its spatial derivatives, have to be updated at every time step.

Eqs. 2.5, 2.6 and Eq. 2.38 can be written in a general 3D form as follows. Note that 1D and 2D cases can follow the same procedure.

$$
\frac{\partial f}{\partial t} + u\frac{\partial f}{\partial x} + v\frac{\partial f}{\partial y} + w\frac{\partial f}{\partial z} = H \tag{2.60}
$$

where H denotes the total terms on the right-hand-sides of Eqs. 2.5 and 2.6.

Differentiating it with respect to x gives

$$
\frac{\partial^2 f}{\partial t \partial x} + \frac{\partial u}{\partial x}\frac{\partial f}{\partial x} + u\frac{\partial^2 f}{\partial x^2} + \frac{\partial v}{\partial x}\frac{\partial f}{\partial y} + v\frac{\partial^2 f}{\partial x \partial y} + \frac{\partial w}{\partial x}\frac{\partial f}{\partial z} + w\frac{\partial^2 f}{\partial x \partial z} = \frac{\partial H}{\partial x} \tag{2.61}
$$

Denoting $\frac{\partial f}{\partial x}$ as f_x, $\frac{\partial f}{\partial y}$ as f_y and $\frac{\partial f}{\partial z}$ as f_z, the above equation can be rewritten as

$$\frac{\partial f_x}{\partial t} + u\frac{\partial f_x}{\partial x} + v\frac{\partial f_x}{\partial y} + w\frac{\partial f_x}{\partial z} = \frac{\partial H}{\partial x} - (f_x\frac{\partial u}{\partial x} + f_y\frac{\partial v}{\partial x} + f_z\frac{\partial w}{\partial x}) \tag{2.62}$$

The left-hand-side of this equation is a 3D advection equation for f_x. The right-hand-side of this equation is a source term.

Applying the fractional step method to the above equations leads to

$$\frac{f^* - f^n}{\Delta t} + u^n\frac{\partial f^n}{\partial x} + v^n\frac{\partial f^n}{\partial y} + w^n\frac{\partial f^n}{\partial z} = 0 \tag{2.63}$$

$$\frac{f_x^* - f_x^n}{\Delta t} + u^n\frac{\partial f_x^n}{\partial x} + v^n\frac{\partial f_x^n}{\partial y} + w^n\frac{\partial f_x^n}{\partial z} = 0 \tag{2.64}$$

$$\frac{f^{n+1} - f^*}{\Delta t} = H \tag{2.65}$$

$$\frac{f_x^{n+1} - f_x^*}{\Delta t} = \frac{\partial H}{\partial x} - (f_x^*\frac{\partial u^n}{\partial x} + f_y^*\frac{\partial v^n}{\partial x} + f_z^*\frac{\partial w^n}{\partial x}) \tag{2.66}$$

Eqs. 2.63 and 2.64 are solved by the CIP method described in Section 2.4.2, and f^* and f_x^* are obtained by Eqs. 2.56 and 2.57.

Differentiating Eq. 2.65 with respect to x yields

$$\begin{aligned}\frac{\partial H}{\partial x} = \frac{f_x^{n+1} - f_x^*}{\Delta t} &= (\frac{f_{i+1,j,k}^{n+1} - f_{i-1,j,k}^{n+1}}{2\Delta x} - \frac{f_{i+1,j,k}^* - f_{i-1,j,k}^*}{2\Delta x})/\Delta t \\ &= \frac{f_{i+1,j,k}^{n+1} - f_{i-1,j,k}^{n+1} - f_{i+1,j,k}^* + f_{i-1,j,k}^*}{2\Delta t\Delta x}\end{aligned} \tag{2.67}$$

Substituting Eq. 2.67 into Eq. 2.66, the final equation for f_x^{n+1} can be obtained,

$$\frac{f_x^{n+1} - f_x^*}{\Delta t} = \frac{f_{i+1,j,k}^{n+1} - f_{i-1,j,k}^{n+1} - f_{i+1,j,k}^* + f_{i-1,j,k}^*}{2\Delta t \Delta x} - (f_x^* \frac{\partial u^n}{\partial x} + f_y^* \frac{\partial v^n}{\partial x} + f_z^* \frac{\partial w^n}{\partial x}) \quad (2.68)$$

and

$$\begin{aligned} f_x^{n+1} = f_x^* &+ \frac{f_{i+1,j,k}^{n+1} - f_{i-1,j,k}^{n+1} - f_{i+1,j,k}^* + f_{i-1,j,k}^*}{2\Delta x} \\ &- \Delta t(f_x^* \frac{u_{i+1,j,k}^n - u_{i-1,j,k}^n}{2\Delta x} + f_y^* \frac{v_{i+1,j,k}^n - v_{i-1,j,k}^n}{2\Delta x} + f_z^* \frac{w_{i+1,j,k}^n - w_{i-1,j,k}^n}{2\Delta x}) \end{aligned} \quad (2.69)$$

Similarly, f_y^{n+1} and f_z^{n+1} can be obtained as follows:

$$\begin{aligned} f_y^{n+1} = f_y^* &+ \frac{f_{i,j+1,k}^{n+1} - f_{i,j-1,k}^{n+1} - f_{i,j+1,k}^* + f_{i,j-1,k}^*}{2\Delta y} \\ &- \Delta t(f_x^* \frac{u_{i,j+1,k}^n - u_{i,j-1,k}^n}{2\Delta y} + f_y^* \frac{v_{i,j+1,k}^n - v_{i,j-1,k}^n}{2\Delta y} + f_z^* \frac{w_{i,j+1,k}^n - w_{i,j-1,k}^n}{2\Delta y}) \end{aligned} \quad (2.70)$$

$$\begin{aligned} f_z^{n+1} = f_z^* &+ \frac{f_{i,j,k+1}^{n+1} - f_{i,j,k-1}^{n+1} - f_{i,j,k+1}^* + f_{i,j,k-1}^*}{2\Delta z} \\ &- \Delta t(f_x^* \frac{u_{i,j,k+1}^n - u_{i,j,k-1}^n}{2\Delta z} + f_y^* \frac{v_{i,j,k+1}^n - v_{i,j,k-1}^n}{2\Delta z} + f_z^* \frac{w_{i,j,k+1}^n - w_{i,j,k-1}^n}{2\Delta z}) \end{aligned} \quad (2.71)$$

2.5 Moving Body Interface Modeling Method

To distinguish the fluid and solid bodies in the Cartesian grid, the volume fraction of solid bodies in each Cartesian grid cell must be calculated accurately, which is important for the computation of fluid-structure interaction problem using the Eulerian grid methods.

Some numerical methods have been proposed for the treatment of arbitrary geometries in a fixed Cartesian grid. In the work of Fekken (2004), a moving body was presented by a number of marker points in space that were connected with straight lines forming a closed polygon, and a cut-cell method was used to calculate the volume fraction of a solid body at each cell.

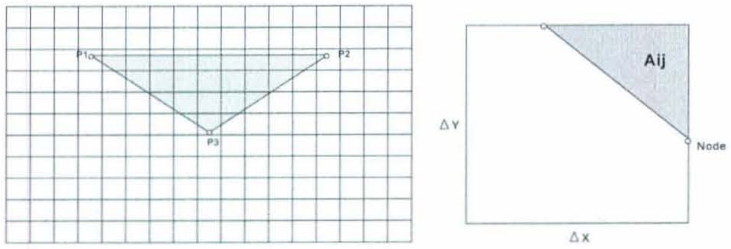

(a) 2D wedge in a fixed grid (b) Boundary cell

Figure 2-8: Calculation of density function for a 2D wedge

A similar method was used in the work of Yang (2007). In his work, a density function was induced to represent the solid body, and a cut-cell method was used to compute the density function. Taking a 2D wedge as an example, the coordinates of the three corner points of the wedge (P_1, P_2, P_3) are updated by a Lagrangian method at each time step, as shown in Fig. 2-8 (a). For each computational cell, if there are more than two nodes intersected by the body surface, the cell is considered one including the solid body boundary, and the area of the solid body in this cell is computed to determine $\phi_{2,ij}$, as shown in Fig. 2-8 (b).

$$\phi_{2,ij} = A_{ij}/\Delta x_i/\Delta y_j$$

It is convenient and accurate to compute the density function in 2D, but the computation in 3D will become very complex. In this work, a panel-based numerical method for modeling arbitrary 3D moving bodies in a fixed Cartesian grid is developed, and described in the following sections.

2.5.1 Generation of Panels

The body surface is represented by a set of panels instead of marker points. The panel can be triangular, quadrilateral or hybrid of them. The distribution of panels is important for the accurate representation of the geometry. Panels should be concentrated at the corners and locations with large curvatures. Based on the work of Qiu et al. (2003), the panel distribution can be controlled by two controlling functions. The controlling function for points concentrated at two ends is defined by Eq. 2.72,

$$\varphi(\xi) = \frac{(2\alpha+\beta)[(\beta+1)/(\beta-1)]^{(\xi-\alpha)/(1-\alpha)} + 2\alpha - \beta}{(2\alpha+1)\{1+[(\beta+1)/(\beta-1)]^{(\xi-\alpha)/(1-\alpha)}\}} \tag{2.72}$$

where α and β are the gird distribution factor and stretching factor, respectively. When $\alpha = 0.5$, the panel will cluster evenly at both ends. The stretching factor, β, should be greater than one. The larger the value is, the less concentration of points at end edge will be achieved. Note that ξ is some values between 0 and 1.

The control function is illustrated by the following example. Ten points are to be distributed on a straight line with a length, L, and ξ_j is specified as

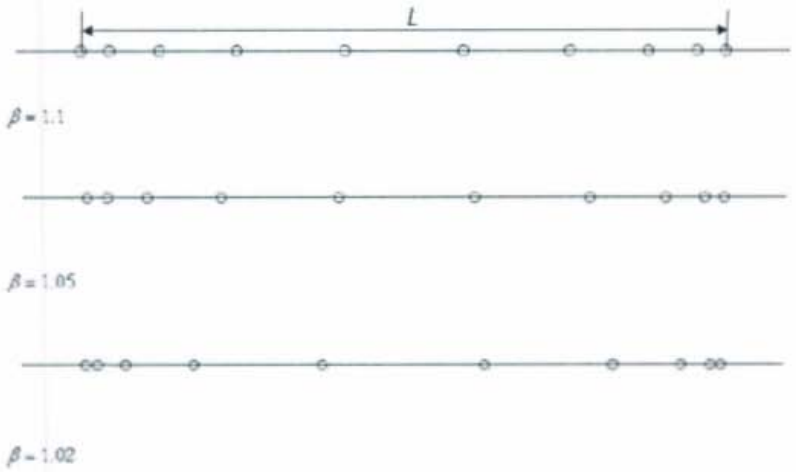

(a) Two-end distribution

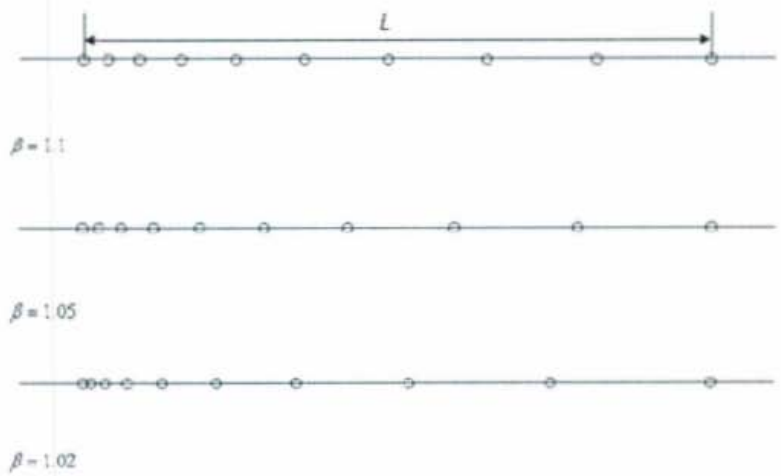

(b) One-end distribution

Figure 2-9: Point distributions on a line

$$\xi_j = \frac{j-1}{10-1}$$

where, $j = 1, 2, 3, ..., 10$. Then the coordinates of points can be obtained,

$$x(j) = L\varphi_i(\xi_j)$$

Fig. 2-9 (a) shows the distribution of points concentrated at two ends on a straight line with various values of β.

The controlling function for grid points concentrated at one end is defined by Eq. 2.73. Fig. 2-9 (b) shows the point distributions on a straight line with various values of β. The larger the value of β, the less concentration of points at the end edge will be achieved.

$$\varphi(\xi) = \frac{(\beta+1) - (\beta-1)[(\beta+1)/(\beta-1)]^{1-\xi}}{[(\beta+1)/(\beta-1)]^{1-\xi} + 1} \tag{2.73}$$

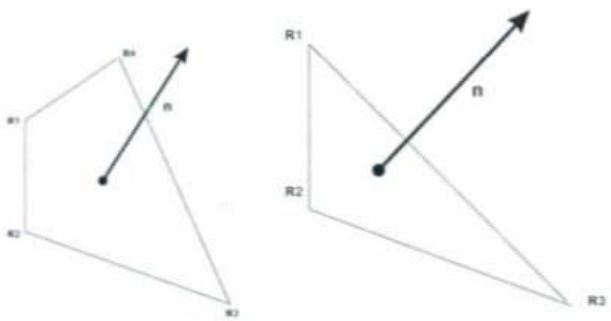

(a) Quadrilateral panel (b) Triangular panel

Figure 2-10: Quadrilateral and triangular panels

These points are then connected to generate panels. The order of the points (nodes) for a panel must be arranged in the counterclockwise direction as observed from the

flow field. This is important as it affects the directions of computed surface normal vectors, see Fig. 2-10. For a quadrilateral panel, two diagonal vectors are constructed from its four corner points.

$$\mathbf{D}_1 = \mathbf{R}_3 - \mathbf{R}_1$$

$$\mathbf{D}_2 = \mathbf{R}_4 - \mathbf{R}_2$$

The vector product of these diagonals produces a vector normal to the mean plane of the quadrilateral panel.

$$\mathbf{n} = \mathbf{D}_1 \times \mathbf{D}_2 / |\mathbf{D}_1 \times \mathbf{D}_2|$$

The modulus of the diagonal vector product also provides the area of the quadrilateral panel (projected onto the mean plane).

$$AREA = |\mathbf{D}_1 \times \mathbf{D}_2|/2$$

The centroid of each panel is obtained by

$$\mathbf{R}_C = \Sigma_{i=1}^{4} \mathbf{R}_i / 4$$

A similar method can also be applied to triangular panels.

Figure 2-11: Panel distributions on a sphere

Fig. 2-11 shows a sphere surface represented by panels. Quadrilateral panels are distributed on the sphere surface, and trilateral panels are distributed on its two polar points.

For a complex geometry, such as a lifeboat in Fig. 2-12 (a), the generation of panels is challenging with the panel generation method introduced above. In order to generate the panels accurately for a complex geometry, the meshing tools in ANSYS and Gridgen were employed. ANSYS can import geometry files from some computer aided design packages directly and generate the surface panels automatically. An example of generated surface panels on a lifeboat is presented in Fig. 2-12 (b).

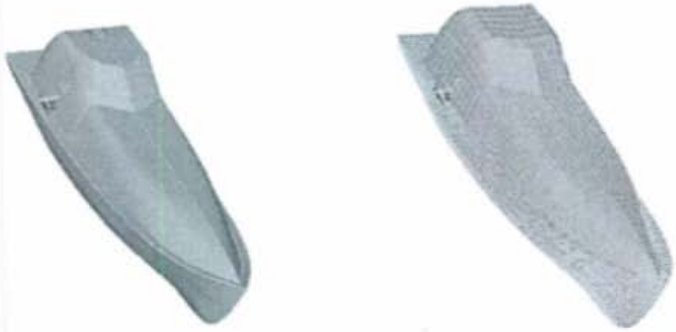

(a) Lifeboat model (b) Panel distribution

Figure 2-12: Panel distributions on a 3D lifeboat

2.5.2 Calculation of Density Function

Since the body is assumed to be rigid, the panels can be considered as moving with the solid body. For translational motions, the directions of normal vectors remain constant. The centroid of panels can be used to update the position of the body as follows:

$$x_{c_j} = x^*_{c_j} + u_c \Delta t$$

$$y_{c_j} = y^*_{c_j} + v_c \Delta t$$

$$z_{c_j} = z^*_{c_j} + w_c \Delta t$$

where $j = 1, 2, ..., N_j$, N_j is the total number of centroid, and u_c, v_c and w_c are the translational velocities of the mass center. These quantities, such as normal vectors and areas of panels are calculated at the beginning of the computation. For the rotational motions, the situation becomes somewhat more complicated. Rotating the body changes the orientations of normal vectors. Therefore, the nodes need to be used to update the body position.

$$x_{R_k} = x^*_{R_k} + u_{b_k} \Delta t$$

$$y_{R_k} = y^*_{R_k} + v_{b_k} \Delta t$$

$$z_{R_k} = z^*_{R_k} + w_{b_k} \Delta t$$

where $k = 1, 2, ..., N_k$, N_k is the total number of nodes, and u_{b_k}, v_{b_k} and w_{b_k} are the velocities of the nodes. The normal vectors need to be calculated in each time step.

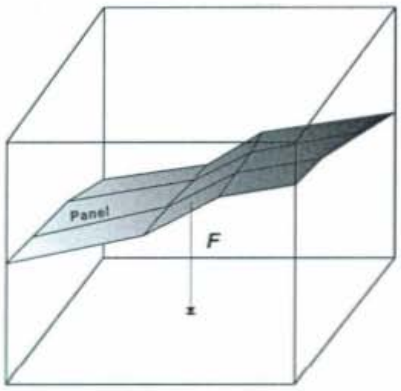

Figure 2-13: Calculation of the contribution factor

To calculate the volume fraction of a solid body in each Cartesian grid cell, the contribution of each panel to the computational grid needs to be estimated. The contribution of each panel is denoted by a contribution factor, ε, and it can be calculated by,

$$\varepsilon = \frac{1}{\Delta V_i} \int_{panel_i} F ds \tag{2.74}$$

where ΔV_i is the volume of the computational cell, and the function F is the distance from one point on the panel to the corresponding computational cell surface (reference surface). The reference surface can be determined by the slope of the panel. If the panel is more horizontal than vertical, the horizontal cell surface will be used as the reference surface (Fig. 2-13), otherwise the vertical cell surface is chosen as the reference surface. The computational cell is very small compared to the solid body (See Fig. 2-14). Therefore, the normals of panels in each computational cell can generally be seen in the same direction. However, the present algorithm will suffer some difficulties in capturing sharp corners, which will cause some numerical irregularities (See Section 3.2). Fig. 2-14 shows a wedge (transverse section) captured in two different grids. It can be seen that the grid resolution has great influences on

the geometry capturing.

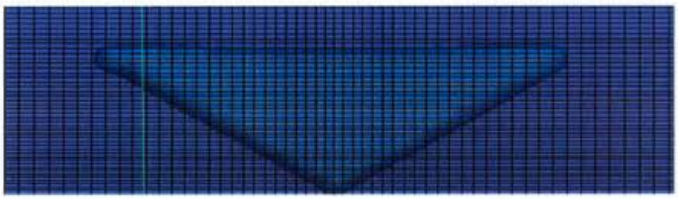

(a) Coarse grid

(b) Fine grid

Figure 2-14: Effect of grid refinement on the geometry capture: Top $80 \times 120 \times 120$, bottom $140 \times 200 \times 150$ grid cells

The density function for solid, ϕ_2, is then calculated by

$$\phi_2 = \sum_{i=1}^{i=N} \varepsilon_i \tag{2.75}$$

where N is the total panel number included in the computational cell.

The density function is used to denote the different phases in the computational domain occupied by liquid, solid and air, respectively. Fig. 2-15 shows that a sphere and a planing hull are embedded in a fixed computational domain. As shown, the upper part is air, the lower part is water, and the interface between air and water is the free surface.

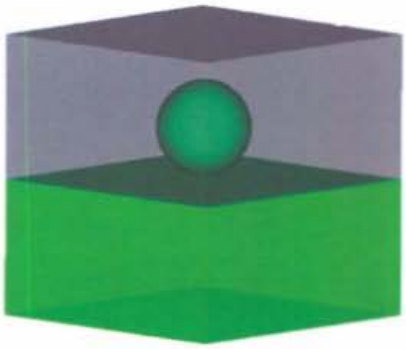

(a) Sphere

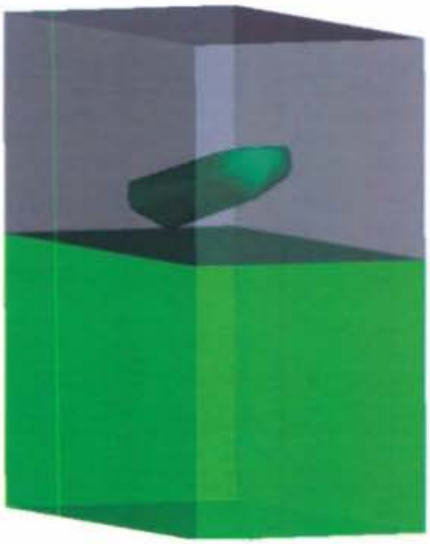

(b) Planing hull

Figure 2-15: 3D bodies embedded in fixed Cartesian grids

2.6 Coupled Motion of Rigid Body and Fluid

In order to solve the slamming problem with free motion, the coupled motion of a 3D body has to be simulated.

2.6.1 Motion of Rigid Body

The motion of an object can be described in terms of translations and rotations:

$$\mathbf{u}_c = (u_c, v_c, w_c)$$

$$\boldsymbol{\omega} = (\omega_x, \omega_y, \omega_z)$$

where $\mathbf{u}_c$ are the translational velocities of the center of mass, and $\boldsymbol{\omega}$ are the angular velocities. These velocities can be obtained by solving the following equations based on Newton's law of motion,

$$M_B \frac{d\mathbf{u}_c}{dt} = \mathbf{F} \tag{2.76}$$

$$\frac{d(\boldsymbol{\Pi}\boldsymbol{\omega})}{dt} = \boldsymbol{\Gamma} \tag{2.77}$$

where $\mathbf{F}$ are the total forces and $\boldsymbol{\Gamma}$ are the moments. These forces and moments can be calculated by the method introduced in Section 2.6.2.

$\boldsymbol{\Pi}$ is the matrix of moment of inertia.

$$\begin{pmatrix} \Pi_{xx} & \Pi_{xy} & \Pi_{xz} \\ \Pi_{yx} & \Pi_{yy} & \Pi_{yz} \\ \Pi_{zx} & \Pi_{zy} & \Pi_{zz} \end{pmatrix}$$

The elements of moment of inertia are calculated as follows:

$$\Pi_{xx} = \sum_{i,j,k}[(y_{i,j,k} - y_c)^2 + (z_{i,j,k} - z_c)^2]\Delta m_{i,j,k} \tag{2.78}$$

$$\Pi_{yy} = \sum_{i,j,k}[(z_{i,j,k} - z_c)^2 + (x_{i,j,k} - x_c)^2]\Delta m_{i,j,k} \tag{2.79}$$

$$\Pi_{zz} = \sum_{i,j,k}[(x_{i,j,k} - x_c)^2 + (y_{i,j,k} - y_c)^2]\Delta m_{i,j,k} \tag{2.80}$$

$$\Pi_{xy} = \Pi_{yx} = \sum_{i,j,k}[(x_{i,j,k} - x_c)(y_{i,j,k} - y_c)]\Delta m_{i,j,k} \tag{2.81}$$

$$\Pi_{xz} = \Pi_{zx} = \sum_{i,j,k}[(x_{i,j,k} - x_c)(z_{i,j,k} - z_c)]\Delta m_{i,j,k} \tag{2.82}$$

$$\Pi_{yz} = \Pi_{zy} = \sum_{i,j,k}[(y_{i,j,k} - y_c)(z_{i,j,k} - z_c)]\Delta m_{i,j,k} \tag{2.83}$$

where $\Delta m_{i,j,k} = \rho_{solid}\phi_{2_{i,j,k}}\Delta V_{i,j,k}$, is the mass of solid in a computational cell (i, j, k), and ρ_{solid} is the mass density of the solid body. Since the position of the body is known, the integration over the complete computational domain is not necessary, as only the cells with $\phi_2 > 0.0$ contribute to the computation.

Eq. 2.76 can be solved by the Euler method. Eq. 2.77, the equation of rotation, can be solved based on the work of Xiao (1999). Eq. 2.77 can be rewritten as follows:

$$\mathbf{\Pi}\frac{d\boldsymbol{\omega}}{dt} = \mathbf{\Gamma} - \boldsymbol{\omega}\frac{d\mathbf{\Pi}}{dt} \tag{2.84}$$

Applying Cramer's rule to Eq. 2.84, we can obtain,

$$\frac{d\omega_x}{dt} = \frac{\det \mathbf{\Lambda}_x}{\det \mathbf{\Pi}} \tag{2.85}$$

$$\frac{d\omega_y}{dt} = \frac{\det \mathbf{\Lambda}_y}{\det \mathbf{\Pi}} \tag{2.86}$$

$$\frac{d\omega_z}{dt} = \frac{\det \mathbf{\Lambda}_z}{\det \mathbf{\Pi}} \tag{2.87}$$

where

$$\mathbf{\Lambda}_x = \begin{pmatrix} \eta_x & \Pi_{xy} & \Pi_{xz} \\ \eta_y & \Pi_{yy} & \Pi_{yz} \\ \eta_z & \Pi_{zy} & \Pi_{zz} \end{pmatrix},$$

$$\mathbf{\Lambda}_y = \begin{pmatrix} \Pi_{xx} & \eta_x & \Pi_{xz} \\ \Pi_{yx} & \eta_y & \Pi_{yz} \\ \Pi_{zx} & \eta_z & \Pi_{zz} \end{pmatrix},$$

$$\mathbf{\Lambda}_z = \begin{pmatrix} \Pi_{xx} & \Pi_{xy} & \eta_x \\ \Pi_{yx} & \Pi_{yy} & \eta_y \\ \Pi_{zx} & \Pi_{zy} & \eta_z \end{pmatrix}$$

with

$$\eta_x = \Gamma_x - (\frac{d\Pi_{xx}}{dt}\omega_x + \frac{d\Pi_{xy}}{dt}\omega_y + \frac{d\Pi_{xz}}{dt}\omega_z) \tag{2.88}$$

$$\eta_y = \Gamma_y - (\frac{d\Pi_{xy}}{dt}\omega_x + \frac{d\Pi_{yy}}{dt}\omega_y + \frac{d\Pi_{yz}}{dt}\omega_z) \tag{2.89}$$

$$\eta_z = \Gamma_z - (\frac{d\Pi_{zx}}{dt}\omega_x + \frac{d\Pi_{zy}}{dt}\omega_y + \frac{d\Pi_{zz}}{dt}\omega_z) \tag{2.90}$$

and

$$\frac{d\Pi_{xx}}{dt} = \sum_{i,j,k}[2(y_{i,j,k} - y_c)(v_{i,j,k} - v_c) + 2(z_{i,j,k} - z_c)(w_{i,j,k} - w_c)]\Delta m_{i,j,k} \tag{2.91}$$

$$\frac{d\Pi_{yy}}{dt} = \sum_{i,j,k}[2(z_{i,j,k} - z_c)(w_{i,j,k} - w_c) + 2(x_{i,j,k} - x_c)(u_{i,j,k} - u_c)]\Delta m_{i,j,k} \tag{2.92}$$

$$\frac{d\Pi_{zz}}{dt} = \sum_{i,j,k}[2(x_{i,j,k} - x_c)(u_{i,j,k} - u_c) + 2(y_{i,j,k} - y_c)(u_{i,j,k} - u_c)]\Delta m_{i,j,k} \tag{2.93}$$

$$\frac{d\Pi_{xy}}{dt} = \frac{d\Pi_{yx}}{dt} = -\sum_{i,j,k}[(x_{i,j,k} - y_c)(v_{i,j,k} - v_c) + (y_{i,j,k} - y_c)(u_{i,j,k} - u_c)]\Delta m_{i,j,k} \tag{2.94}$$

$$\frac{d\Pi_{xz}}{dt} = \frac{d\Pi_{zx}}{dt} = -\sum_{i,j,k}[(x_{i,j,k} - y_c)(w_{i,j,k} - w_c) + (z_{i,j,k} - z_c)(u_{i,j,k} - u_c)]\Delta m_{i,j,k} \tag{2.95}$$

$$\frac{d\Pi_{yz}}{dt} = \frac{d\Pi_{zy}}{dt} = -\sum_{i,j,k}[(y_{i,j,k} - y_c)(w_{i,j,k} - w_c) + (z_{i,j,k} - z_c)(v_{i,j,k} - v_c)]\Delta m_{i,j,k} \quad (2.96)$$

The rotational velocities can then be obtained by the Euler explicit method as follows:

$$\omega_x = \omega_x^* + \Delta t \frac{\det \mathbf{\Lambda}_x}{\det \mathbf{\Pi}} \quad (2.97)$$

$$\omega_y = \omega_y^* + \Delta t \frac{\det \mathbf{\Lambda}_y}{\det \mathbf{\Pi}} \quad (2.98)$$

$$\omega_z = \omega_z^* + \Delta t \frac{\det \mathbf{\Lambda}_z}{\det \mathbf{\Pi}} \quad (2.99)$$

Once the translational and rotational velocities are determined, the total velocities of any points on the moving rigid body, u_i^b, can be obtained. The body motion provides boundary conditions for the Navier-Stokes equations. The resulting body motion are fed into the pressure equation of Eq. 2.18 by a no-slip fluid velocity boundary condition:

$$u_i^{**} = u_i^b \phi_2 + u_i^{**}(1 - \phi_2) \quad (2.100)$$

where u_i^{**} is the velocity after the non-advection phase I. This is for velocity interpolation in the boundary cells based on the volume fraction. However, the location of the interface is determined based on the volume fraction information (Density function). So, it is difficult to apply the no-slip boundary condition at the exact location of the boundary, unavoidably resulting in a loss of accuracy.

2.6.2 Calculation of Hydrodynamic Forces

The hydrodynamic force acting on the solid body, F_i, can be calculated by integrating the pressure and skin friction over the body surface. Note that for the slamming problem, the skin friction is relatively small and is neglected in the computation, therefore,

$$F_i = \oint_A (-p\delta_{ik}) n_k dA \tag{2.101}$$

where F_i represents the force due to the pressure, A denotes the surface of the solid body, and n_k is the kth component of the outward unit normal vector.

The forces can also be calculated by integrating over the whole computational domain (Hu and Kashiwagi, 2004). Applying Gauss's theorem to Eq. 2.101, leads to,

$$F_i = -\oint_\Omega \frac{\partial p}{\partial x_i} \phi_2 d\Omega \tag{2.102}$$

where Ω denotes the whole computational domain and ϕ_2 is the density function of solid.

The moments of force are computed as follows:

$$\Gamma_i = -\oint_\Omega \frac{\partial p}{\partial x_i} \times r_i \phi_2 d\Omega \tag{2.103}$$

where r_i is the distance vector from the computational cell to the center of mass. The advantage of Eqs. 2.102 and 2.103 is that the exact position and orientation of the boundary surface is not required.

Expanding Eqs. 2.102 and 2.103 with respect to the spatial coordinates leads to,

$$F_x = \sum_{i,j,k} (\frac{\partial p}{\partial x})_{i,j,k} \phi_{2_{i,j,k}} \Delta V_{i,j,k}$$
$$= \sum_{i,j,k} (\frac{p_{i+1,j,k} - p_{i-1,j,k}}{2\Delta x}) \phi_{2_{i,j,k}} \Delta V_{i,j,k} \tag{2.104}$$

$$F_y = \sum_{i,j,k} (\frac{\partial p}{\partial y})_{i,j,k} \phi_{2_{i,j,k}} \Delta V_{i,j,k}$$
$$= \sum_{i,j,k} (\frac{p_{i,j+1,k} - p_{i,j-1,k}}{2\Delta y}) \phi_{2_{i,j,k}} \Delta V_{i,j,k} \tag{2.105}$$

$$F_z = \sum_{i,j,k} (\frac{\partial p}{\partial z})_{i,j,k} \phi_{2_{i,j,k}} \Delta V_{i,j,k}$$
$$= \sum_{i,j,k} (\frac{p_{i,j,k+1} - p_{i,j,k-1}}{2\Delta z}) \phi_{2_{i,j,k}} \Delta V_{i,j,k} \tag{2.106}$$

$$\Gamma_x = \sum_{i,j,k} [(y_{i,j,k} - y_c)(\frac{\partial p}{\partial z})_{i,j,k} - (z_{i,j,k} - z_c)(\frac{\partial p}{\partial y})_{i,j,k}] \phi_{2_{i,j,k}} \Delta V_{i,j,k}$$
$$= \sum_{i,j,k} [(y_{i,j,k} - y_c)(\frac{p_{i,j,k+1} - p_{i,j,k-1}}{2\Delta z}) - (z_{i,j,k} - z_c)(\frac{p_{i,j+1,k} - p_{i,j-1,k}}{2\Delta y})] \phi_{2_{i,j,k}} \Delta V_{i,j,k} \tag{2.107}$$

$$\Gamma_y = \sum_{i,j,k}[(z_{i,j,k} - z_c)(\frac{\partial p}{\partial x})_{i,j,k} - (x_{i,j,k} - x_c)(\frac{\partial p}{\partial z})_{i,j,k}]\phi_{2_{i,j,k}}\Delta V_{i,j,k}$$
$$= \sum_{i,j,k}[(z_{i,j,k} - z_c)(\frac{p_{i+1,j,k} - p_{i-1,j,k}}{2\Delta x}) - (x_{i,j,k} - x_c)(\frac{p_{i,j,k+1} - p_{i,j,k-1}}{2\Delta z})]\phi_{2_{i,j,k}}\Delta V_{i,j,k} \tag{2.108}$$

$$\Gamma_z = \sum_{i,j,k}[(x_{i,j,k} - x_c)(\frac{\partial p}{\partial y})_{i,j,k} - (y_{i,j,k} - y_c)(\frac{\partial p}{\partial x})_{i,j,k}]\phi_{2_{i,j,k}}\Delta V_{i,j,k}$$
$$= \sum_{i,j,k}[(x_{i,j,k} - x_c)(\frac{p_{i,j+1,k} - p_{i,j-1,k}}{2\Delta y}) - (y_{i,j,k} - y_c)(\frac{p_{i+1,j,k} - p_{i-1,j,k}}{2\Delta x})]\phi_{2_{i,j,k}}\Delta V_{i,j,k} \tag{2.109}$$

where x_c, y_c and z_c are the coordinates of the center of mass, and $\Delta V_{i,j,k}$ is volume of the computational cell.

2.7 Summary of the Computational Method

The computational procedure can be summarized as follows:

1. Solve the advection equations.
    - The advection equations of Eqs. 2.5 and 2.6 for velocities and pressure, and advection equation of Eq. 2.38 for free surface, are solved by the CIP method.
    - The free surface is updated by solving Eq. 2.38 and the density function ϕ_1 is obtained by Eq. 2.39.

- In the free-fall case, the motion equations of Eqs. 2.76 to 2.77 are solved. Otherwise, a prescribed velocity is used as input to update the solid body. The density function of ϕ_2 is obtained by the panel-based numerical method. The density function of air, ϕ_3, is obtained by Eq. 2.33. During the simulation, the values of ϕ_1 and ϕ_3 change continuously between the values for air and water at the free surface. The same happens with the density functions between the body, the air and the water.
- The physical properties, such as viscosity and density, are calculated for each computational cell by Eqs. 2.34 and 2.35 based on the incompressible flow assumption.

2. Solve the non-advection equations I (Eq. 2.7).
   - An Euler explicit scheme is used for the time integration for the left-hand-side terms of Eqs. 2.11 to 2.13 and a central finite difference scheme is used to discretise the terms on the right-hand-side of these equations. Note that for the intermediate velocity field u_i^{**}, continuity is not required.

3. Solve the non-advection equations II.
   - Based on a pressure-based algorithm, a poisson equation of pressure (Eq. 2.18) is obtained. The calculation of Eq. 2.18 is generally the most computationally time-consuming part in the numerical simulation. A CG iterative method is employed to solve the linear equations. Note that the no-slip boundary condition (Eq. 2.100) is used before solving Eq. 2.18 to enforce the velocity inside the body equal to the rigid body velocity.
   - The velocities in the new time step are obtained by solving Eqs. 2.30 to 2.32. The spatial derivatives of advection equations are calculated by Eqs.

2.69, 2.70 and 2.71. The slamming loads are calculated by Eqs. 2.104 to 2.109.

4. Repeat steps (1)-(3) until the prescribed final time is reached.

A flow chart of the computational procedure is given in Fig. 2-16

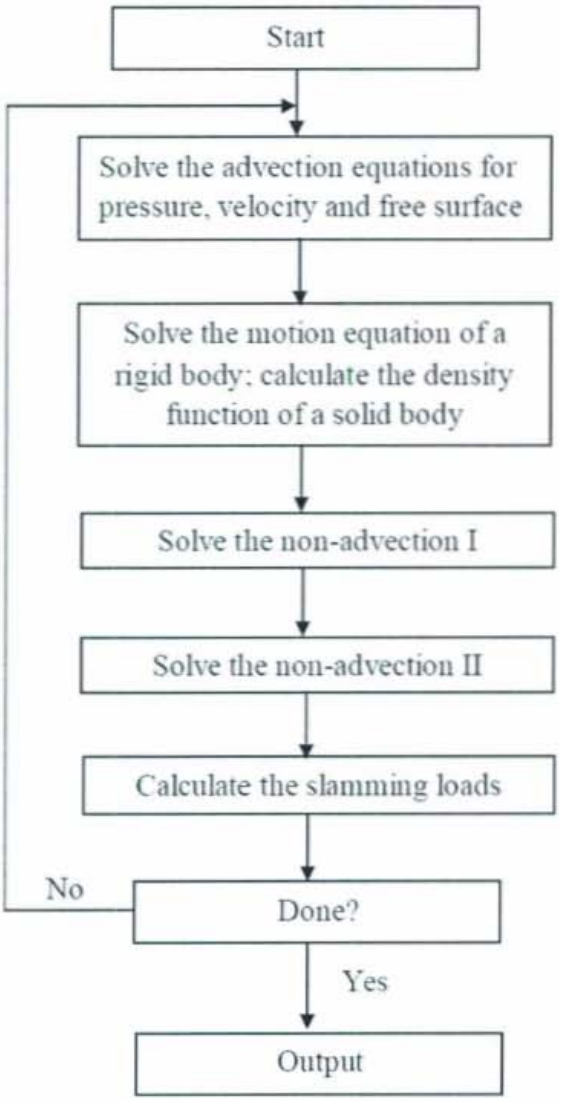

Figure 2-16: Procedure of the numerical method

Chapter 3

Water Entry of 3D Bodies with Prescribed Velocities

This chapter presents some numerical solutions of 3D bodies entering calm water with prescribed vertical and oblique velocities. The hydrodynamic forces and pressure distributions were computed and compared with experimental results. The highly nonlinear free surface elevations were captured. Three-dimensional flow effects were investigated.

In the computations, the liquid phase was treated as water and the gas phase was treated as air. Their density and viscosity at 25 ^oC were chosen as ρ_{water}=997 kgm^{-3}, $\mu_{water} = 8.55 \times 10^{-4}\ kgs^{-1}m^{-1}$, and $\rho_{air} = 1.16\ kgm^{-3}$, $\mu_{air} = 1.85 \times 10^{-5}\ kgs^{-1}m^{-1}$, respectively.

3.1 Verification

The present numerical method has been verified for a sphere added mass. When a submerged body is accelerating in infinite fluid, it experiences a reaction force from the fluid.

$$F_r = m_a \frac{\partial u_b}{\partial t} \tag{3.1}$$

The value of m_a is called the added mass and is dependent on the shape of the submerged body. The computed added mass was compared with the analytical solution. Note that the added mass of a sphere submerged in infinite flow is $\frac{2}{3}\rho\pi R^3$ based on the potential flow theory. In the applications in this study, viscous effects play a minor role at the start of the simulation, and there is not yet a viscous wake behind the sphere, thus the flow behavior is very much comparable with a potential flow. Therefore the added mass as they are computed by the reaction force and acceleration of the body according to Eq. 3.1 can be compared with the analytical solution.

In present simulation, the sphere was accelerated at 1 m/s^2. The radius of the sphere was 0.1 m, and the computational domain was 0.6 m × 0.5 m × 0.5 m. Theoretically, the added mass m_a=2.09 kg. The added mass as computed by the present method is shown in Fig. 3-1. As shown, the computed added mass agree well with the analytical solution.

Simulations have been carried out with three different grids and time steps. It can be observed that the numerical solution converges as the grid refinement increases and the time step decreases.

The relative error (RE) was calculated to estimate the differences between numerical

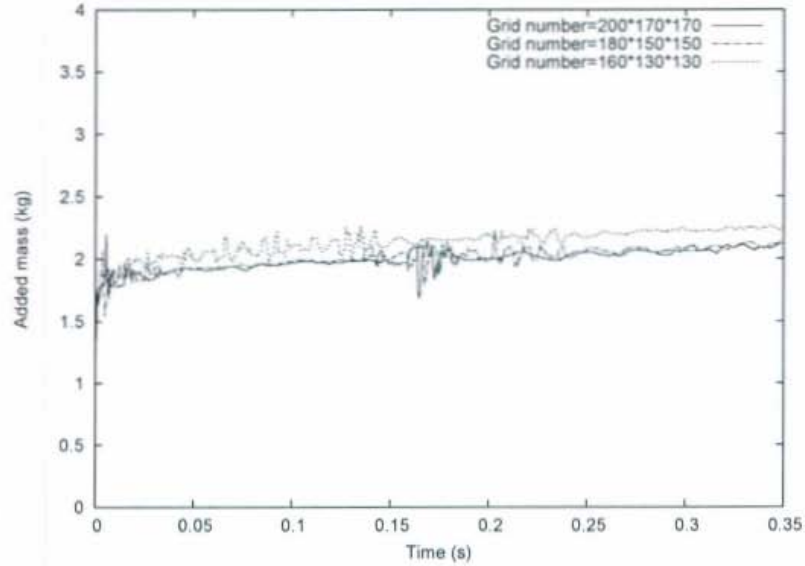

(a) Sensitivity to the grid resolution

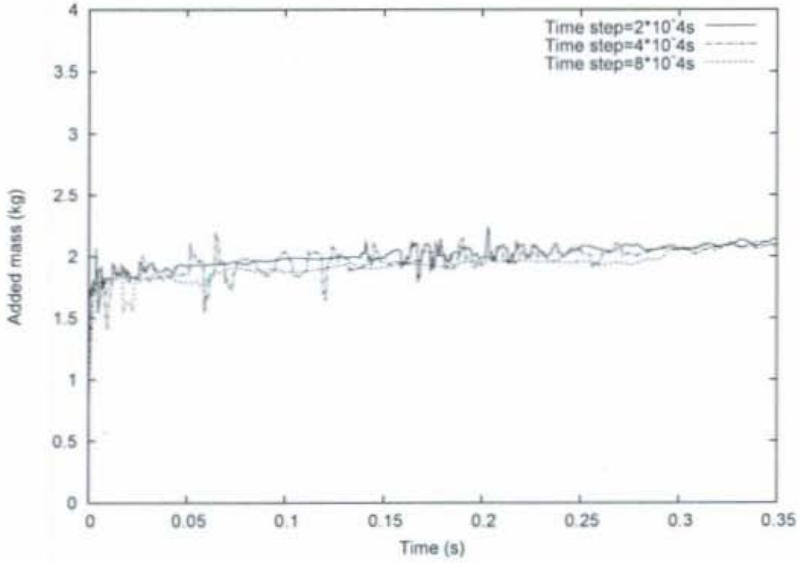

(b) Sensitivity to the time step

Figure 3-1: Computed added mass for a sphere

solution predicted by the CIP method and analytical results. The relative error is defined as follows:

$$\delta = \left| \frac{\hat{s} - s_e}{s_e} \right| \times 100\% \tag{3.2}$$

where $\hat{s}$ is the numerical solution and the s_e is the analytical solution. The average value of the added mass between 0.1 s to 0.35 s is $\hat{s} = 2.03$ corresponding to the solution with the finest grid. The RE for the numerical solution by the CIP method based on Eq. 3.2 is 2.87%. In this case, verification is successful from a programmatic standpoint.

3.2 Water Entry of a 3D Wedge

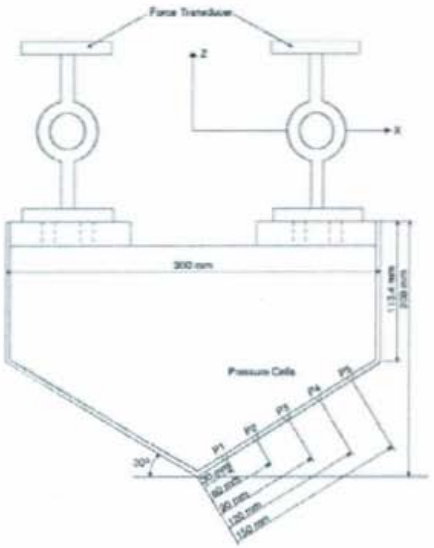

Figure 3-2: A wedge used in drop test

Table 3.1: Data related to the experimental drop test of a wedge

Breadth of section	0.50 m
Vertical distance from keel to knuckles	0.29 m
Length of measuring sections	0.20 m
Length of each dummy sections	0.40 m
Total length of the wedge	1 m
Weight drop rig (without ballast)	141 kg
Ballast weight	100 kg
Total weight of drop rig	241 kg
Weight of the measure section	14.5 kg

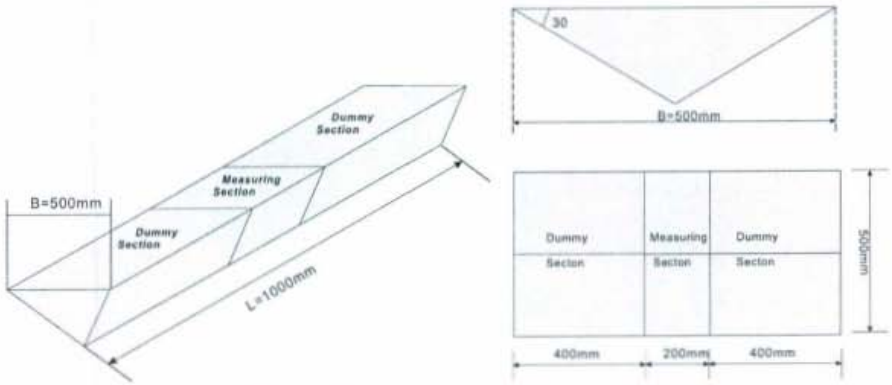

Figure 3-3: Geometry of a 3D wedge

The geometry of the wedge used in the drop test is given in Fig. 3-2. Zhao et al. (1996) conducted the drop test for such a wedge at MARINTEK. The test rig consisted of four different parts: the vertical guide rails, the trolley, a horizontal beam and the test section. The beam was connected to the trolley using one bolt at each end of the beam. The ballast weights were located within the beam. The trolley was engaged with the vertical guide rail. The test sections were mounted directly to the horizontal beam. The test sections were connected to the trolley during the entire drop. The free-falling rig was mounted in a small towing tank. The trolley was raised using a winch fitted with a quick-release hook. The hook was connected to an automatic release mechanism. After the test section had hit the water surface,

the trolley was stopped using two elastic ropes. The total drop section was divided into three parts (See Fig. 3-3), one measuring section, and two dummy sections. The breadth, B, of the test section is 0.5 m, the total length, L, is 1 m, and the measure part length is 0.2 m. The maximum drop height was about 2 m. Pressures in 5 locations were measured using pressure cells. The positions of the pressure cells are shown in Fig. 3-2.

Figure 3-4: Computational model

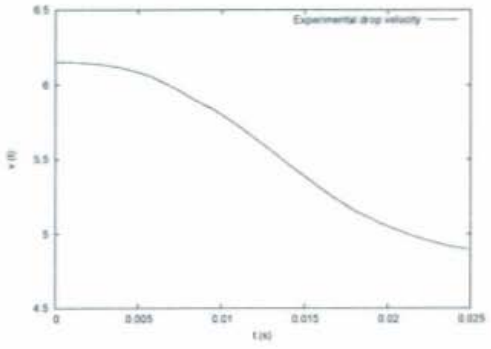

Figure 3-5: Experimental drop velocity

The computational model of 3D wedge is shown in Fig. 3-4. In the computation, the solid surface was represented by 198 triangular panels and 19,157 rectangular panels. The computational domain size was 1.15 m × 1.73 m × 1.15 m.

To investigate the convergence of the numerical solution to the time step and the grid resolution, the hydrodynamic forces on the wedge were computed using various

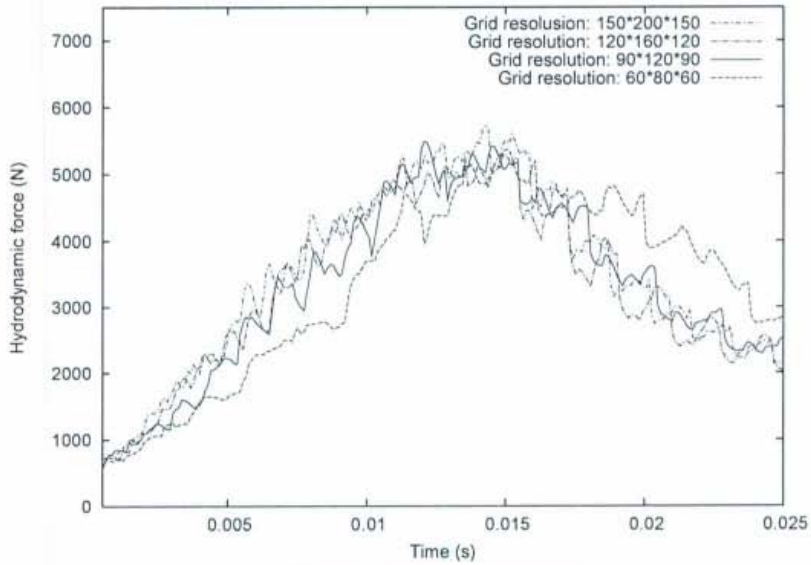

(a) Sensitivity to the grid resolution

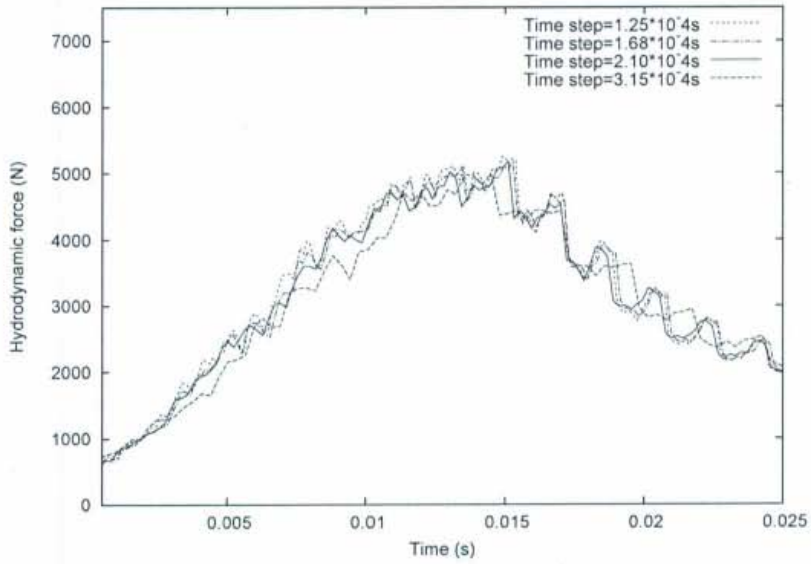

(b) Sensitivity to the time step

Figure 3-6: Sensitivity studies

time steps and numbers of grid. The sensitivity of the computed forces to the grid refinement at time step Δt=1.05×10^{-4} s is given in Fig. 3-6(a). The convergence of the numerical solution on a grid of 150 × 200 × 150 to the time step is presented in Fig. 3-6(b). It can be observed that the numerical solution converges as the grid refinement increases and the time step decreases.

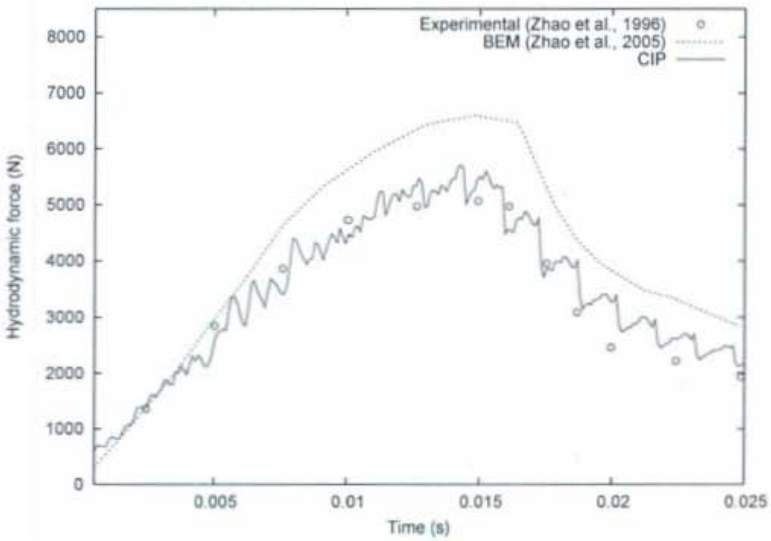

Figure 3-7: Vertical slamming force

The time series of the computed hydrodynamic forces were compared with the experimental results and boundary element method (Zhao et al., 1996) in Fig. 3-7. The computational grid was 150 × 120 × 150 and the time step was chosen as 1.05 × 10^{-4} s. The experimental vertical velocity (See Fig. 3-5) was used as input to the numerical simulation. As shown in this figure, the numerical solution by the CIP method is in good agreement with experimental result. The numerical solution by 2D BEM over-predicts the slamming force. Note that fluctuations are observed in the predicted slamming forces. They are mainly due to numerical irregularities. Similar fluctuations in the simulations are also shown in the work of Fekken (2004). When bodies, especially for those with sharp corners, are moving through the computational

grid, the geometry, especially the corner geometry, can not be accurately captured by the density function in present method. The application of the no-slip condition on the body boundary is based on the density function (The boundary condition can not be applied at the exact location of the boundary). This leads to the fluctuations in the pressure computation and therefore in the slamming forces.

The root mean square error (RMSE) was calculated to estimate the differences between numerical solution predicted by the CIP method and experimental results. The root mean square error is defined as follows:

$$\bar{\delta} = \sqrt{\frac{1}{n}\sum_{i=1}^{n}\delta_i^2} \times 100\% \tag{3.3}$$

and

$$\delta_i = \frac{s_i^n - s_i^e}{s_i^e} \tag{3.4}$$

where s_i^n and s_i^e are the numerical result and experimental result on time point i, respectively.

The root mean square error of the computed slamming force by the CIP method relative to experimental results is 12.56% (See Table 3.2). The present numerical method give a good prediction on the slamming force.

To investigate the effect of 3D flow, the hydrodynamic forces were computed using various lengths of dummy sections. In the computation, the lengths of dummy sections were changed and the measuring section was kept constant. The slamming force was obtained by integrating the pressure along the measuring section. As shown in Fig. 3-8, the computed maximum slamming forces become smaller as the lengths of

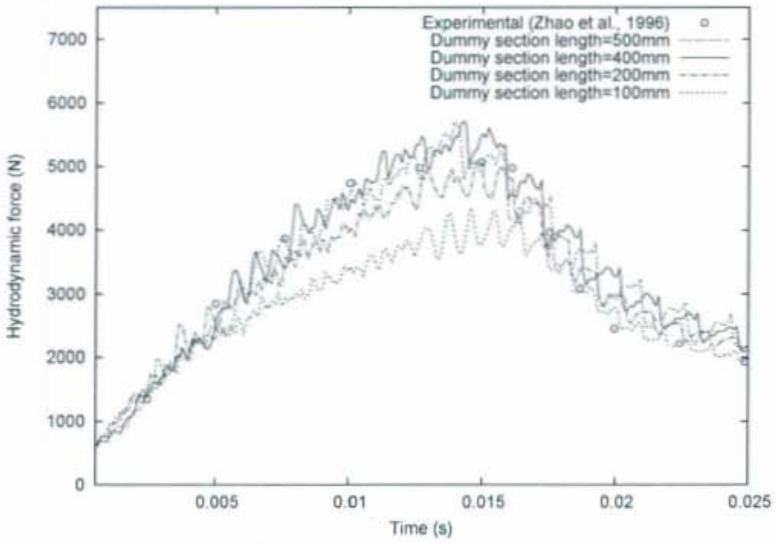

Figure 3-8: 3D flow effects

dummy sections decrease, and the 3D flow effects become significant. The 3D effects cause a reduction in the vertical slamming force. The maximum slamming force has no changes when the dummy section length is increased.

Fig. 3-9(a) presents the hydrodynamic pressure distribution on the mid wedge section at the time instant (t=0.013 s) in the computation. It can be shown from the figures that the maximum pressure occurs near the spray roots of the jets. Fig. 3-9(b) shows the pressure distribution on the central plane of the 3D wedge. As shown in Fig. 3-9(b), the pressure at measuring section keeps uniform whereas the pressure at dummy section is significantly smaller than that at measuring section. (It can be seen that the dummy sections reduce the 3D flow effects on the measuring section)

Fig. 3-10 represents the numerical and experimental pressures on these five test points for three time instants. The non-dimensional pressure coefficient is defined as $C_p = \frac{p}{0.5*\rho V(t)^2}$ where p is the hydrodynamic pressure, ρ is the density of water, $V(t)$ is the drop velocity. The numerical results by the present method are generally in

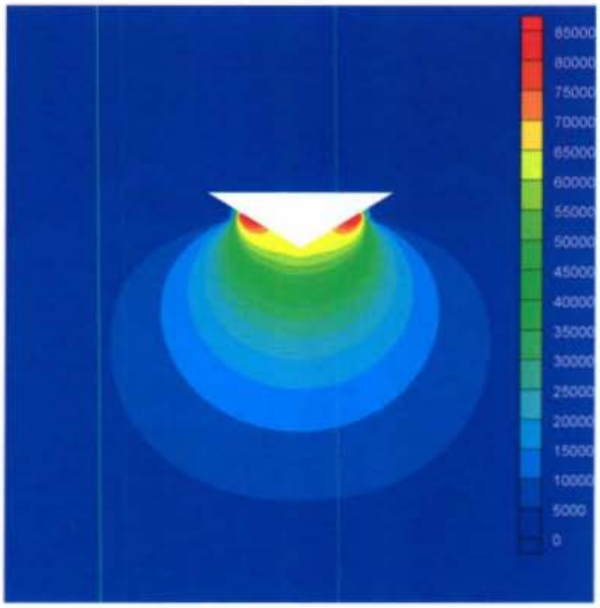

(a) Mid transverse section

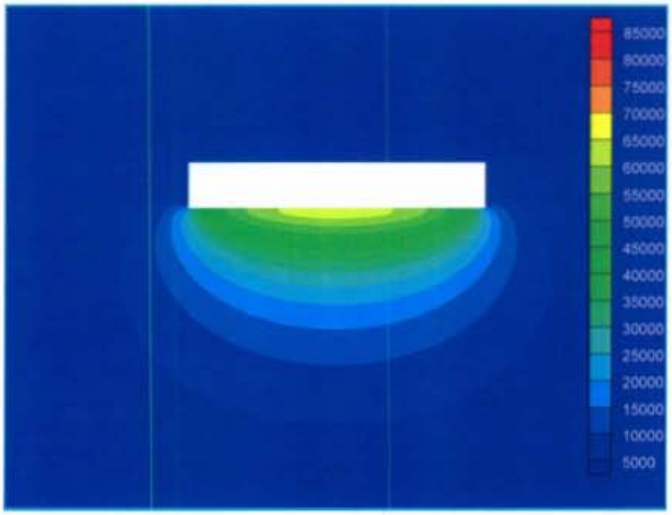

(b) Central plane

Figure 3-9: Hydrodynamic pressure (Pa) distribution on sections of a 3D wedge

agreement with the experimental results. The reasons for the discrepancy at P_5 are believed to be the loss of interface sharpness and inaccurate boundary conditions on the body. In the present computation, the interface was not explicitly tracked but was reconstructed from the field variables on the fixed computational grid, unavoidably resulting in losing some accuracies when details of the interface can not be covered by grid.

Table 3.2: RMSE of the numerical solutions by the CIP method

Hydrodynamic force in Fig. 3-7:	12.56%
Pressure in Fig. 3-10 (a) (t=0.00435):	17.85%
Pressure in Fig. 3-10 (b) (t=0.0158):	23.88%
Pressure in Fig. 3-10 (c) (t=0.0202):	22.03%

Fig. 3-11 presents the free surface deformation during the water entry of the wedge at several time instants. After the wedge enters the free surface, jets are generated and run up. Waves propagate away from the impact center.

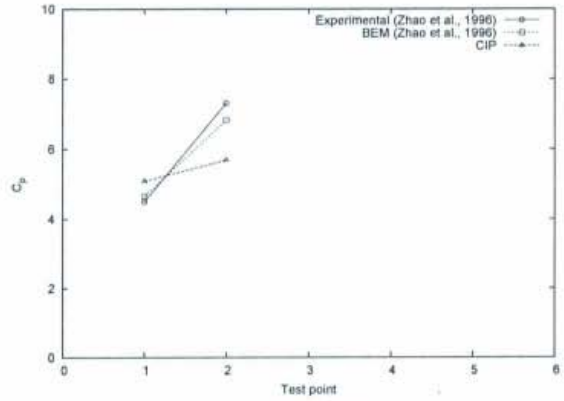

(a) t=0.00435 s

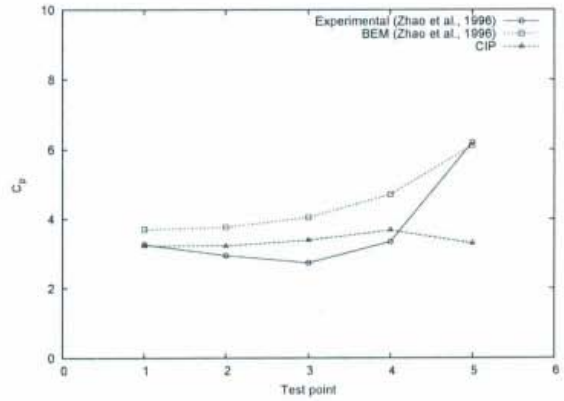

(b) t=0.0158 s

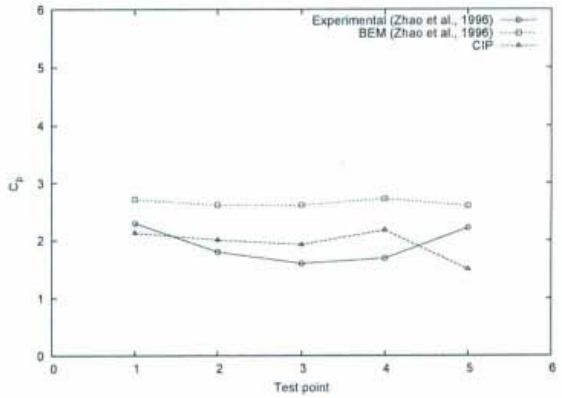

(c) t=0.0202 s

Figure 3-10: Pressure coefficients of test points

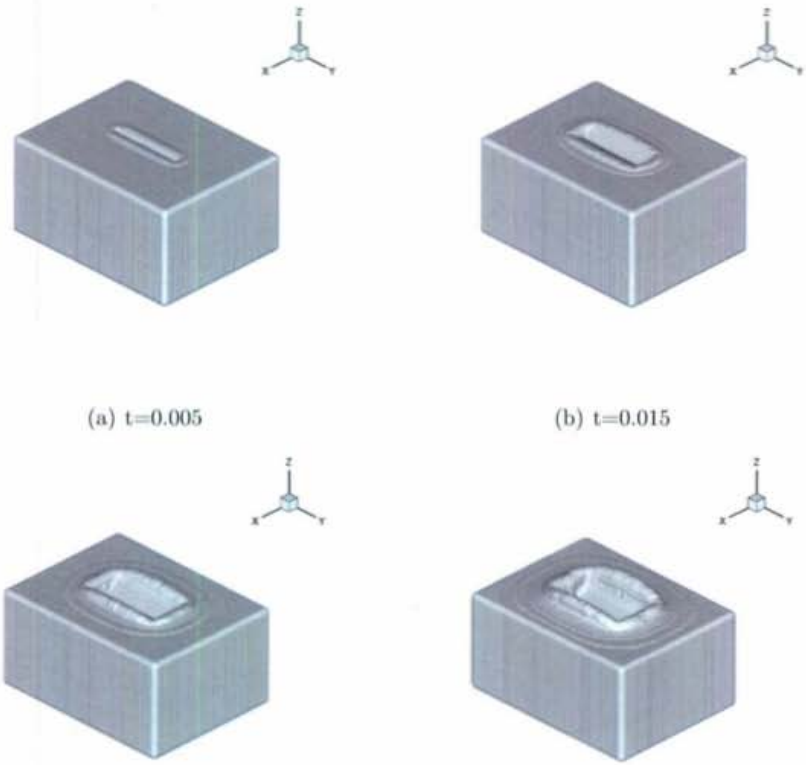

(a) t=0.005 (b) t=0.015

(c) t=0.025 (d) t=0.04

Figure 3-11: Free surface elevation during the water entry of a 3D wedge

3.3 Water Entry of a 3D Ship Section

Aarsnes (1996) conducted a drop test for a ship section, see Fig. 3-12(a). The breadth and draft of the section are 0.32 m and 0.24 m, respectively. It was attached via force transducers to a free-fall rig. Pressures were measured at positions P_1, P_2, P_3 and P_4 shown in Fig. 3-12(b). The ship section was represented by 18436 panels in the computation, see Fig. 3-13. The computational grid was 100 $\times$ 200 $\times$ 150 and the time step was chosen as 1.05 $\times 10^{-4}$ s. The computational domain size was 1.15 m $\times$ 1.73 m $\times$ 1.15 m. In present computation, the section was forced into the water with the velocity profile taken from the experiments (See Fig. 3-14).

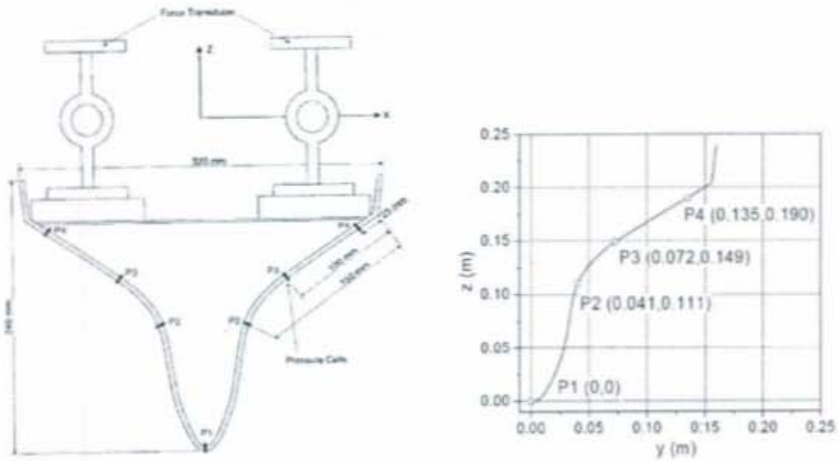

(a) (b)

Figure 3-12: Geometry of a 3D ship section in the drop test

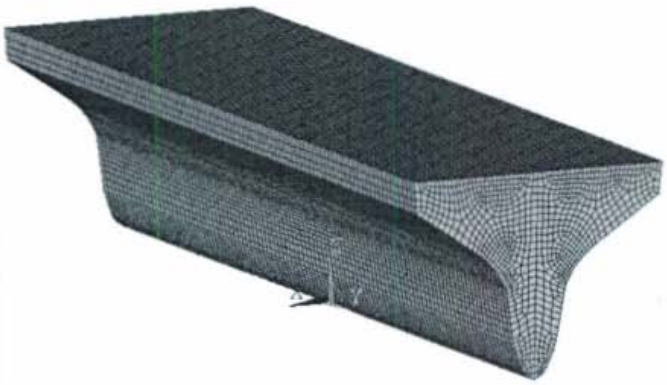

Figure 3-13: Computational model of a 3D ship section

Table 3.3: Data related to the experimental drop test of a ship section

Breadth of section	0.32 m
Vertical distance from keel to knuckles	0.203 m
Length of measuring sections	0.10 m
Length of each dummy sections	0.45 m
Total length	1 m
Weight drop rig (without ballast)	161 kg
Ballast weight	100 kg
Total weight of drop rig	261 kg
Weight of the measure section	6.9 kg

The time series of the computed hydrodynamic forces were compared with the experimental results in Fig. 3-15 and numerical results by Sun (2007). In the work of Sun (2007), the water entry problem was simulated by a 2D boundary element method (BEM). As shown in this figure, the numerical solution by the CIP method is in general agreement with experimental results. However, it under-predicts the peak values of slamming force. The numerical solutions by the BEM is slightly higher than the experimental results.

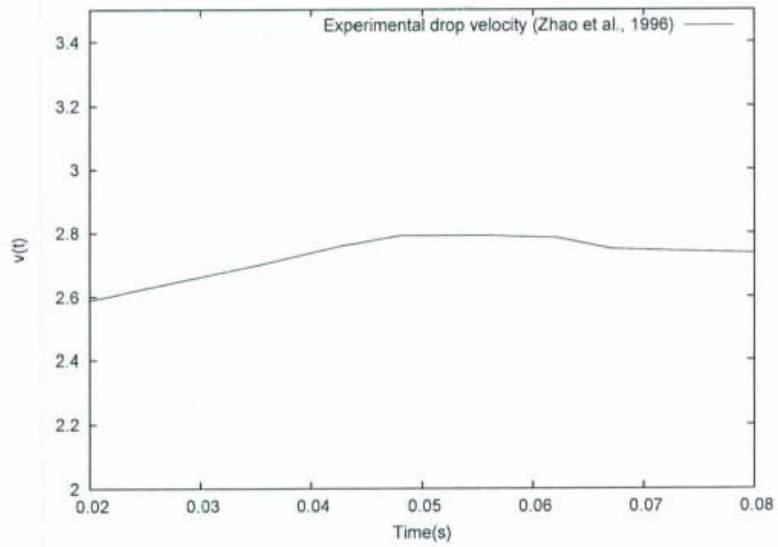

Figure 3-14: Experimental velocity

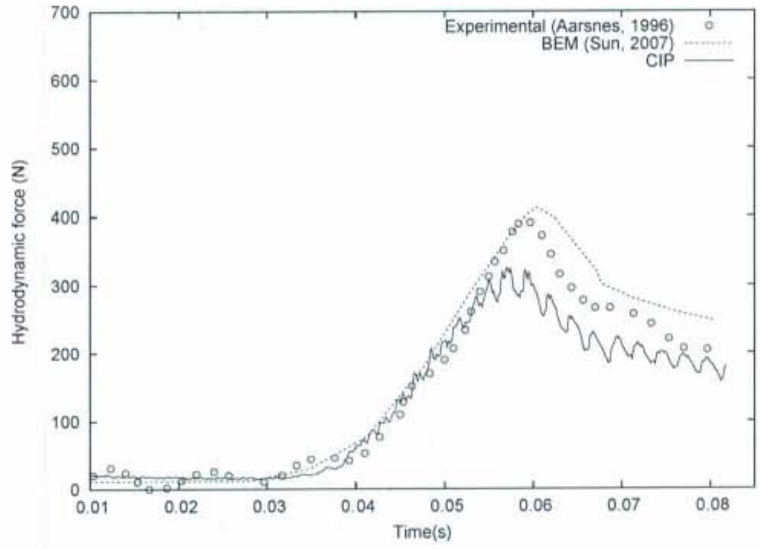

Figure 3-15: Vertical slamming force

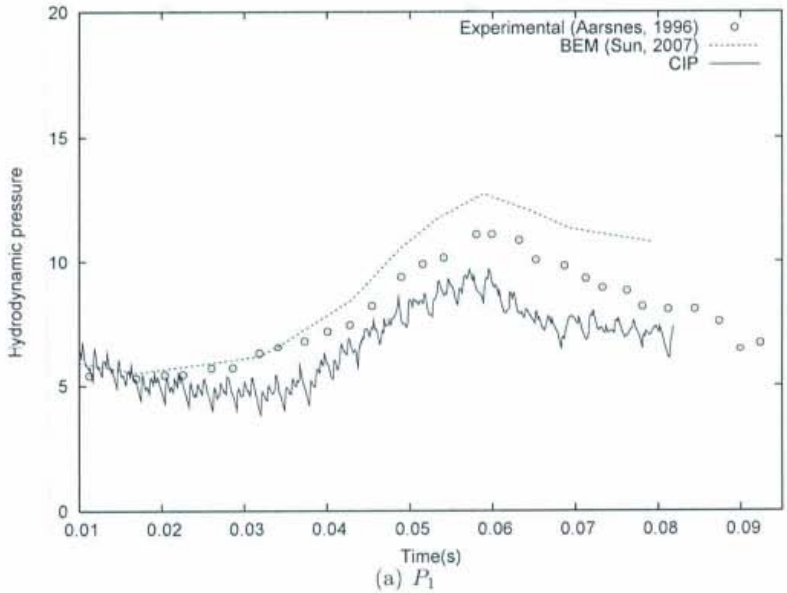
Experimental (Aarsnes, 1996)
BEM (Sun, 2007)
CIP
Hydrodynamic pressure
Time(s)
0
5
10
15
20
0.01
0.02
0.03
0.04
0.05
0.06
0.07
0.08
0.09

(a) P_1

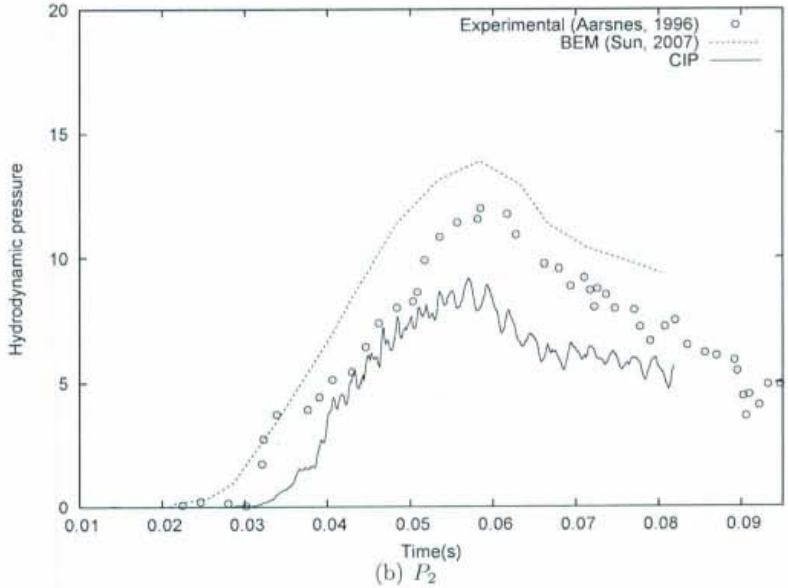
Experimental (Aarsnes, 1996)
BEM (Sun, 2007)
CIP
Hydrodynamic pressure
Time(s)
0
5
10
15
20
0.01
0.02
0.03
0.04
0.05
0.06
0.07
0.08
0.09

(b) P_2

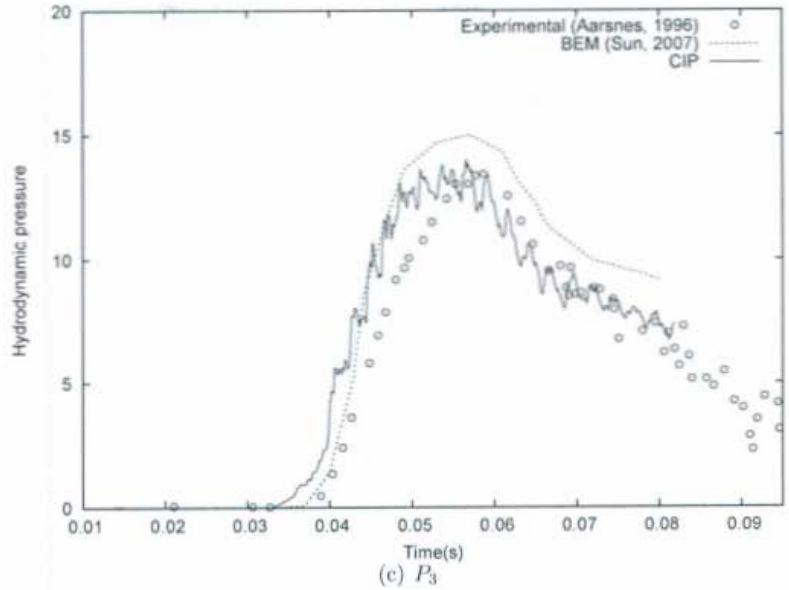

(c) P_3

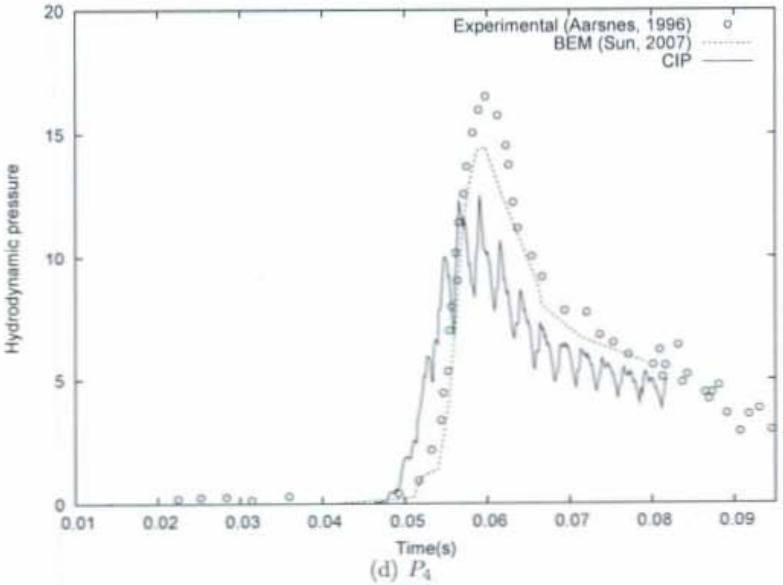

(d) P_4

Figure 3-16: Numerical and experimental hydrodynamic pressures (KPa) for the ship section entering calm water

The computed hydrodynamic pressures were presented in Fig. 3-16 and compared with experimental results (Aarsnes, 1996) and numerical solution by 2D BEM (Sun, 2007). The CIP method slightly under-predicts the pressure at points P_1, and it agrees well with the experimental data at point P_3. However, the pressures at P_2 and P_4 are under-predicted by as much as twenty percent of the peak values. Similar to the case of a 3D wedge, these discrepancies are presumedly due to the loss of interface sharpness and therefore inaccurate body boundary conditions caused by the immersed boundary method. In addition, as shown in Fig. 3-17, the spray jets near the knuckles were not captured very well. The loss of spray jets may also contribute to the discrepancies. The numerical results by the 2D BEM slightly over-predict the pressures at points P_1, P_2 and P_3, and it under-predicts the pressure at P_4. As shown in these figures, the peak pressures at four positions almost occur at the same time (t=0.058 s).

The root mean square errors of the numerical solutions predicted by the CIP method relative to experimental results were given in Table 3.4.

Table 3.4: RMSE of the numerical solutions by the CIP method

Hydrodynamic force in Fig. 3-15:	21.91%
Pressure on P_1 in Fig. 3-16 (a):	19.82%
Pressure on P_2 in Fig. 3-16 (b):	27.8%
Pressure on P_3 in Fig. 3-16 (c):	20.45%
Pressure on P_4 in Fig. 3-16 (d):	26.5%

Fig. 3-17 shows the free surface elevation at the time instant of t=0.058 s. As we can see, the simulated jets are very 'blunt'. This can be attributed to grid resolution effects. A further comparison and discussion about the jet simulation will be given in section 4.1.

(a)

(b)

Figure 3-17: Free surface simulation at t=0.058s

3.4 Water Entry of a Flared Body

The computation was conducted to a 3D flared body, as shown in Fig. 3-18. The vertical water entry of the flared body was studied in the experiment by Troesch and Kang (1986). The flared body had a total weight of 74.7 N and floated at

approximately 90 percent of the total height of the body. Table 3.5 gives the offsets of the flared body.

Table 3.5: Offset table of the flared body

Radius (in)	Height (in)	Radius (in)	Height (in)
0.0000	0.0000	2.9023	5.9070
0.3849	0.0285	3.1071	6.3008
0.7550	0.1186	3.3434	6.6946
1.0961	0.2950	3.5836	7.0884
1.3951	0.5141	3.8632	7.4822
1.6404	0.7969	4.1546	7.8760
1.8228	1.1505	4.4854	8.2698
1.9350	1.4614	4.8733	8.6636
1.9729	1.5752	5.2691	9.0574
2.0084	1.9690	5.7219	9.4512
2.0360	2.3628	6.1866	9.8450
2.0576	2.7566	6.6119	10.2389
2.0970	3.1504	6.9309	10.6327
2.1659	3.5442	7.2223	11.0265
2.2447	3.9380	7.4784	11.4202
2.3392	4.3318	7.6752	11.8141
2.4534	4.7256	7.7854	12.4692
2.5973	5.1194	7.7933	12.7251
2.7290	5.5132		

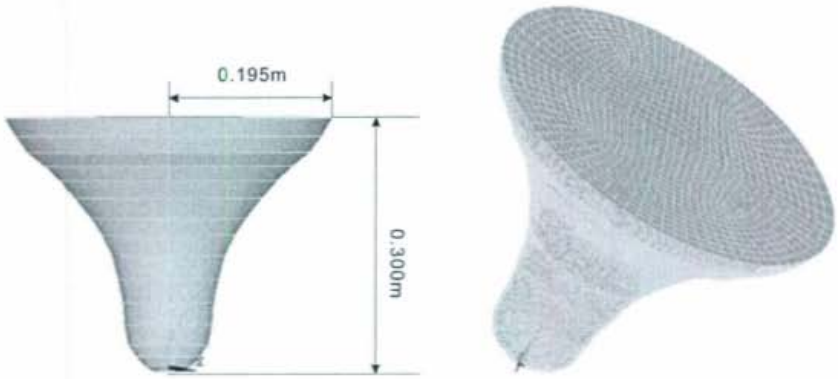

Figure 3-18: Geometry of a flared body

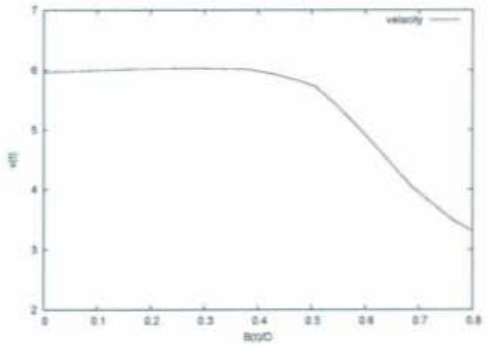

Figure 3-19: Velocity of flared body in the computation

The non-dimensional slamming coefficient is defined as $C_s = \frac{F_I}{0.5 * \rho V_0^2 A_p}$ where F_I is the impact force, ρ is the density of water, V_0 is the initial vertical impact velocity (5.99 m/s), and A_p is the projected area of the flared body.

In Fig. 3-20, the computed vertical slamming force coefficients were compared with experimental results and numerical solutions with the potential flow theory by Troesch and Kang (1986). The vertical velocity used in the present computation is shown in Fig. 3-19. In Fig. 3-20, $B(t)$ is the instantaneous submerged depth and D is the top transverse dimension ($2 \times 0.195\ m$). In the computation, the computational grid was

$180 \times 180 \times 140$ and the time step was chosen as 4.11×10^{-5} s. The computational domain size was 1.2 $m \times 1.2$ $m \times 1.0$ m. As shown, the computed results by the CIP method agree well with the experimental results. The root mean square error of the numerical solution predicted by the CIP method relative to experimental result is 17.03%. However, the reason for the over-prediction of the maximum vertical impact force by the potential flow is unclear. Troesch and Kang (1986) stated that it could be caused by the spray jet jumping on the flared upper sections which leads to a lower experimental velocity than the one predicted by the potential flow theory. Also, as indicated by Maskew et al. (1994), possible inaccurate force prediction in the work of Troesch and Kang (1986) could be due to the simplified free surface conditions or model discretization which can not be identified with certainty.

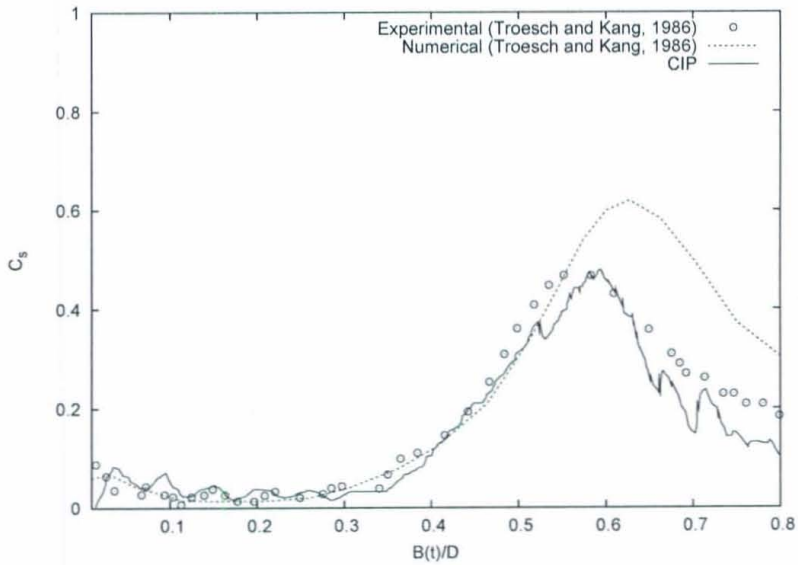

Figure 3-20: Time history of the slamming forces on a flared body

3.5 Water Entry of a Sphere

The model tests of water entry of a sphere subjected to oblique impact angles were carried out by Troesch and Kang (1986) for a sphere entering calm water with both vertical and horizontal velocities. The diameter of the sphere is 0.502 m. The sphere was ballasted to float as a hemisphere. The sphere was dropped from a moving carriage with a speed corresponding to the vertical impact velocity, which resulted in an oblique entry angle of 45 degrees. Computations are carried out for two drop heights, 0.61 m and 1.22 m, which corresponds to impact velocities of 3.46 m/s (Fn=2.2030) and 4.89 m/s (Fn=3.1156). The surface of the sphere was represented by 200 triangular panels and 19,800 rectangular panels in the computation. The computational grid was 210 $\times$ 180 $\times$ 180 and the time step was chosen as 1.027 $\times$ 10^{-4} s. The computational domain size was 1.75 m $\times$ 1.5 m $\times$ 1.5 m.

The non-dimensional slamming coefficient is defined as $C_s = \frac{F_I}{0.5*\rho V_0^2 A_p}$ where F_I is the impact force, ρ is the density of water, V_0 is the initial vertical impact velocity, and A_p is the projected area of the sphere.

The computed horizontal and vertical slamming force coefficients are compared with experimental results and numerical solutions based on potential flow theory (Troesch and Kang, 1986) in Figs. 3-21 and 3-22. The velocity used in the present computation is shown in Fig. 3-24. In these figures, $B(t)$ is the instantaneous submerged depth and R is the radius of sphere. As shown in these figures, the numerical solution by the CIP method in general agrees well with experimental results. The root mean square errors of the numerical solutions predicted by the CIP method relative to experimental results were given in Table 3.6.

Figs. 3-23 presents the free surface deformation during the water entry of the sphere at several time instants. After the sphere enters the free surface, jets are generated around the spheres and run up.

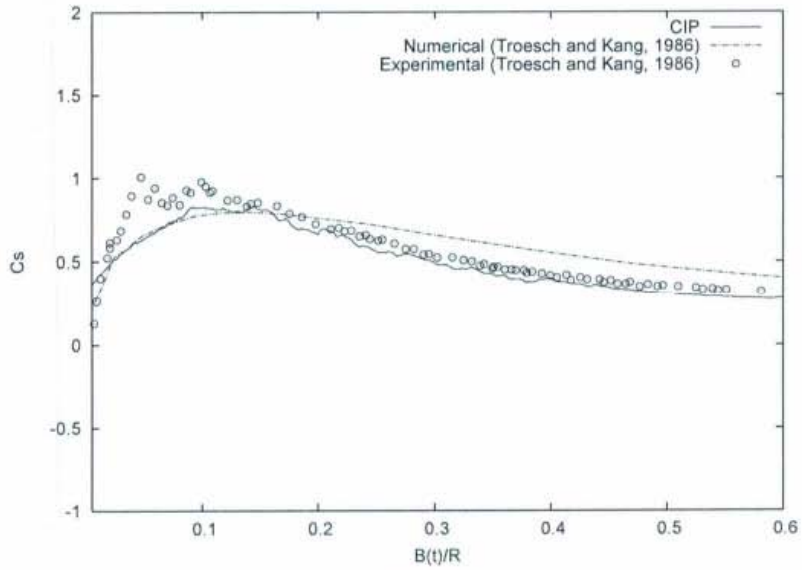

(a) Vertical

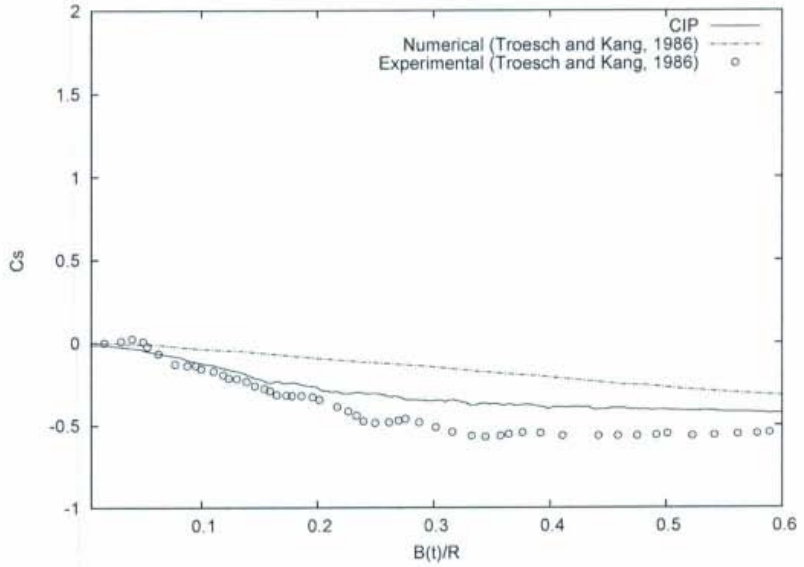

(b) Horizontal

Figure 3-21: Time history of the slamming forces on a sphere (Fn=2.2030)

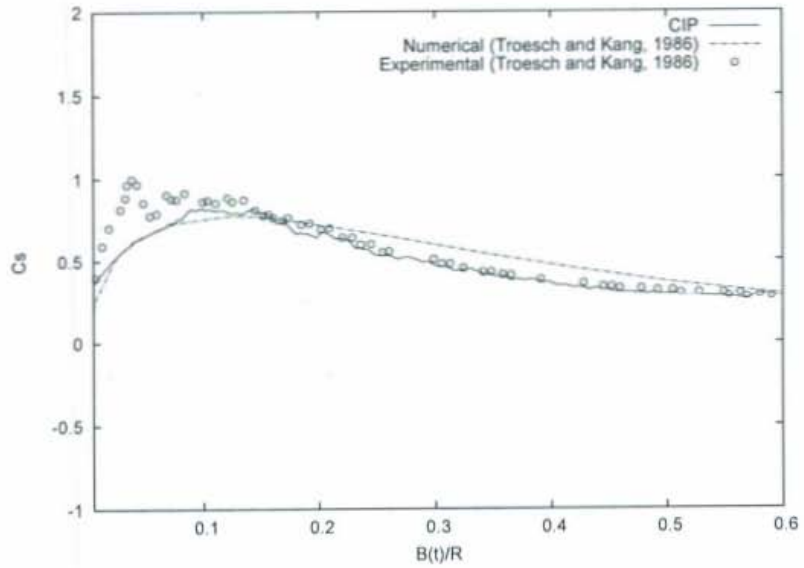

(a) Vertical

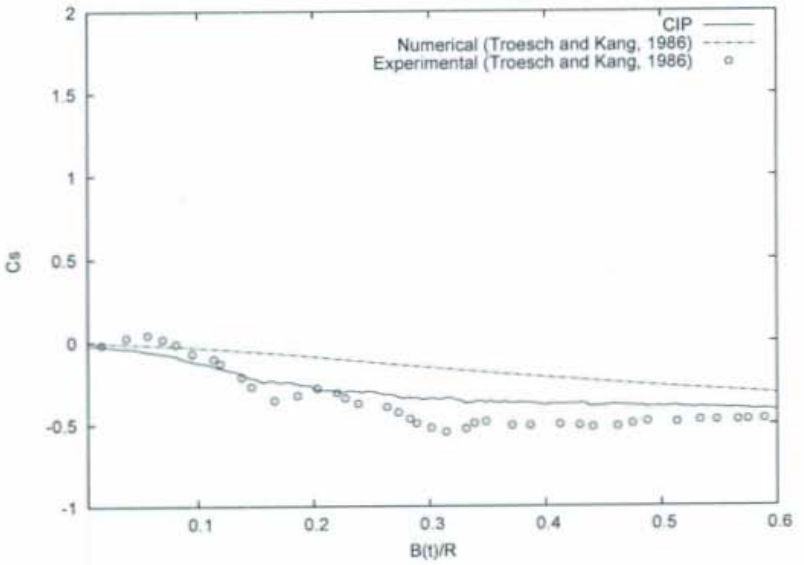

(b) Horizontal

Figure 3-22: Time history of the slamming forces on a sphere (Fn=3.1156)

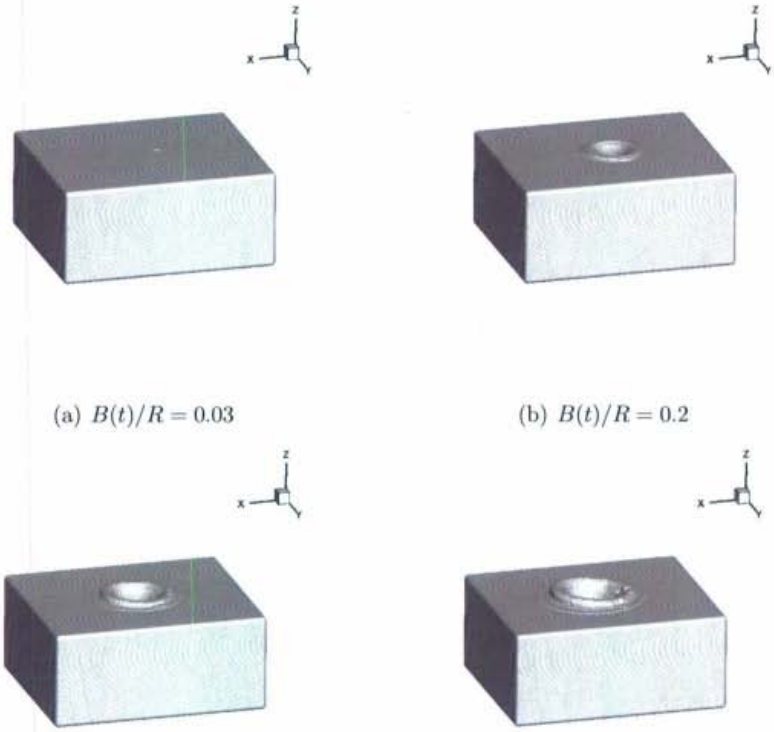

(a) $B(t)/R = 0.03$ (b) $B(t)/R = 0.2$

(c) $B(t)/R = 0.4$ (d) $B(t)/R = 0.6$

Figure 3-23: Free surface elevation during the water entry of a sphere entering calm water obliquely (Fn=2.2030)

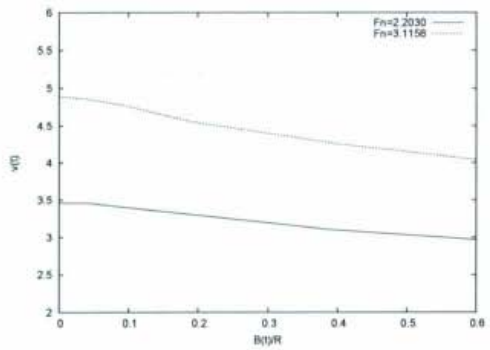

Figure 3-24: Velocities in the computation

Table 3.6: RMSE of the numerical solutions by the CIP method

Vertical slamming force in Fig. 3-21 (a) (Fn=2.2030):	14.25%
Horizontal slamming force in Fig. 3-21 (b) (Fn=2.2030):	28.4%
Vertical slamming force in Fig. 3-22 (a) (Fn=3.1156):	11.9%
Horizontal slamming force in Fig. 3-22 (b) (Fn=3.1156):	21.94%

3.6 Water Entry of a 3D Planing Hull

The prediction of slamming forces is important in the simulation of planing hull motions. The computation of slamming forces is usually based on 2D potential flow theory and CFD solutions. The computations of slamming forces based on 3D methods are relatively rare. The objective of this work is to investigate the slamming phenomena on a planing hull using a 3D numerical method.

The computations were carried out to a prismatic planing hull (Fridsma, 1969) entering calm water with different pitch and roll angles. The prismatic hull geometry is shown in Fig. 3-25. The hull features constant deadrise through its length, and vertical sides above its single chine. The chine and keel line are horizontal from the stern to a point one-fifth of the length aft of the bow, where the keel and chine are elliptical in elevation and the chine and deck line are elliptical in planform. The computational model is shown in Fig. 3-26. The surface of the planing hull was represented by 10,975 rectangular panels in the computation. The computational grid was $180 \times 80 \times 160$ and the time step was chosen as 4.28×10^{-4} s. The computational domain size was $2.5\ m \times 1\ m \times 2\ m$. In the computation, the pitch and roll angles were 0, 5, and 10 degrees, respectively.

The 3D results are compared with strip theory solution. The actual fluid mechanical problem is simplified through a strip approach. The force on the hull is approximated by determining the section load at a number of sections, or strips (see Fig. 3-27 (a)). The 2D section calculations are expressed in terms of 2D CIP method (Yang, 2007). In the 2D computation, in order to consider the effects of pitch, the drop velocity in

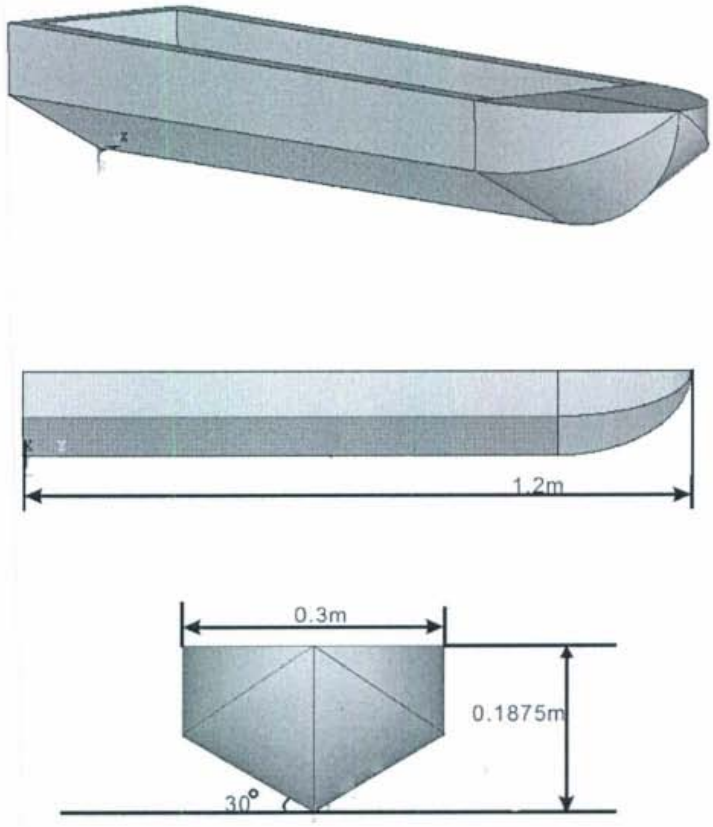

Figure 3-25: Geometry of a 3D planing hull

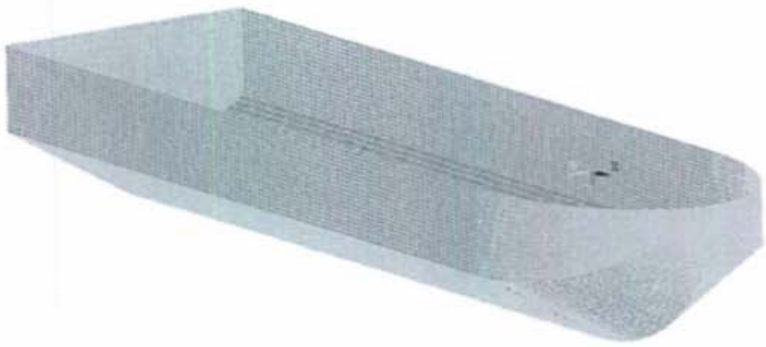

Figure 3-26: Computational model of a 3D planing hull

the 2D section plane is

$$V^{'} = Vcos(\theta) \tag{3.5}$$

where θ is the pitch angle and V is the drop velocity in the vertical direction (Fig. 3-27 (b)).

Then the vertical slamming force on each section is obtained by

$$F = F^{'}/cos(\theta) \tag{3.6}$$

$F^{'}$ is the force calculated by the velocity in the 2D section plane. The total vertical slamming force is

$$F_{total} = \Sigma F ds \tag{3.7}$$

Fig. 3-28 shows the maximum slamming force coefficients with different pitch and roll angles. The slamming coefficient is given by $C_s = \frac{F}{0.5\rho V^2 L^2}$ where L is the length of hull and V is the vertical velocity (V=0.925 m/s). From these figures, it can be seen that the 2D results are a little higher than the 3D solution. The main reason is due to 3D flow effects. As discussed previously, the 3D effects tend to cause a reduction

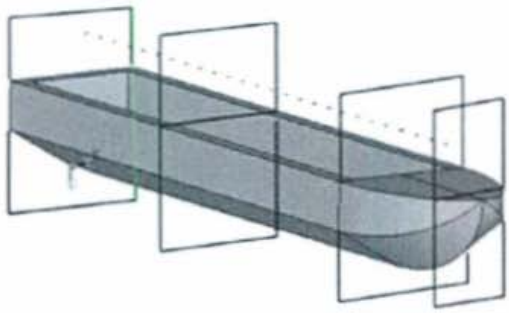

(a)

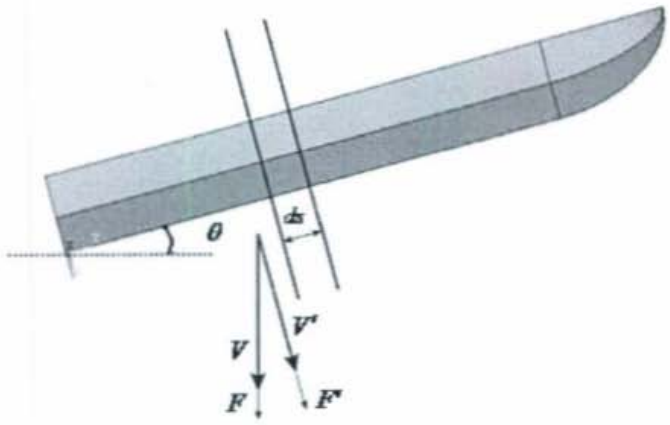

(b)

Figure 3-27: 2D strip and force/velocity components

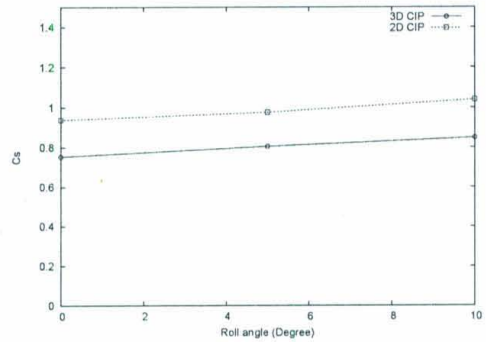

(a) Pitch 0

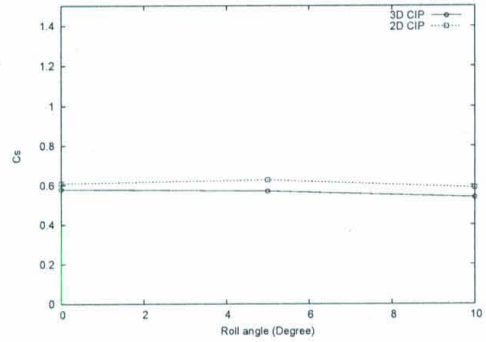

(b) Pitch 5

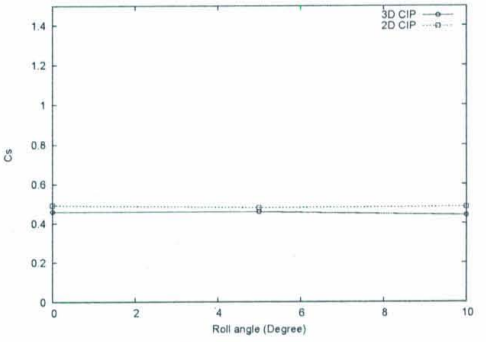

(c) Pitch 10

Figure 3-28: Maximum slamming force coefficient for different roll and pitch angles

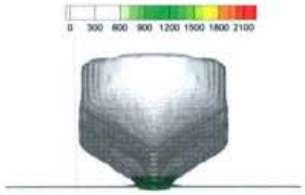

(a) $t = 0$

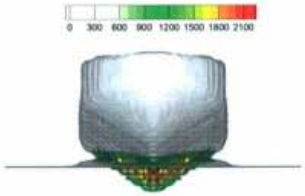

(b) $t = 0.04$

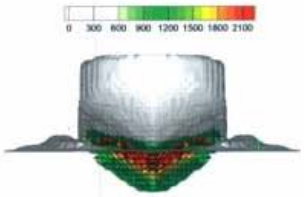

(c) $t = 0.08$

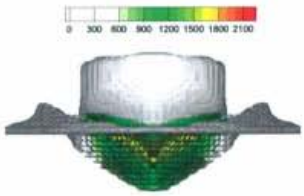

(d) $t = 0.12$

Figure 3-29: Pressure distribution (Pa) on a planing hull entering calm water (pitch=5 degrees and roll=0)

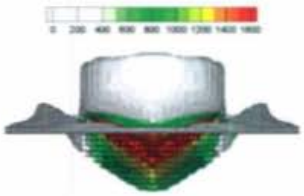

(a) pitch 5 & roll 0

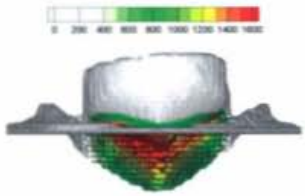

(b) pitch 5 & roll 5

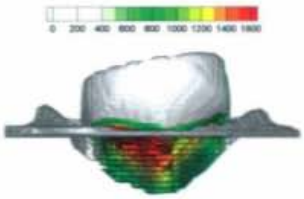

(c) pitch 5 & roll 10

Figure 3-30: Pressure distribution (Pa) on a planing hull at 5 pitch angles and different roll angles

of vertical slamming force on a wedge. This observation seems to be consistent. The difference between the 2D and 3D results become smaller with increasing pitch angle. The maximum slamming force coefficients predicted by the two methods increase slightly as the roll angle is increased.

Fig. 3-29 presents the pressure distribution of the planing hull entering water at 5 degrees pitch angle and zero roll angle at various time instants. Jets are generated around the hull, and peak pressure occurs near the jet roots. The peak pressure keeps changing positions with the moving of water jets during water entry. Fig. 3-30 shows pressure distributions on the planing hull at different roll angles. As we can see, at zero roll angle, the pressure distribution is almost uniform over the hull bottom. For asymmetrical water entries, the peak pressures occur at the water jet roots on the side of hulls with smaller deadrise angles.

Chapter 4

Water Entry of 3D Bodies with Free-Fall Motion

The problem of a 3D body entering calm water with free-fall motion has been studied. The computations have been carried out for cylinders, catamaran models and a ship section. The predicted motion has been compared with experimental results.

4.1 Water Entry of 3D Cylinders

Computations have been carried out for the free-fall of 3D cylinders entering calm water. Numerical results were compared with experimental data presented by Greenhow and Lin (1983). Greenhow and Lin (1983) did free drop tests of horizontal circular cylinders into initially calm water. A half-buoyant and a neutrally buoyant cylinder with a radius of 0.055 m and 1 m in length are used in the validation studies. The depth of water is 0.3 m. Half buoyant means that the cylinder's weight equals half of the buoyancy force on a totally submerged cylinder, while the neutrally buoyant means the weight equals the buoyancy force. Both cylinders were dropped from

Figure 4-1: Computational model of a 3D cylinder

a height of 0.5 m between the lowest point of the cylinder and the undisturbed free surface. The computational model in the present computation is shown in Fig. 4-1. The surface of the cylinder was represented by 9,194 rectangular panels. The computational grid was $178 \times 78 \times 158$ and the time step was chosen as 1.02×10^{-3} s. The computational domain size was $1.12\ m \times 0.56\ m \times 0.56\ m$.

Fig. 4-2 presents the time history of the depth of penetration for the half-buoyant and neutrally buoyant cylinders. The calculated results for the penetration depth into the water were compared with the experimental results by Greenhow and Lin (1983). For the half-buoyant cylinder, there is good agreement between the numerical results and experimental data. For the neutrally buoyant cylinder, reasonable agreement is obtained, except at one experimental value which obviously deviates from the other data. As indicated by Greenhow and Lin (1983), there were some measuring errors in the model test. The root mean square errors of the numerical solutions predicted by the CIP method relative to experimental results were given in Table 4.1. Fig. 4-3 shows the numerical results by 2D BEM (Sun, 2007), and the numerical solution is very close to the present simulation.

Figs. 4-4 and 4-5 show the free surface deformations during water entry of the

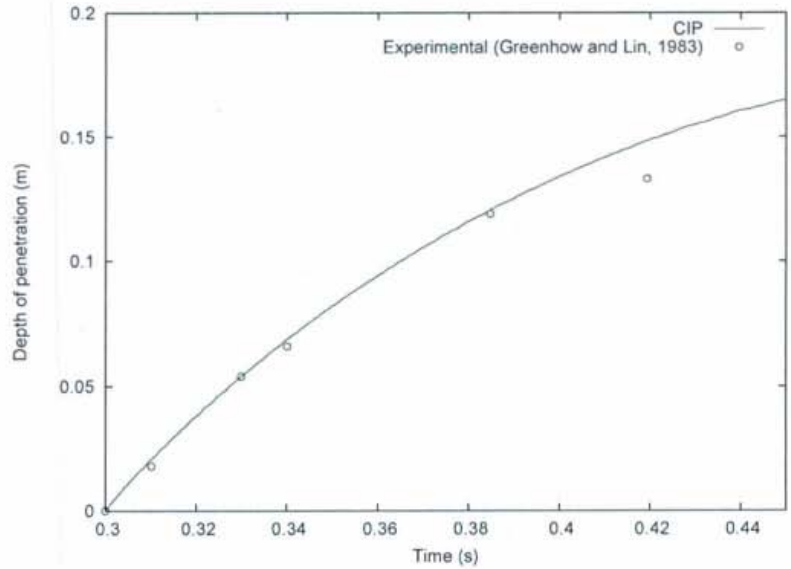

(a) Half-buoyant cylinder

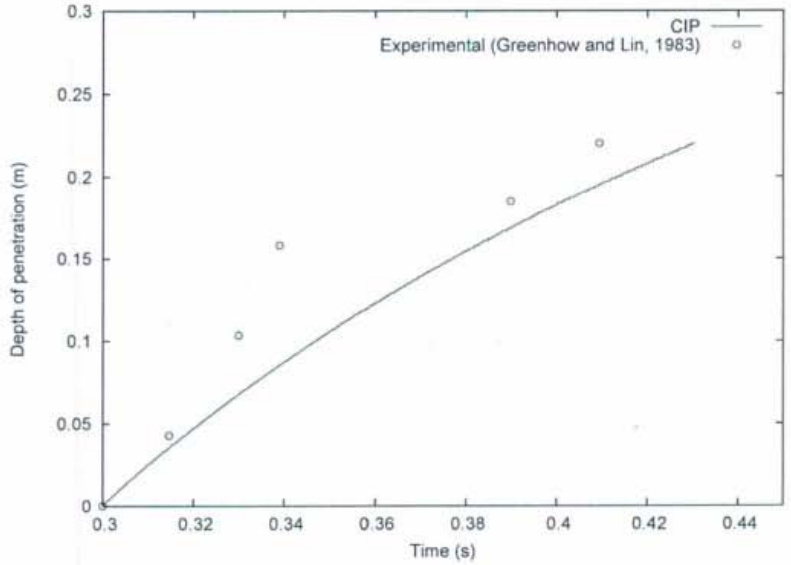

(b) Neutrally buoyant cylinder

Figure 4-2: Depth of penetration during water entry of cylinders

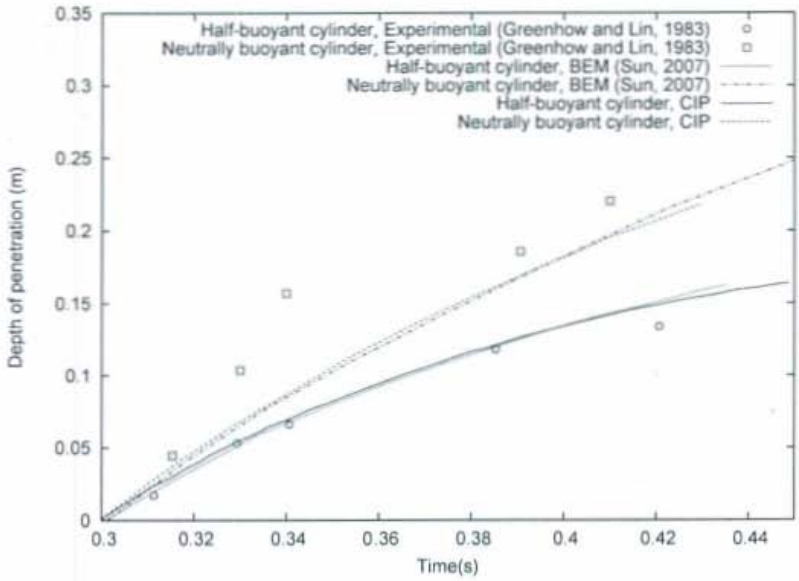

Figure 4-3: Numerical results by Sun (2007)

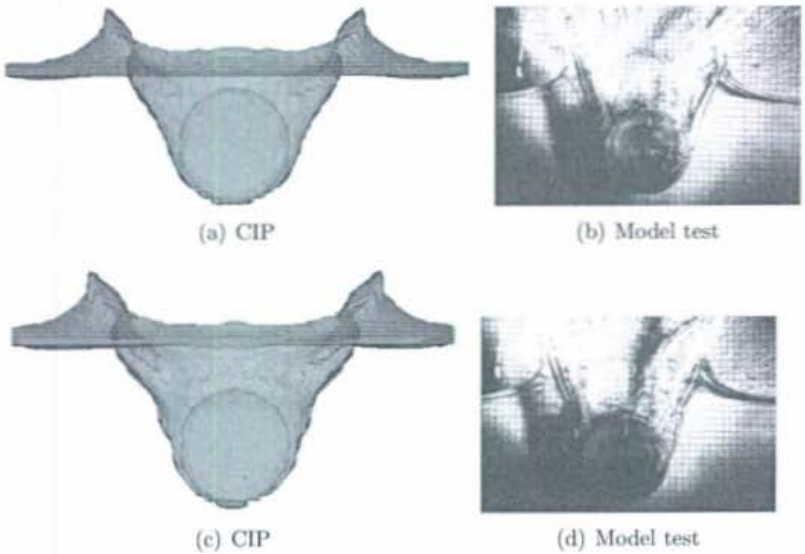

(a) CIP (b) Model test

(c) CIP (d) Model test

Figure 4-4: Free surface deformation during water entry of a half-buoyant circular cylinder

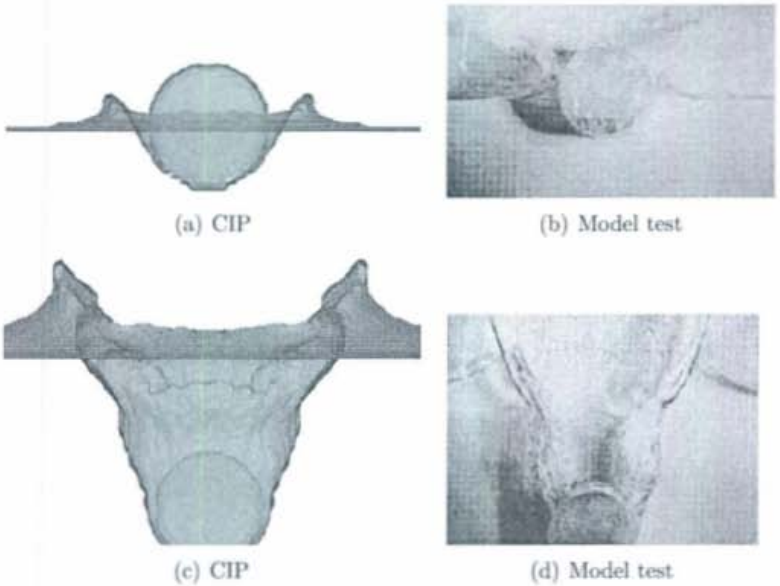

(a) CIP (b) Model test

(c) CIP (d) Model test

Figure 4-5: Free surface deformation during water entry of a neutrally buoyant cylinder

Table 4.1: RMSE of the numerical solutions by the CIP method

Depth of half-buoyant cylinder in Fig. 4-2 (a):	7.38%
Depth of neutrally buoyant cylinder in Fig. 4-2 (b):	24.71%

half-buoyant and neutrally buoyant cylinders, respectively. These figures show in general satisfactory agreement between the numerical results and experimental results. Actually, the resolution of the grid has a great influence on the formation of the jets aside the cylinder. As shown in Fig. 4-6, the jet formation becomes "blunt" with coarser grid. A very fine grid is needed to capture the jets. However, it is difficult for a 3D simulation using a very fine grid due to the limitation of computer resource and computational time.

Fig. 4-7 shows a comparison of computed jets with a 2D simulation (fine grid) and the $\sqrt{3}-$ ellipse theory (Greenhow and Lin, 1983). Greenhow and Lin found that the shape of $\sqrt{3}-$ ellipse fitted the jet geometry from their model tests. The computed

(a) Grid number: 800×700

(b) Grid number: 500×400

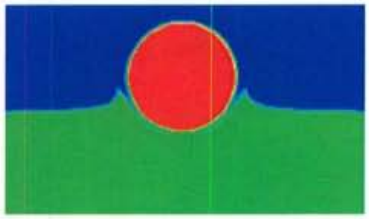

(c) Grid number: 400×300

(d) Grid number: 300×200

Figure 4-6: Effect of grid refinement on the jets (2D)

(a) Numerical (2D)

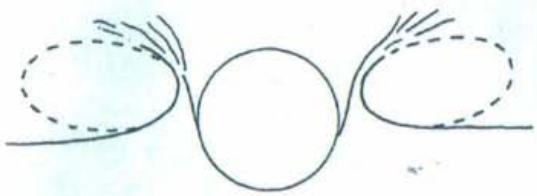

(b) $\sqrt{3}-$ ellipse

Figure 4-7: Comparison of computed jets

results generally agree with that by the $\sqrt{3}-$ ellipse theory.

4.2 Water Entry of a 3D Catamaran Model

(a) Computational model (b) Section geometry

Figure 4-8: Geometry of a 3D catamaran model

The water entry of a catamaran with free-fall motion has been studied. The catamaran hull experiences cross-deck slamming during water entry. A model drop test was carried out by Davis and Whelan (2007). The geometry of cross section is shown in Fig. 4-8 (b). The computational model is shown in Fig. 4-8 (a). The surface of the cylinder was represented by 8,598 panels in the computation. The computational grid was 100 × 100 × 110 and the time step was chosen as 1.84×10^{-4} s. The computational domain size was $1.3\ m \times 1.3\ m \times 1.5\ m$.

There are two main parameters used in the drop tests, the non-dimensional drop height (H/L) which defines the maximum velocity just prior to the water entry and the mass ratio $m^* = m_m/\rho T L^2$, where H is the drop height from the water surface to the top of the wet deck when the model is released, L is the overall width (0.544 m) of the model, m_m is the model mass, ρ is the water density and T is the length of the model (0.5 m). Note that the velocity of a large mass ratio model is not greatly

reduced when the model enters water. A small mass ratio model leads to a greater velocity reduction.

The ratios of hull velocity C_v defined as the velocity at the time when the top of the wet deck arch touches the initial water level to the velocity at initial water contact at various drop heights are compared with the experimental results. The comparisons were made for two mass ratios, m^*=0.29 and 0.58.

As shown in Fig. 4-9, the trend of the predicted values is in good agreement with that of the experimental data, while the CIP method over-predicts the velocity ratios, especially for large drop heights. Note that the compressibility of air was not taken into account in the computations, which could lead to the over-prediction. Residual air is entrained at the top of the arch due to bubble formation by turbulent mixing and this modifies the effect of the slamming force on the hull. A very fine grid is required to simulate the compressible air. However, it is very time-consuming for 3D simulations using a very fine grid due to the limitation of computer resource. The compressible air was therefore neglected for this case. In the work of Davis and Whelan (2007), an added mass theory was used to simulate slamming problem. The entrained air at the top of the arch was modeled as a spring. They gave a better prediction for the case of $m^* = 0.58$. However, their results under-predicted the velocity ratio for the case of $m^* = 0.29$ for small drop heights. The root mean square errors of the numerical solutions predicted by the CIP method relative to experimental results were given in Table 4.2.

Table 4.2: RMSE of the numerical solutions by the CIP method

Velocity ratio $m^* = 0.29$ in Fig. 4-9 (a):	32.91%
Velocity ratio $m^* = 0.58$ in Fig. 4-9 (b):	31.11%

The computed free surface elevations for the catamaran were compared with the test results by Davis and Whelan (2007) as shown in Fig. 4-10. The visual comparison indicates that the predicted free surface elevation on such a catamaran model is rather

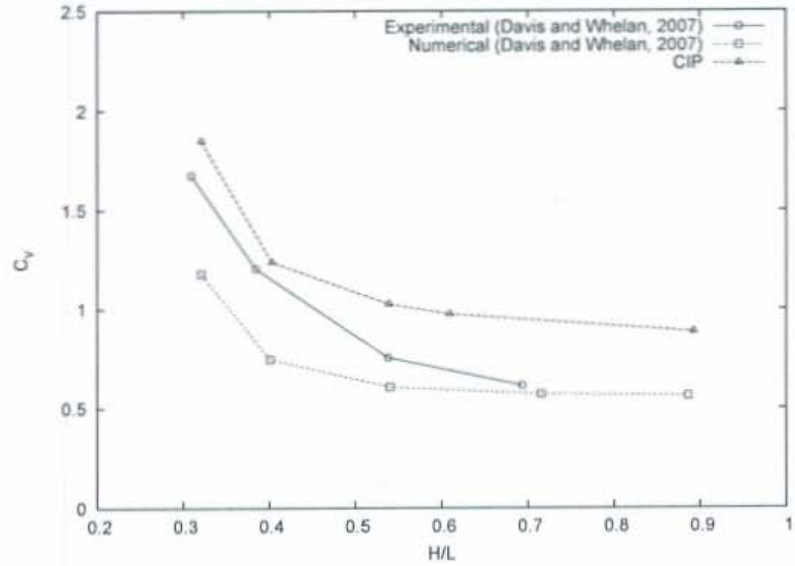

(a) $m^* = 0.29$

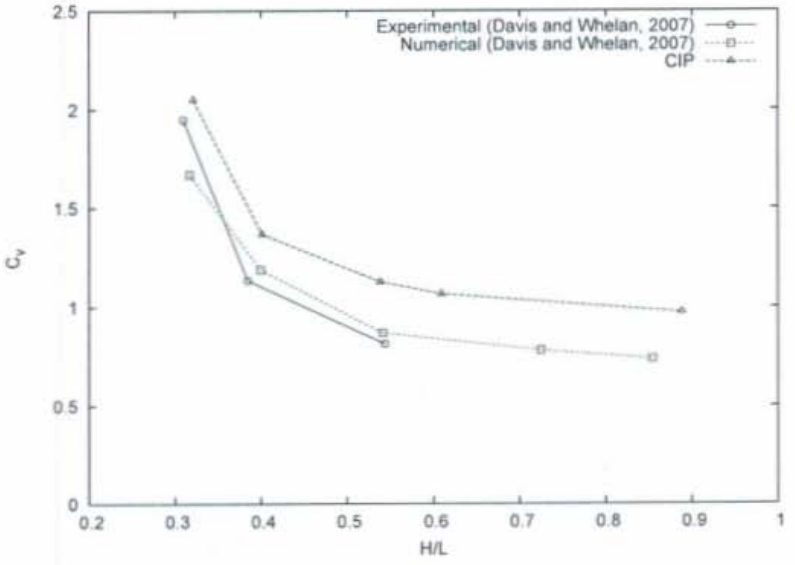

(b) $m^* = 0.58$

Figure 4-9: Velocity ratio of catamaran models

moderate. The free surface deformation was not captured very well in details. As mentioned previously, the coarseness of the grid has great influence on the formation of the jets in the Cartesian grid approach. To improve the computational quality of the free surface, a very fine grid is needed. It is again limited by the available computer resource for serial computations. In addition, complexity of the geometry can also contribute to the discrepancies.

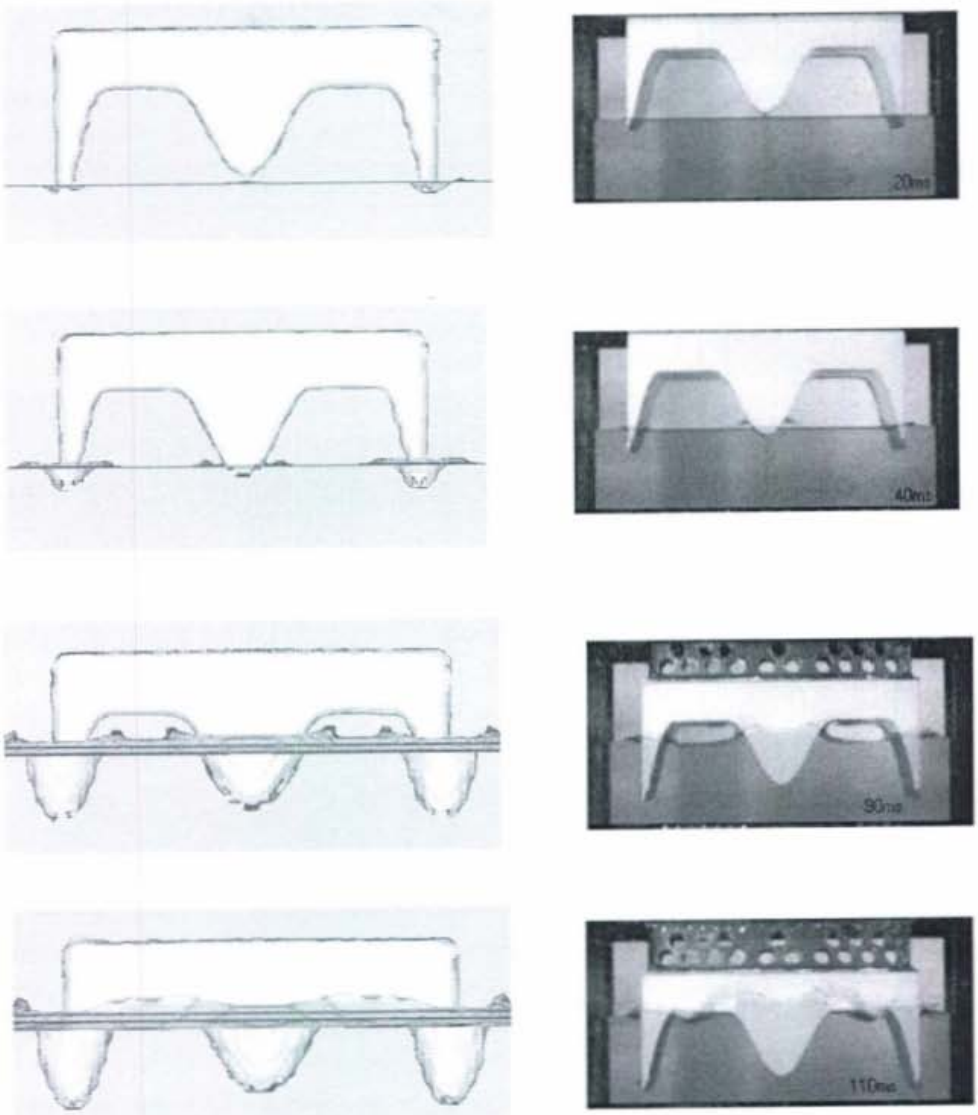

Figure 4-10: Comparison of free surface elevations at m^*=0.29, H/L=0.8 (Left: computed, Right: experimental)

4.3 Asymmetric Water Entry of a 3D Ship Section

The drop tests of a ship-bow section in Aarsnes (1996) with different roll angles have also been studied. The same model as in the symmetric cases discussed in Section 3.3 was used in the drop tests. The only difference is that the section enters the water with a roll angle (See Fig. 4-11). The computational conditions are the same as those in Section 3.3.

Figure 4-11: Asymmetric water entry of a 3D ship section

Figs. 4-12 and 4-13 show the comparisons between the present calculations by the CIP method and the experiments for the tilt angle of 28.3°. The numerical results presented in Sun (2007) by the 2D BEM method are also presented. From the Fig. 4-12, it can be seen that the present calculation for vertical hydrodynamic force agrees well with the experimental result. However, it under-predicts the horizontal hydrodynamic force. Fig. 4-13 shows the comparisons of the acceleration and velocity. The calculations show reasonable agreement with the experimental results.

Figs. 4-14 and 4-15 show the comparisons for the tilt angle of 20.3°. The calculations are in agreement with the experimental results for the hydrodynamic forces. There are some discrepancies in the acceleration and velocity results at the later time for this case. As shown in Fig. 4-15, near the end of the time histories, the measured

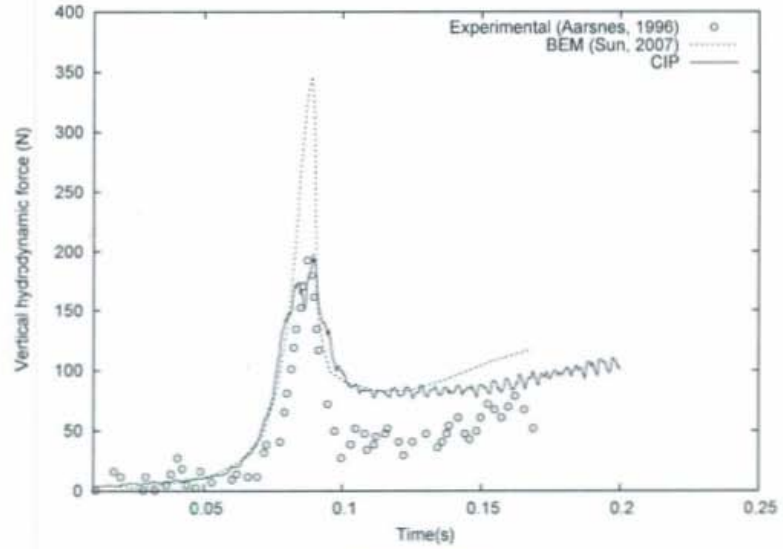

(a) Vertical force

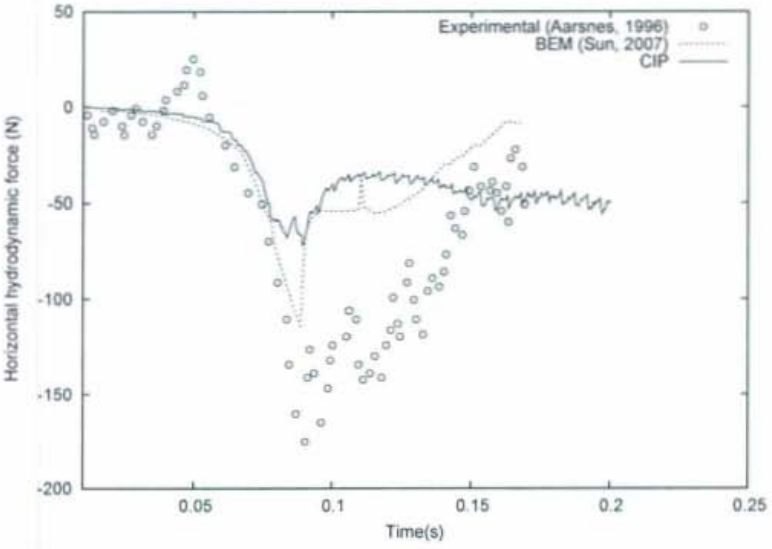

(b) Horizontal force

Figure 4-12: Measured and calculated hydrodynamic force ($tilt$: 28.3°)

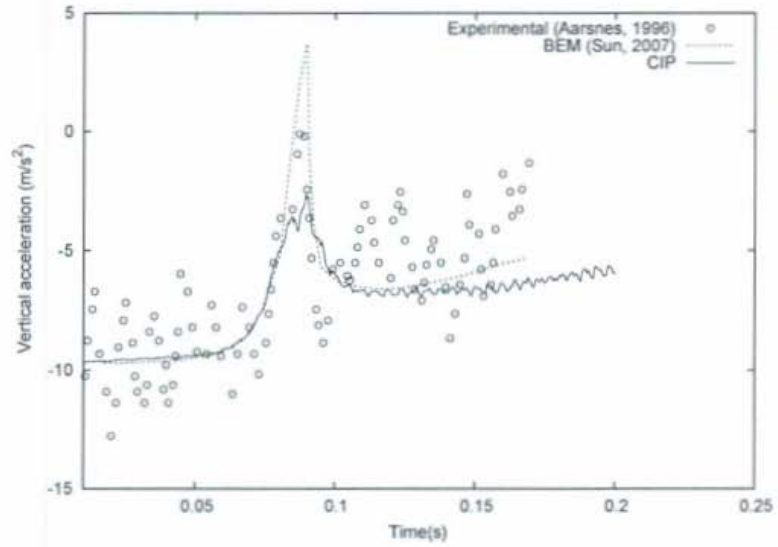

(a) Acceleration

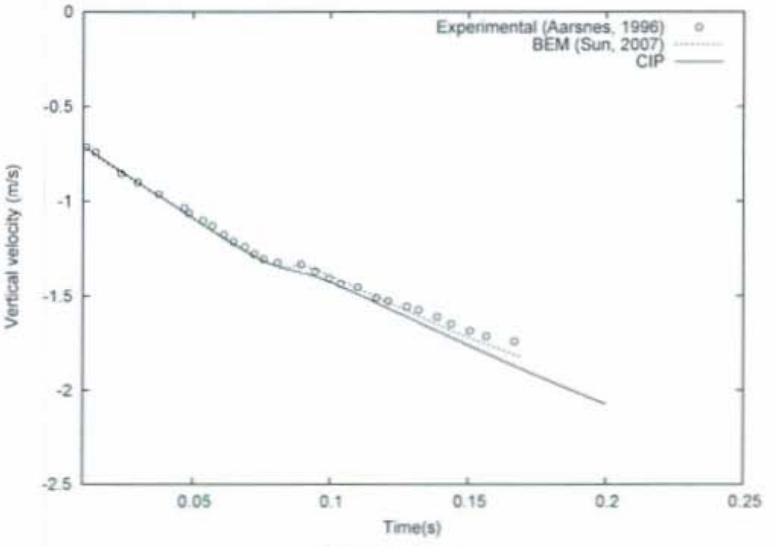

(b) Velocity

Figure 4-13: Measured and calculated acceleration and velocity ($tilt$: 28.3^o)

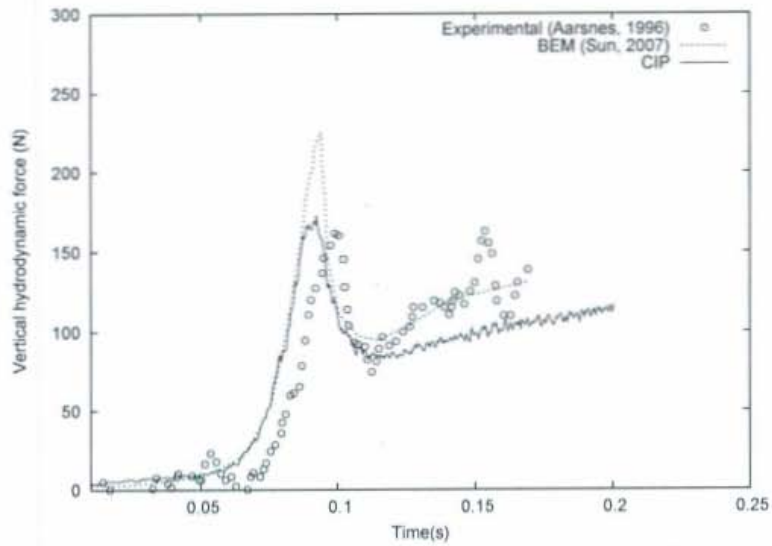

(a) Vertical force

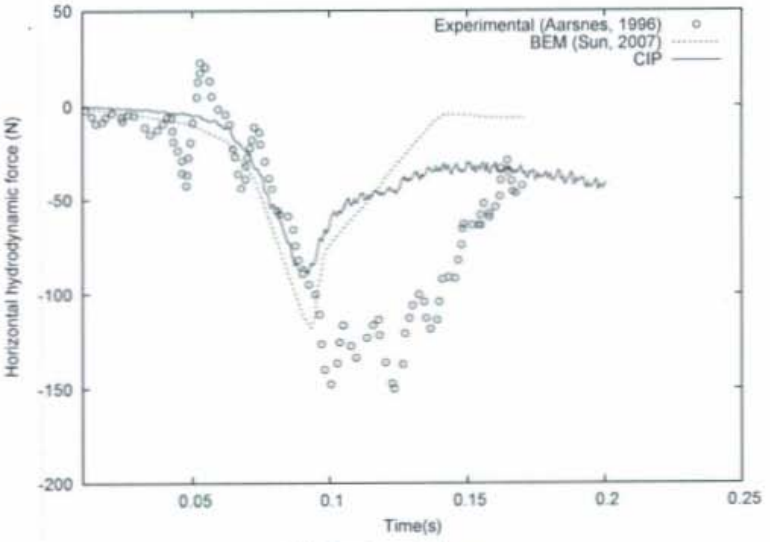

(b) Horizontal force

Figure 4-14: Measured and calculated hydrodynamic force ($tilt : 20.3^o$)

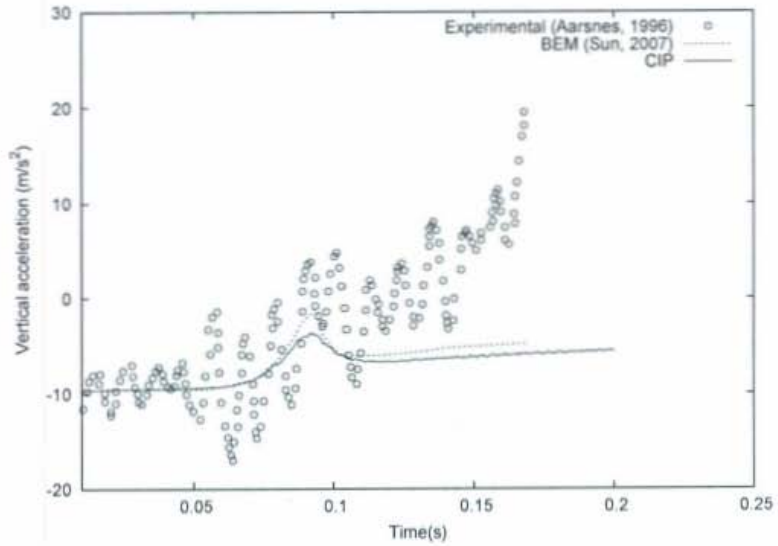

(a) Acceleration

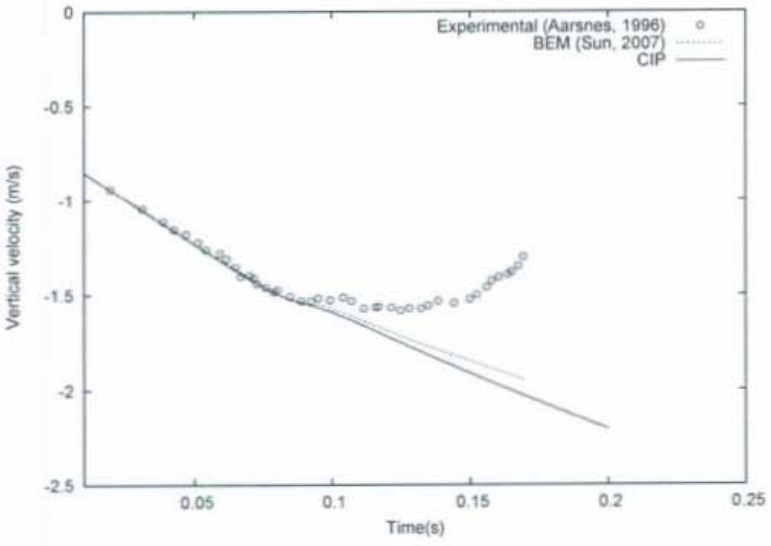

(b) Velocity

Figure 4-15: Measured and calculated acceleration and velocity ($tilt$: 20.3^o)

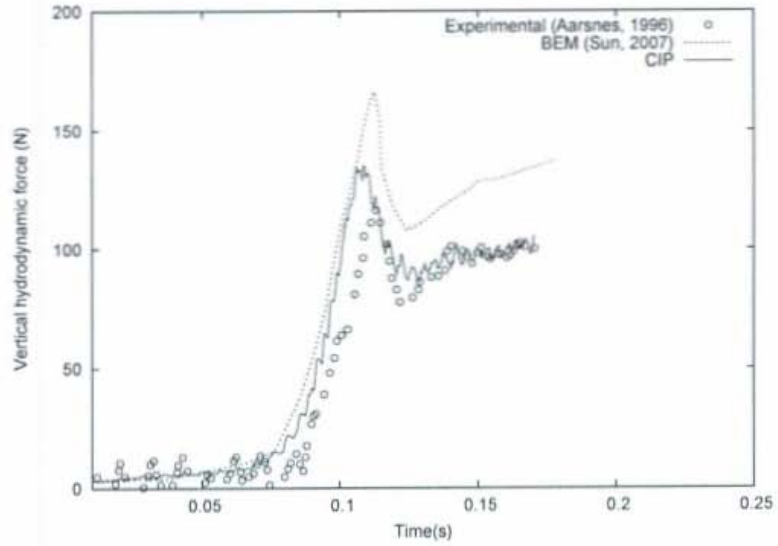

(a) Vertical force

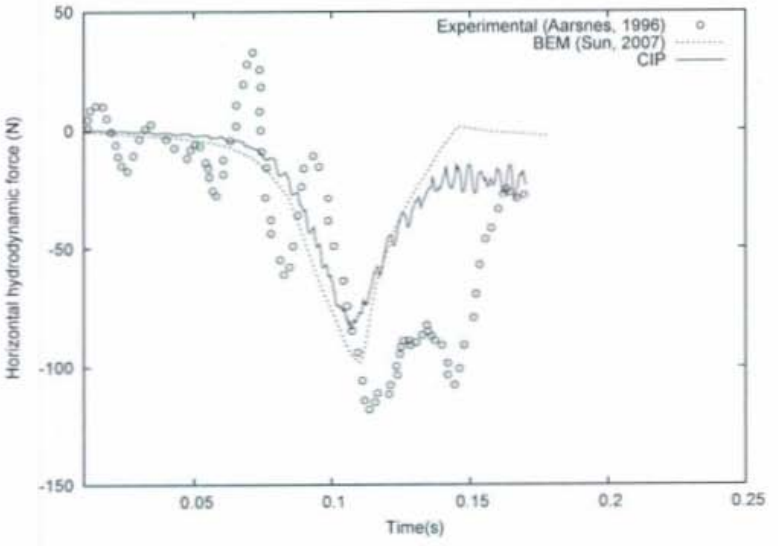

(b) Horizontal force

Figure 4-16: Measured and calculated hydrodynamic force ($tilt$: 20.3°)

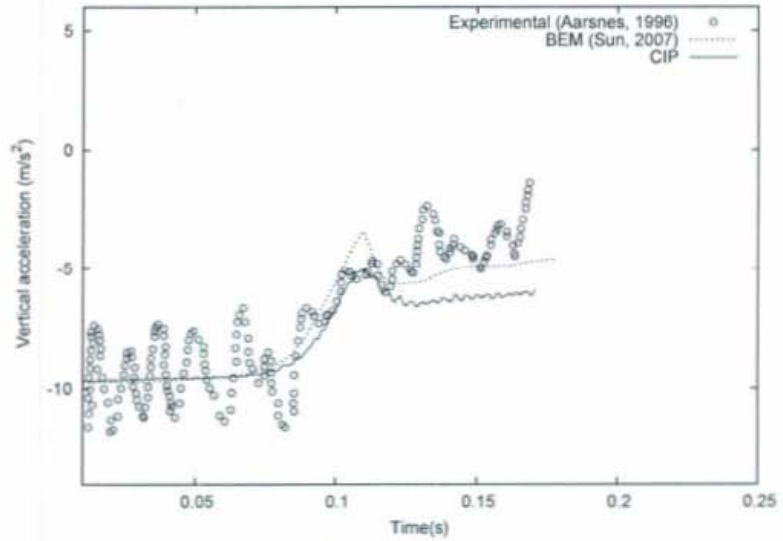

(a) Acceleration

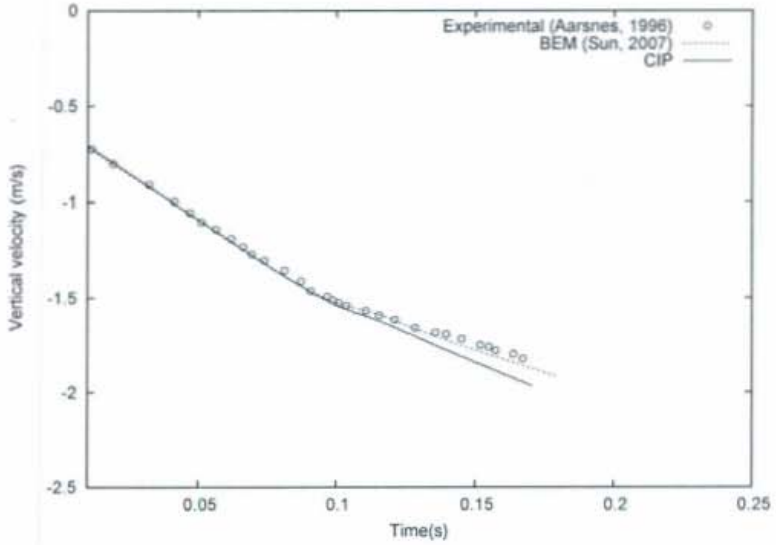

(b) Velocity

Figure 4-17: Measured and calculated acceleration and velocity ($tilt$: 14.7^o)

accelerations increase and the resulting water entry speeds suddenly decrease. Elastic ropes were used to stop the model at the later stage of the water entry in the model test. Experimental bias errors caused by this fact can account for the apparent discrepancies in the acceleration and velocity results at the later time for this case.

Figs. 4-14 and 4-15 show the comparisons for the tilt angle of 14.7^o. The calculations show reasonable agreement with the experiments in this case. The oscillation in the experimental results for the accelerations are due to the vibrations of the drop rig during the test.

Chapter 5

Conclusions and Future Work

5.1 Conclusions

This thesis presents a numerical method for simulating 3D strongly nonlinear slamming problems. The study has been focused on developing a numerical tool for predicting slamming loads on ships and offshore structures with an objective to improve the design and their effective operations. The present computations include symmetric and asymmetric water entries with prescribed entry velocities and free-fall motions. The main contributions of the research work can be summarized as follows:

Three-dimensional nonlinear free surface. In the work, the 2D Constrained Interpolation Profile (CIP) method (Yang, 2007) was further developed to simulate the 3D nonlinear free surface problems. The CIP method is a compact upwind scheme with subcell resolution for advection calculations. It does not involve any interface construction procedure and is economical for 3D applications. In the CIP method, a cubic interpolation function is constructed, and a high-order scheme is achieved.

Coupled motion simulation. In order to simulate the slamming problem for bodies

with free motion, the coupled motions of a 3D body and fluid have been solved. In the present research, slamming forces and moments were obtained from the Navier-Stokes equations which were solved by a CIP-based finite difference method. The motion of a solid body was predicted by numerical integration of differential equations of motions. The fluid velocities due to the body motion were calculated, and used for capturing the free surface.

Solid body interface capturing method. A panel-based numerical method was developed in this work to model the arbitrary 3D moving body interface. The body surface was represented by a set of panels. The panel can be triangular, quadrilateral or hybrid of them. Since the body is assumed to be rigid, the panels can be used to update the body position with a Lagrangian method in each time step. The contribution of each panel was estimated by the contribution factor in each computational grid cell. Then the density function for a solid body was obtained, and the solid phase was modeled in a fixed computational grid.

Validation studies of the present method were carried out for several 3D bodies entering calm water symmetrically and asymmetrically with prescribed velocities and free-fall motions.

- Water entries of 3D bodies with prescribed velocities were first studied. For the water entry of a 3D wedge, 3D flow effects were investigated. 3D flow effects tend to cause a reduction in slamming force. The computed slamming forces are in good agreement with experimental results. For the sphere entering calm water obliquely, the computed vertical and horizontal slamming forces in general agree well with experimental results.

- The simulations were further carried out for a couple of bodies with complex geometry. For the water entry of a 3D ship section, pressures near the knuckles were under-predicted by the numerical method. Similar to the case

of a 3D wedge, the discrepancies are presumedly due to the loss of interface sharpness and therefore inaccurate body boundary conditions caused by the immersed boundary method. In addition, the spray jets near the knuckles were not captured very well. The loss of spray jets may also contribute to the discrepancies. The slamming force on a 3D flared body was also computed by the present numerical method, and the predicted slamming forces are in good agreement with the experimental results.

- The maximum slamming force coefficients of a planing hull with different pitch and roll angles were computed by the present numerical method and compared with these by the 2D strip theory. The 2D results are slightly greater than the 3D solutions. The main reason is due to 3D flow effects. The 3D effects tend to cause a reduction of vertical slamming force.

- The studies were then extended to 3D bodies entering calm water with free-fall motions. The predicted motion of the half-buoyant cylinder with free-fall motion agrees well with the experimental data. For the neutrally buoyant cylinder, reasonable agreement is obtained, except at one experimental value which obviously deviates from the other data. The complicated free surface elevations during water entry of cylinder were simulated by the present numerical method. They are visually in good agreement with the photographs taken from the experiments.

- The present numerical method over-predicts the velocity ratios for water entry of a catamaran, especially for large drop heights. The compressibility of air was not taken into account in the present computations, which could lead to the over-prediction.

- Velocity, acceleration, as well as vertical and horizontal hydrodynamic forces as a function of time were predicted by the present numerical method for

the asymmetric water entry of a ship section. A satisfactory agreement with experimental drop test results is demonstrated.

In addition, the present method was compared with the conventional boundary element method. In most of cases, the CIP method gives better predictions of slamming forces and pressure than the boundary element method, since the CIP method overcomes the difficulties in treating highly distorted or breaking free surfaces and the flow separations.

5.2 Future Work

In order to make the calculation more accurate and efficient, the following aspects need to be addressed in future work.

1. To apply the boundary condition at the exact location of the boundary. The interface is not explicitly tracked but is reconstructed from the field variables on a fixed computational grid. The location of the interface can be determined based on the volume fraction information, unavoidably resulting in losing some accuracies when details of the interface can not be covered by grids. An accurate boundary condition application method on the geometry needs to be developed.

2. Parallel computational technique. In comparison with the boundary element method, the present numerical method is time-consuming. A parallel computational technique should be developed to improve the computing efficiency. In addition, the resolution of the grid has great influence on the formation of the water jets. The current studies were limited by computer resource and grid resolution. A parallel computational technique can also improve computing efficiency for fine grid resolution.

3. To simulate the case when the 3D body has an arch deck, i.e. the catamaran model, the predicted results have large discrepancies with the experimental result. The main reason is the effect of the air compressibility. Residual air is entrained at the top of the arch due to bubble formation by turbulent mixing and this affects the slamming loads on the deck. An algorithm should be developed to include the effects of compressible air in 3D simulations during the water impacts.

References

Aarsnes, J.V., 1996, Drop test with ship sections-effect of roll angle, MARINTEK, Trondheim, Norway.

Armand, J.L. and Cointe, R., 1986, Hydrodynamic Impact Analysis of a Cylinder, Proceedings of the 5th International Offshore Mechanics and Arctic Engineering, Tokyo, Japan, Vol. 1, pp. 609-634.

Chuang, J.M., Zhu, W. and Qiu, W., 2006, Numerical Solutions of 2D Water Entry Problem, Proceedings of ISOPE2006, San Francisco, California, USA.

Cointe, R., 1991, Free Surface Flows Close to a Surface-Piercing Body, Mathematical Approaches in Hydrodynamics, Soc. Ind. Appl. Maths, Philadelphia, pp. 319-334.

Davis, M.R. and Whelan, J.R., 2007, Computation of Wet Deck Bow Slam Loads for Catamaran Arched Cross Sections, Ocean Engineering, Vol. 34, pp. 2265-2276.

De Backer, G., Vantorre, M., Beels, C., De Pré, J., Victor, S., De Roucka J., Blommaertb, C. and Van Paepegemb, M., 2009, Experimental Investigation of Water Impact on Axisymmetric Bodies, Applied Ocean Research, Vol. 31, pp. 143-156.

Dobrovol'skaya, Z.N., 1969, On some Problems of Similarity Flow of Fluid with a Free Surface, Journal of Fluid Mechanics, Vol. 36, pp. 805-829.

Faltinsen, O.M. and Chezhian, M., 2005, A Generalized Wagner Method for Three-Dimensional Slamming, Journal of Ship Research, Vol. 49, No. 4, pp. 279-287.

Faltinsen, O.M., Landrini, M. and Greco, M., 2004, Slamming in Marine Applications, Journal of Engineering Mathematics, Vol. 48, pp. 187217.

Fekken, G., 2004, Numerical Simulation of Free Surface Flow with Moving Rigid Bodies. Ph.D. thesis, Faculty of Mathematics and Natural sciences, University of Groningen.

Fridsma, G., 1969, A Systematic Study of the Rough Water Performance of Planing Boats, Technical Report. 1275, Stevens Institute of Technology, Davidson Laboratory.

Gingold, R.A. and Monaghan, J.J., 1977, Smoothed Particle Hydrodynamics: Theory and Application to Non-Sperical Stars, Monthly Notices of Royal Astronomical Society, Vol. 181, pp. 375-389.

Greenhow, M., 1987, Wedge Entry into Initially Calm Water, Applied Ocean Research, Vol. 9, pp. 214-223.

Greenhow, M. and Lin, W.M., 1983, Nonlinear Free Surface Effects: Experiments and Theory, Report No. 83-19, Department of Ocean Engineering, MIT, Cambridge, MA.

Hestenes, M. R. and Stiefel, E., 1952, Methods of Conjugate Gradients for Solving Linear Systems, J. Res. Natl. Bur. Stand. Vol.49, pp. 409-436.

Hirt, C.W. and Nichols, B.D., 1981, Volume of Fluid Method for the Dynamics of Free Boundaries, Journal of Computational Physics, Vol. 39, pp. 201-225.

Hirt, C.W., Cook, J.L. and Butler, T.D., 1970, A Lagrangian Method for Calculating the Dynamics of an Incompressible Fluid with Free Surface, Journal of Computational Physics, Vol. 5, pp. 103-124.

Howison, S.D., Ockendon, J.R. and Wilson, S.K., 1991, Incompressible Water Entry Problems at Small Deadrise Angles, Journal of Fluid Mechanics, Vol. 222, pp. 215-230.

Hu, C. and Kashiwagi, M., 2004, A CIP-Based Method for Numerical Simulations of Violent Free-surface Flow, J. Mar. Sci. Technol., Vol. 9, pp.143-157.

Hu, C. and Kashiwagi, M., 2007, Numerical and Experimental Studies on Three-Dimensional Water on Deck with a Modified Wigley Model, Proceedings of 9th International Conference on Numerical Ship Hydrodynamics, Ann Arbor, Michigan.

Kim, Y.W., Kim, Y., Liu, Y.M., and Yue, D.K.P., 2007, On the Water-Entry Impact Problem of Asymmetric Bodies, Proceedings of 9th International Conference on Numerical Ship Hydrodynamics, Ann Arbor, Michigan.

Kleefsman, K.M.T., Fekken, G., Veldman, A.E.P., Iwanowski, B. and Buchner, B., 2005, A Volume-of-Fluid based Simulation Method for Wave Impact Problems, Journal of Computation Physical, Vol. 206, pp. 363-393.

Korobkin, A. A. and Pukhnachov, V. V., 1988, Initial Stage of Water Impact, Ann. Rev. Fluid Mech., Vol. 20, pp. 159-185.

Leveque, R.J., 2007, Finite Difference Methods for Ordinary and Partial Differential Equations, Steady-State and Time-Dependent Problems, Society for Industrial and Applied Mathematics.

Lin, W.M., Newman, J.N. and Yue, D.K., 1984, Nonlinear Forced Motions of Floating Bodies, Proceedings of the 15th Symposium on Naval Hydrodynamics, Hamburg, German, pp. 33-47.

Maskew, B., Wang, M.L. and Troesch, A., 1994, Comparison of Calculated and Measured Loads on a Flared Body Oscillating in a Free Surface, 20th Symposium on Naval Hydrodynamics, Santa Barbera, California.

Miloh, T., 1981, Wave Slam on a Sphere Penetrating a Free Surface, Journal of Engineering Math., Vol. 15, No.3, pp. 221-240.

Monaghan, J.J., 1994, Simulating Free Surface Flows with SPH, J. Computational Physics, Vol. 110, pp. 399-406.

Nichols, B.D., Hirt, C.W. and Hotchkiss, R.S., 1980, SOLA-VOF: A Solution Algorithm for Transient Fluid Flow with Multiple Free Boundaries, Los Alamos Scientific Lab Report LA-8355.

Osher, S. and Sethian, J.A., 1988, Fronts Propagating with Curvature Dependent Speed: Algorithms based on Hamilton-Jacobi Formulations, J. Comput. Phys., Vol. 79, pp. 12-49.

Qiu, W., Peng, H. and Brennan, D., 2003, Development of Surface Geometry and External Flow Field Gridding Software for the Computation of Propeller Surface and Tip Vortex Flow-Final Report, DRDC Atlantic CR2003-91, Defence R&D Canada Atlantic, Nova Scotia, Canada.

Roache, P.J., 1998, Verification and Validation in Computational Science and Engineering, Hermosa publishers, Albuquerque, New Mexico.

Rogers, B.D., Dalrymple, R.A., Gesteira, M. and Knio, O., 2003, Smoothed Particle Hydrodynamics for Naval Hydrodynamics, 18th International Workshop on Water Waves and Floating Bodies, Le Croisic, France.

Shiffman, M. and Spencer, D.C., 1951, The Force of Impact on a Cone Striking a Water Surface, Communications on Pure and Applied Mathematics, Vol. 4, pp. 379-417.

Sussman, M. and Fatemi, E., 1999, An Efficient, Interface-Preserving Level Set Redistancing Algorithm and its Application to Interfacial Incompressible Fluid Flow, SIAM Journal on Scientific Computing, Vol. 20, pp. 1165-1191.

Sun, H., 2007, A Boundary Element Method applied to Strongly Wave-Body Interaction Problems.

Sussman, M., Smereka, P. and Osher, S., 1994, A Level Set Approach for Computing Solutions to Incompressible Two-Phase Flow, J. Comp. Phys., Vol. 114, pp. 146-159.

Takewaki, H., Nishiguchi, A. and Yabe, T., 1985, Cubic Interpolated Pseudo-Particle Method (CIP) for Solving Hyperbolic-Type Equations, J. Comput. Phys., Vol. 61, pp. 261-268.

Thoroddsen, S.T., Etoh, T.G., Takehara, K. and Takano, Y., 2004, Impact Jetting by a Solid Sphere, J. Fluid Mech., Vol. 499, pp. 139-148.

Troesch, A.W. and Kang, C.G., 1986, Hydrodynamic Impact Loads on 3D Bodies, Symposium on Naval Hydrodynamics, University of California, Berkeley.

Utsumi, T., Kunugi, T. and Aoki, T., 1997, Stability and Accuracy of the Cubic Interpolated Propagation Scheme, Comput. Phys. Commun. Vol. 101, pp. 9-20.

von Karman, T., 1929, The Impact on Seaplane Floats During Landing, NACA TN 321

Vestbøstad, T.M., Faltinsen, O.M. and Kristiansen, D., 2007, Validation Methods and Benchmark Tests for a 2D CIP Method Applied to Marine Hydrodynamics, Proceedings of the Seventeenth International Offshore and Polar Engineering Conference, Lisbon, Portugal.

Vinje, T. and Brevig, P., 1981, Nonlinear Ship Motions, Proceedings of the 3rd International Conference on Numerical Ship Hydrodynamic, Paris, pp. 257-266.

Wagner, H., 1932, *Über* Stoss-und Gleitvorgänge an der Oberfläche von Flüssigkeiten, Zeitschrift fur Angewandte Mathematik Mechanik, Vol. 12, No. 4, pp. 192-235.

Walhorn, E., Kölke, A., Hübner, B. and Dinkler, D., 2005, Fluid-Structure Coupling within a Monolithic Model Involving Free Surface Flows, Computers and Structures, Vol. 83, pp. 2100-2111.

Xiao, F., 1999, A Computational Model for Suspended Large Rigid Bodies in 3D Unsteady Viscous Flows, Journal of Computational Physics, Vol. 155, pp. 348-379.

Yabe, T., 1991, A Universal Cubic Interpolation Solver for Compressible and Incompressible Fluids, Shock Waves, Vol. 1, pp. 187-195.

Yabe, T., 2001, An Exactly Conservative Semi-Lagrangian Scheme (CIPCSL) in One Dimension, Monthly Weather Review, Vol. 129, pp. 332-344.

Yabe, T., Ishikawa, T, Wang, P.Y., Aoki, T., Kadota, Y. and Ikeda, F., 1991, A Universal Solver for Hyperbolic Equations by Cubic Polynomial Interpolation II. Two- and Three- Dimensional Solvers, Computer Physics Communication, Vol. 66, pp. 233-242.

Yabe, T., Xiao, F. and Utsumi, T., 2001, The Constrained Interpolation Profile Method for Multiphase Analysis, Journal of Computational Physics, Vol. 169, pp. 556-593.

Yang, Q., 2007, Numerical Solution of 2D Water Entry Problem with a CIP Method, Master thesis, Faculty of Engineering and applied science, Memorial University, Canada.

Yang, Q. and Qiu, W., 2007, Numerical Solution of 2D Slamming Problem with a CIP Method, International Conference on Violent Flows, VF-2007, Research Institute for Applied Mechnamics, Kyushu University, Japan.

Yang, Q. and Qiu, W., 2010, Computation of Slamming Force on 3D Bodies with a CIP Method, 29th International Conference on Ocean Mechanics and Arctic

Engineering, Shanghai, China, June 6-11

Yokoi, K., 2007, Efficient Implementation of THINC Scheme: A Simple and Practical Smoothed VOF Algorithm, Journal of Computational Physics, Vol., 226, pp. 1985-2002.

Youngs, D.L., 1982, Time-Dependent Multi-material Flow with Large Fluid Distortion, Numerical Methods for Fluid Dynamics, Aceademic Press, New York, pp. 273-285.

Youngs, D.L., 1987, An Interface Tracking Method for a 3D Eulerian Hydrodynamics Code, Technical Report AWRE/44/ 92/35, Atomic Weapons Research Establishment, Design Mathematics Division, Aldermaston, Reading, Berkshire, UK.

Zhao, R. and Faltinsen, O.M., 1993, Water Entry of Two-Dimensional Bodies, J. Fluid Mech., Vol. 246, pp. 593-612.

Zhao, R., Faltinsen, O.M. and Aarsnes, J., 1996, Water Entry of Arbitrary Two-Dimensional Sections With and Without Flow Separation, Proceedings of 21st Symposium on Naval Hydrodynamics, Trondheim, Norway.

Zheng, X., Duan, W.Y. and Wu, G.X., 2007, Numerical Simulation of Violent Free Surface through a Higher Order SPH Method, International Conference on Violent Flows, VF-2007, Research Institute for Applied Mechanics, Kyushu university, Japan.

Zhu, X., Faltinsen, O.M. and Hu, C., 2005, Water Entry and Exit of a Horizontal Circular Cylinder, 24th International Conference on Offshore Mechanics and Arctic Engineering, Halkidiki, Greece.

Appendices

Appendix A

Conjugate Gradient Method and Preconditioning

As mentioned in Chapter two, the linear equations (Eq. 2.26) obtained from pressure equation are solved by a Conjugate Gradient (CG) method. The method can be used to solve linear systems $\mathbf{Ax} = \mathbf{b}$ when the matrix $\mathbf{A}$ is symmetric positive definite (SPD), or negative definite since negating the system then gives a SPD matrix. The CG method was first proposed by Hestenes and Stiefel (1952), and further developed by Leveque (2007). In the work, the CG algorithm is based on the work of Leveque (2007).

Choose initial guess u_0 (possibly the zero vector)

$$r_0 = f - Au_0$$

$$p_0 = r_0$$

for $k = 1, 2, ...$

$$\omega_{k-1} = Ap_{k-1}$$

$$\alpha_{k-1} = (r_{k-1}^T r_{k-1})/(p_{k-1}^T w_{k-1})$$

$$u_k = u_{k-1} + \alpha_{k-1} p_{k-1}$$

$$r_k = r_{k-1} - \alpha_{k-1} \omega_{k-1}$$

if $\|r_k\|$ is less than some tolerance then stop

$$\beta_{k-1} = (r_k^T r_k)/(p_{k-1}^T r_{k-1})$$

$$p_k = r_k + \beta_{k-1} p_{k-1}$$

end

In this work, the tolerance is 10^{-6}.

The convergence rate of CG generally depends on the condition number of the matrix $\mathbf{A}$. Preconditioning the system can reduce the condition number of the matrix involved and speed up the convergence. $\mathbf{Ax} = \mathbf{b}$ can be solved indirectly by solving $\mathbf{M}^{-1}\mathbf{Ax} = \mathbf{M}^{-1}\mathbf{b}$. If the eigenvalues of $\mathbf{M}^{-1}\mathbf{A}$ are better clustered than those of $\mathbf{A}$, the linear equations can be iteratively solved more quickly than the original problem.

A very simple preconditioning, which is effective for some problems, is simply to use $\mathbf{M}$= $diag(\mathbf{A})$, namely Jacobi preconditioning. Generally this does not help for the Poisson problem on a rectangle computational domain, where this is just a multiple of the identity matrix, and hence does not change the condition number at all. Although Eq. 2.26 is a Poisson type equation, it is solved in a multi-phase computational domain (large gradient of density at the interface). The elements in matrix $\mathbf{A}$ are different at different phases. It was found that the Jacobi preconditioning works well in this work.

Appendix B

Water Entry of a Free-Fall Lifeboat

One of the applications of the present numerical method is to simulate the water entry of a free-fall lifeboat. Free-fall lifeboats are common life-saving appliances on seagoing vessels and offshore platforms. The numerical simulation can provide engineers the opportunity to investigate the safety of lifeboats under severe impact conditions with high accuracy, reducing the investigation time and eliminating the high costs associated with experiments.

The water entry of a free-fall lifeboat was simulated by the present method. Fig. B-1 presents the trajectories of a 3D lifeboat entering calm water. Before the boat touches the water, the main force acting on the lifeboat is its weight. The rotation of the boat during the free-fall determines the angle of attack at water entry. During water entry, the lifeboat is acted upon by the slamming forces. As shown in Fig. B-1, when the bow touches the free surface, jets are generated and the boat starts to rotate due to slamming loads and continues until the boat becomes balanced. This numerical study has shown some interesting phenomena. However, these results still need to be validated by experiments.

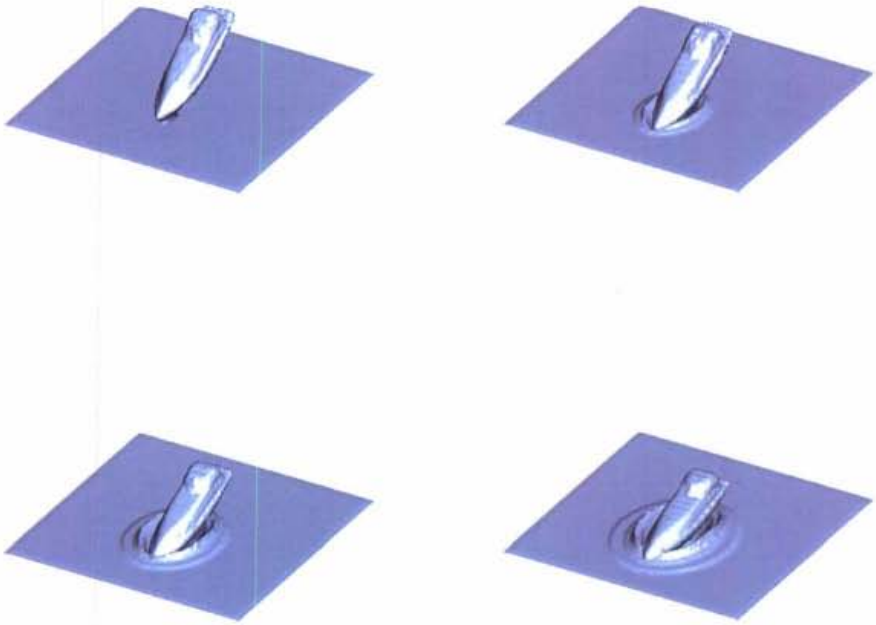

Figure B-1: A free-fall lifeboat entering calm water